

# Laser heating as approach to retard fatigue crack growth in aircraft aluminium structures

(Vom Promotionsausschuss der Technischen Universität Hamburg-Harburg als Dissertation angenommene Arbeit)

D. Schnubel



# **Laser heating as approach to retard fatigue crack growth in aircraft aluminium structures**

(Vom Promotionsausschuss der Technischen Universität Hamburg-Harburg als Dissertation angenommene Arbeit)

**D. Schnubel**

---

Die HZG Reporte werden kostenlos abgegeben.  
HZG Reports are available free of charge.

Anforderungen/Requests:

Helmholtz-Zentrum Geesthacht  
Zentrum für Material- und Küstenforschung GmbH  
Bibliothek/Library  
Max-Planck-Straße 1  
21502 Geesthacht  
Germany  
Tel.: +49 4152 87-1690  
Fax.: +49 4152 87-1717  
E-Mail: [bibliothek@hzg.de](mailto:bibliothek@hzg.de)

*Druck: HZG-Hausdruckerei*

Als Manuskript vervielfältigt.  
Für diesen Bericht behalten wir uns alle Rechte vor.

ISSN 2191-7833

Helmholtz-Zentrum Geesthacht  
Zentrum für Material- und Küstenforschung GmbH  
Max-Planck-Straße 1  
21502 Geesthacht

[www.hzg.de](http://www.hzg.de)

---

HZG REPORT 2012-5

## Laser heating as approach to retard fatigue crack growth in aircraft aluminium structures

*(Vom Promotionsausschuss der Technischen Universität Hamburg-Harburg als Dissertation angenommene Arbeit)*

Dirk Schnubel

*116 pages with 45 figures and 5 tables*

### Abstract

It is demonstrated experimentally that the laser heating process can be employed for fatigue crack growth retardation in aircraft aluminium structures. A numerical methodology for the quantitative prediction of the resulting fatigue crack growth in laser heated specimens is developed and validated on basis of the experimental results. Then the validated methodology is employed for numerically based design optimization.

## Laser-Erwärmen als Ansatz zur Verlangsamung des Ermüdungsrisswachstums in Luftfahrt-Aluminiumstrukturen

### Zusammenfassung

Es wird experimentell gezeigt, dass das Laser-Erwärmen zur Verlangsamung des Ermüdungsrisswachstums in Luftfahrt-Aluminiumstrukturen eingesetzt werden kann. Zur quantitativen Vorhersage des Ermüdungsrisswachstums in laser-erwärmten Proben wird zunächst eine numerische Methodik entwickelt, die dann auf Grundlage der experimentellen Ergebnisse schrittweise validiert wird. Anschließend wird die validierte Vorhersagemethodik zur numerischen Design-Optimierung eingesetzt.

---

# Laser heating as approach to retard fatigue crack growth in aircraft aluminium structures

Dirk Schnubel

*Institute of Materials Research, Materials Mechanics, Helmholtz-Zentrum*

*Geesthacht, 21502 Geesthacht, Germany.*

*Contact: dirk.schnubel@hzg.de*

## Abstract

One major future challenge for the aircraft industry will be the development of proper strategies for maintenance and life extension of the growing ageing aircraft fleet. In this context, residual stress based life enhancement approaches are believed to have a huge potential for cost efficient solutions.

Hence, there exists an economic rationale for the industry to extend the use of established residual stress based life enhance techniques and to explore the potential of interesting new approaches. However, it is difficult to gain official credit for the use of these techniques, since the established damage tolerance evaluation methods do not account for residual stress effects.

Following these two points, the presented work aims to demonstrate that the laser heating process is an interesting new approach for fatigue life enhancement or more specific for fatigue crack growth retardation and that it is possible to predict the resulting improvements via a FEM based numerical prediction methodology.

In a first step, it is demonstrated experimentally that laser heating is applicable to aerospace aluminium alloys. Therefore, a defocused laser is used to create a heating line on C(T)100 specimens manufactured from AA2198, a modern Al-Li-Cu alloy. The experimental program includes a characterisation of the laser heating process and the resulting changes of the mechanical behaviour. Here, the focus is laying on the measurement of the heating temperature field, the residual stress state after heating and the resulting retardation of the fatigue crack growth.

The second step is the development of a numerical prediction methodology to gain quantitative predictions of the fatigue crack growth in laser heated specimens. To reach this, a numerical process simulation for the prediction of the residual stress field after laser heating is subsequently coupled with a fracture mechanics simulation to predict the resulting fatigue crack growth. The developed methodology is then validated on basis of the experimental results.

As last step, the developed and validated approach is applied to the optimisation of the positioning of one and two heating lines on a C(T)100 specimen with regard to the total lifetime enhancement in order to demonstrate the capability of the proposed

strategy to solve design optimisation problems.

In conclusion, it is demonstrated on the laboratory scale, that laser heating has the potential to be employed for fatigue crack growth retardation in aircraft aluminium structures. The developed numerical prediction approach is capable to deliver accurate predictions of the fatigue crack growth in laser heated specimens. In contrast to the commonly used methodologies, the developed approach delivers correct predictions for cracks growing through compressive residual stress fields and furthermore it provides the possibility to employ numerically based design optimisation.

# Laser-Erwärmen als Ansatz zur Verlangsamung des Ermüdungsrisswachstums in Luftfahrt-Aluminiumstrukturen

**Dirk Schnubel**

*Institut für Werkstofforschung, Werkstoffmechanik, Helmholtz-Zentrum Geesthacht,  
21502 Geesthacht, Deutschland.*

*Kontakt: dirk.schnubel@hzg.de*

## **Zusammenfassung**

Eine der zukünftigen Herausforderungen für die Luftfahrtindustrie ist die Entwicklung von passenden Strategien für die Wartung und Lebensdauererlängerung von alternden Flugzeugstrukturen. Hier bieten eigenspannungsbasierte Verfahrensansätze ein Potential für die Entwicklung kosteneffizienter Lösungen.

Folglich gibt es einen großen ökonomischen Anreiz für die Industrie den Gebrauch von etablierten Techniken auszuweiten und Möglichkeiten neuer technischer Ansätze auszuloten. Es ist jedoch schwierig seitens der Zulassungsbehörden eine Anerkennung der Eigenschaftsverbesserungen durch die Nutzung solcher eigenspannungsbasierten Verfahren zu erhalten, da die zur Lebensdauerberechnung eingesetzten numerischen Vorhersageverfahren für die Schadenstoleranz-Analyse im allgemeinen keine Eigenspannungseffekte berücksichtigen.

Motiviert durch diese beiden Punkte wird in der vorliegenden Arbeit das Laser-Erwärmen als ein interessanter neuer Ansatz zur Lebensdauererlängerung von Flugzeugstrukturen aus Aluminium untersucht. Zudem wird gezeigt, dass die Möglichkeit besteht, die resultierende Verlangsamung des Ermüdungsrisswachstums durch eine FE basierte Methodik vorherzusagen.

Den ersten Teil der Arbeit bildet eine experimentelle Konzeptstudie in der demonstriert wird, dass es prinzipiell möglich ist, den Prozess des Laser-Erwärmens auf Luftfahrt-Aluminiumlegierungen anzuwenden. Hierzu werden mit einem defokussierten Laser Wärmelinien auf C(T)100 Proben aus der modernen Al-Li-Cu Legierung AA2198 aufgebracht. Die nachfolgenden experimentellen Untersuchungen dienen zur Charakterisierung des Prozesses und der resultierenden Änderungen im mechanischen Verhalten. Kernaspekte bilden die Messung der Prozess-Temperaturen, des Eigenspannungszustandes und des Ermüdungsrisswachstums.

Der zweite Teil der Arbeit befasst sich mit der Entwicklung einer numerischen Vorhersagemethodik für das Ermüdungsrisswachstum in lasererwärmten Proben. Die grundlegende Idee besteht in der Kopplung einer numerischen Prozesssimulation zur

Vorhersage der wärmeinduzierten Eigenspannungen mit einer nachfolgenden Bruchmechaniksimulation zur Vorhersage des resultierenden Ermüdungsrisswachstums. Die entwickelte Methodik wird dann auf Grundlage der zuvor gewonnenen experimentellen Daten validiert.

Im letzten Teil der Arbeit wird die entwickelte und validierte Vorhersagemethodik dann zur Optimierung der Positionierung von einer bzw. zwei Laser-Linien auf einer C(T)100 Probe hinsichtlich der Steigerung der Lebensdauer genutzt. Ziel ist es zu zeigen, dass durch den Einsatz der numerischen Vorhersagemethodik solche Optimierungsaufgaben gelöst werden können.

Zusammenfassend kann festgehalten werden, dass das Ermüdungsrisswachstum in Luftfahrt-Aluminiumstrukturen mittels des Laser-Erwärmens signifikant verlangsamt werden kann. In Gegensatz zu den heute gebräuchlichen Ansätzen liefert die entwickelte numerische Vorhersagemethodik gute Resultate für den betrachteten Fall von Rissen, die durch Druckeigenspannungsfelder wachsen. Das experimentell gemessene Ermüdungsrisswachstum in laser-erwärmten Proben kann akkurat vorhergesagt werden. Die entwickelte Methodik eignet sich ebenso zur numerischen Design-Optimierung.

# Contents

<b>1</b>	<b>Introduction</b>	<b>1</b>
1.1	Motivation . . . . .	1
1.2	Objectives . . . . .	2
1.3	Approach . . . . .	3
1.4	Structure of the thesis . . . . .	5
<b>2</b>	<b>Fundamentals on residual stresses and damage tolerance</b>	<b>7</b>
2.1	Residual stresses . . . . .	7
2.2	Heating induced residual stresses . . . . .	7
2.3	Numerical prediction of heating induced residual stresses . . . . .	9
2.3.1	Thermal FE analysis . . . . .	10
2.3.2	Mechanical FE analysis . . . . .	11
2.3.3	Material data . . . . .	12
2.4	The stress intensity factor concept . . . . .	13
2.5	Numerical fracture mechanics analysis using the MVCCT approach . .	14
2.6	Fatigue crack growth . . . . .	16
2.7	Prediction of FCG using empirical crack growth laws . . . . .	17
2.8	Damage tolerance . . . . .	18
2.9	Accepted processes for life enhancement via residual stresses . . . . .	21
2.9.1	Cold expansion of holes . . . . .	21
2.9.2	Shot peening . . . . .	22
2.9.3	Laser shock peening . . . . .	22
2.10	Heating as alternate process for life enhancement . . . . .	24
2.11	Comparison of heating and the established processes . . . . .	26
<b>3</b>	<b>Laser heating - Proof of concept</b>	<b>29</b>
3.1	Material: Aluminium-Lithium alloy 2198 . . . . .	29
3.2	Specimen design . . . . .	30
3.3	Laser heating process . . . . .	32
3.4	Thermocouple measurements . . . . .	33
3.5	Microscopical examinations . . . . .	36
3.6	Micro hardness measurements . . . . .	36
3.7	Tensile tests . . . . .	38

3.8	Residual stress measurements . . . . .	42
3.9	Fatigue crack growth tests . . . . .	44
3.9.1	Calibration of the Walker equation . . . . .	46
3.9.2	Comparison of base material and laser heated specimens . . . . .	46
3.10	Fractographic examination . . . . .	50
3.11	Discussion - Proof of concept . . . . .	50
<b>4</b>	<b>FCG prediction methodology</b>	<b>55</b>
4.1	Commonly used methodology . . . . .	55
4.2	Limitations of the commonly used methodology . . . . .	56
4.3	Extended prediction methodology . . . . .	56
4.4	Implementation of the extended prediction methodology . . . . .	58
<b>5</b>	<b>Validation of the FCG prediction methodology</b>	<b>61</b>
5.1	Mesh . . . . .	61
5.2	Thermal FE analysis . . . . .	62
5.3	Mechanical FE analysis . . . . .	65
5.4	Fracture mechanics analysis . . . . .	70
5.5	Empirical crack growth law . . . . .	73
5.6	Discussion - Validation of the FCG prediction methodology . . . . .	74
<b>6</b>	<b>Design optimisation</b>	<b>76</b>
6.1	Positioning of one heating line . . . . .	76
6.2	Positioning of two heating lines . . . . .	79
<b>7</b>	<b>Conclusions</b>	<b>85</b>
	<b>Bibliography</b>	<b>87</b>

# List of symbols and abbreviations

$(x_s, y_s, z_s)$	surface coordinates
$A_{HS}, B_{HS}, C_{HS}$	heat source shape parameters
$C$	material constant in Paris law and Walker equation
$E$	Young's modulus
$F_y$	component of the nodal cutting force in $y$ -direction
$G$	energy release rate
$K$	stress intensity factor
$K_c$	fracture toughness
$K_{\max}$	stress intensity due to the maximum applied load of the load cycle
$K_{\min}$	stress intensity due to the minimum applied load of the load cycle
$K_{\text{tot}}$	total stress intensity factor due to the combination of applied load and internal residual stresses
$N$	number of load cycles or flights
$N(a = 60 \text{ mm})$	number of load cycles $N$ needed for a crack with an initial length $a_0 = 25 \text{ mm}$ to reach a final length of $a = 60 \text{ mm}$
$N_i$	inspection interval
$N_{\text{th}}$	inspection threshold
$Q$	heat flux
$Q_0$	heat source amplitude
$R$	stress intensity factor ratio
$R_{\text{tot}}$	total stress intensity factor ratio
$T$	temperature

$T_0$	room temperature
$\Delta K$	stress intensity factor range
$\Delta K_{th}$	threshold stress intensity factor range
$\Delta a$	crack growth increment
$\Delta K_{tot}$	total stress intensity factor range
$\alpha$	coefficient of thermal expansion
$\epsilon_{eq}^p$	cumulative plastic strain
$\epsilon_r$	thermal emissivity
$dT$	temperature increment
$d\epsilon$	total strain increment
$d\epsilon^e$	elastic strain increment
$d\epsilon^p$	plastic strain increment
$d\epsilon^{th}$	thermal strain increment
$d\sigma$	stress increment
$da/dN$	fatigue crack growth rate
$\lambda$	thermal conductivity
<b>div</b>	vector operator divergence
<b>grad</b>	vector operator gradient
$\nu$	Poisson's ratio
$\rho$	specific weight
$\sigma$	stress
$\sigma_{eq}$	Mises stress
$\sigma_l$	limit load of the structure
$\sigma_m$	middle bar stress
$\sigma_{rs}$	residual strength

$\sigma_{\text{r}}$	Stefan Boltzmann constant
$\sigma_{\text{s}}$	side bar stress
$\sigma_{\text{uts}}$	ultimate tensile strength
$\sigma_{\text{ys}}$	yield stress
$a$	crack length
$a_0$	initial crack length
$a_{\text{c}}$	critical crack length for a catastrophic failure under static loading
$a_{\text{d}}$	detectable crack length
$b$	specimen thickness
$c$	specific heat
$f(a)$	geometry form function
$h_{\text{c}}$	coefficient of convective thermal exchange
$m$	material constant in the Walker equation
$n$	material constant in Paris law and Walker equation
$s_{ij}$	stress deviator tensor
$t$	time
$u_{\text{y}}$	component of the nodal displacement in $y$ -direction
$v_{\text{y}}$	travelling speed of the heat source
$x, y, z$	space coordinates
$x_0, y_0, z_0$	start position of the heat source centre
$x_{\text{h,opt}}$	optimum position of the heating line for designs with only one heating line
$x_{\text{h1,opt}}$	optimum position of the first heating line for designs with two heating lines
$x_{\text{h1}}$	position of the first heating line for designs with two heating lines

$x_{h2,opt}$	optimum position of the second heating line for designs with two heating lines
$x_{h2}$	position of the second heating line for designs with two heating lines
$x_h$	position of the heating line for designs with only one heating line
AA	aluminium alloy
Ag	silver
BM	name prefix for base material specimens/results or area with base material properties
C(T)	compact tension specimen
CS	specimen name suffix macro cross section
Cu	copper
DESY	Deutsches Elektronen-Synchrotron
EBSD	electron backscatter diffraction technique
EXP	name suffix for experimental results
FCG	fatigue crack growth, also used as specimen name suffix
Fe	iron
FE analysis	finite element analysis
FEM	finite element method, also name suffix for numerical prediction results
HARWI-II	hard X-ray wiggler beamline W2 of HZG at DESY
HAZ	heat affected zone
HV	Vickers hardness
HZ	heating zone
HZG	Helmholtz-Zentrum Geesthacht
L-T	testing orientation with specimen in L-T plane and crack in T direction
X	

LH	name prefix for laser heated specimens/results
Li	lithium
Mar555	image plate detector for diffraction experiments at HARWI-II
MCCI	modified crack closure integral
Mg	magnesium
Mn	manganese
MVCCT	modified virtual crack closure technique
Nd:YAG	neodymium-doped yttrium aluminium garnet
OM	light optical microscope
RS	specimen name suffix residual stress measurement
SEM	scanning electron microscope
Si	silicon
T-L	testing orientation with specimen in L-T plane and crack in L direction
T3	aluminium alloy temper designation: solution heat treated, cold worked
T8	aluminium alloy temper designation: solution heat treated, cold worked, artificially aged
TC	specimen name suffix thermocouple measurement
TT	specimen name suffix tensile test
VCCT	virtual crack closure technique
WFM	weight function method
Zn	zinc
Zr	zirconium



# 1 Introduction

## 1.1 Motivation

Up to now residual stress effects are not addressed explicitly in the design and damage tolerance evaluation of aircraft structures or components [1]. This includes the favourable residual stresses willingly introduced by life enhancement methods, as well as, the unwillingly introduced ones from production processes like for example forging or welding.

Interestingly, the production induced residual stresses are the reason why the whole topic of residual stresses and damage tolerance gained increasing attention during the last years, especially in the scientific community. There was a rising awareness, that not including residual stress effects in the prediction methods used for damage tolerance evaluation involves the risk of non-conservative designs [2]. This was leading to fundamental research with a special focus on the prediction of the fatigue crack growth including the residual stress effects for integral welded metallic aircraft structures [3–7]. That activities also triggered further research aiming to predict [8–13] and experimentally characterise [14–16] the residual stress state after welding in such structures.

One major future challenge for the aircraft industry will be the development of proper strategies for maintenance and life extension of the growing ageing aircraft fleet. In this context, residual stress based life enhancement approaches provide cost efficient solutions [1, 17, 18].

Even though these approaches offer the potential of large improvements by inducing compressive residual stresses at critical locations [1, 18], it is barely possible to exactly characterise the amount of residual stresses induced for each part under industrial production conditions and there are concerns that the residual stress state might change during the long service life of approximately 30 years for aircraft [1]. Additionally, as explained earlier, the residual stress effects are not explicitly addressed in the damage tolerance evaluation. Hence, the authorities claim that damage tolerance requirements generally have to be reached without considering beneficial effects of residual stress based life enhancement processes [19, 20].

However, experience has shown that the use of such processes, like for example the cold expansion of rivet holes, helps to significantly decrease the maintenance costs [1, 17]. This was over the last decades a strong economically driven motivation for the manufacturers and operators to continue using them and to try to convince

the authorities to grant them official credit for their use.

Currently, the authorities make exceptions from their general policy in very narrow confines if the manufacturer or operator can proof the effectiveness of the life enhancement experimentally and via predictions for the specific envisaged application case [19, 20]. Even though this procedure is both time consuming and expensive for each individual case, it is an important step towards a general acceptance for such enhancement approaches.

Due to the existing limitations of the established enhancement processes, for example with regard to special geometries or the maximum amount of induced residual stresses, it is also attractive for the industry to explore the possible benefits of different new approaches. A prominent example for such new process is the laser shock peening.

In summary it can be said that there is a large economic motivation of the industry to extend the use of established residual stress based life enhance techniques and to explore the potential of interesting new approaches. However, at the same time it is difficult to gain official credit for their use, since the established damage tolerance evaluation methods do not account for residual stress effects. In this context, the earlier mentioned safety driven scientific research on quantitative prediction methodologies that address also the residual stress effects opens a perspective for an improvement of that situation.

Following this two points, the presented work aims to demonstrate that the laser heating process is an interesting new approach for fatigue life enhancement or more specific for fatigue crack growth retardation and that it is possible to predict the resulting improvements by the development of a quantitative numerical prediction methodology.

## 1.2 Objectives

While the formation of thermally induced residual stresses is seen normally as detrimental side effect from production processes like welding or casting, some researchers also used the well directed introduction of thermal residual stresses as tool to retard the fatigue crack growth in thin walled structures during the last decades [21–30].

As already stated, in the presented work this principle shall be investigated under the aspect of a possible application to thin walled aerospace structures and hence three main objectives have been defined:

- The experimental proof of concept that it is possible to retard the fatigue crack growth via laser heating induced residual stresses in aircraft aluminium structures shall be given.
- A numerical prediction methodology for the resulting fatigue crack growth of

specimens containing laser heating residual stresses shall be developed and validated.

- It shall be demonstrated that it is possible to solve design optimisation problems by the use of the developed and validated prediction methodology.

Besides of the examination of laser heating as an alternative process for life enhancement with a clear economic potential, the development of a reliable quantitative numerical prediction methodology addresses one essential requirement for its application in structures designed based on the damage tolerance philosophy. This will help to increase the acceptance of such an approach, as well as give an added value by contributing to the general improvement of the existing prediction methodologies at the same time.

The presented work shall also establish the foundations for a future vision, the numerically based design optimisation of large light-weight structures. Therefore, the applicability of the developed prediction methodology for solving design optimisation problems shall be demonstrated on the laboratory scale.

## 1.3 Approach

Figure 1.1 shows a schematic view of the proposed scientific approach to reach the defined objectives.

In a first step, an experimentally based proof of concept for the specific case of the modern aluminium aerospace alloy AA2198 using C(T)100 specimens containing a single line of laser heating at a fixed position will be given. This includes the characterisation of the laser heating temperature field, the residual stress state after heating and the resulting effect on the fatigue crack growth.

The second step is the development of a numerical methodology for quantitative predictions of the fatigue crack growth in laser heated specimens. To reach this, a numerical process simulation for the prediction of the residual stress field after laser heating will be subsequently coupled with a fracture mechanics simulation to predict the resulting fatigue crack growth.

In the next step, the developed prediction methodology will be validated on basis of the generated experimental data.

As the last step, the developed and validated approach will be applied to the optimisation of the positioning of one and two heating lines on a C(T)100 specimen, in order to demonstrate the capability of the proposed strategy to solve design optimisation problems.

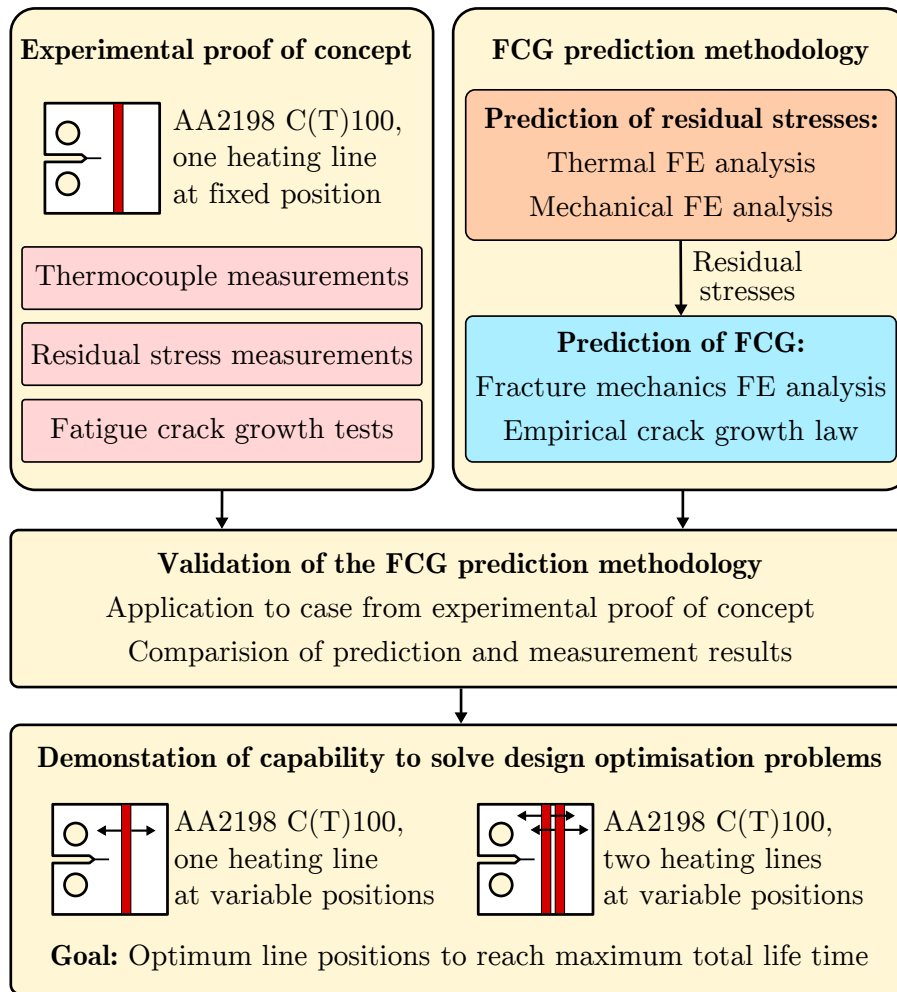


Figure 1.1: Schematic view of the scientific approach of the thesis.

## 1.4 Structure of the thesis

The thesis was structured according to the schematic view of the scientific approach (Fig. 1.1) extended by an introducing section on the fundamentals of the methods and concepts used, as well as a final section with concluding remarks.

Chapter 2 gives a brief introduction on the fundamentals of utilising residual stresses for the improvement of the fatigue behaviour. The general introduction of residual stresses, fatigue crack growth and damage tolerance is followed by an overview on prominent and generally accepted residual stress based approaches for life enhancement and is closed by an introduction on the use of heating as approach for life enhancement.

In chapter 3 it is demonstrated experimentally that laser heating can be used to substantially retard the fatigue crack growth for the specific case of an aluminium C(T)100 specimen containing one laser heating line at a fixed position. The detailed description of the process is followed by an experimental study including the characterisation of the laser heating temperature field, the residual stress state after heating and the resulting effect on the fatigue crack growth.

The goal of chapter 4 is the development of the needed quantitative prediction methodology for the fatigue crack growth in laser heated specimens. After the discussion of the commonly used approaches, currently existing limitations are identified. Hence, an extended prediction methodology is proposed to overcome these limitations and its specific implementation to deal with laser heated specimens is shown.

In chapter 5 the extended prediction methodology developed in chapter 4 is applied to the experimentally examined case of chapter 3. This way it is possible to gain a validation for each prediction step on basis of the experimental data.

In chapter 6 the validated prediction methodology is used to solve two design optimisation problems, the positioning of either one or two heating lines on a C(T)100 specimen in order to gain a maximum life enhancement effect. For both cases the prediction results are validated for specific positions to proof the validity of the chosen strategy.

In Chapter 7 the conclusions resulting from the presented study are given.



## 2 Fundamentals on residual stresses and damage tolerance

This chapter gives a brief introduction on the fundamentals of using residual stresses for the improvement of the damage tolerance performance. The general remarks on residual stresses, fracture mechanics, fatigue and damage tolerance and the related prediction approaches shall establish the terminology used in the following and give a basic idea of the underlying principles and concepts.

After the general remarks an overview on the established residual stress based life enhancement approaches for aerospace applications is given. The chapter is closed by a review of work published on heating based approaches for life enhancement and a comparison of heating to the discussed established approaches.

### 2.1 Residual stresses

Residual stresses are the internal stresses that are still present even if all external loads are removed [31]. This means that they are in equilibrium with themselves [31, 32].

In general, macroscopic residual stresses are to be distinguished from microscopic residual stresses. Microscopic residual stresses have their origin in microstructural inhomogeneities like for example the grain or dislocation structure. Macroscopic residual stresses vary on a scale where the material behaviour can be described as a continuum. They are, for example, the result of localised plastic deformations.

Such macroscopic residual stresses are of particular importance for engineering applications, since they can have a substantial impact on the performance and failure behaviour of components and structures [31–33]. In the following, the use of the term residual stresses always refers to these macroscopic residual stresses.

### 2.2 Heating induced residual stresses

Since heating is the underlying process for the presented work in this thesis, a small recap on the underlying physical phenomena leading to the formation of the heating induced residual stresses shall be given.

To understand the formation of the heating residual stresses one can perform a simple thought experiment adopted from [31] and sketched in Fig. 2.1a.

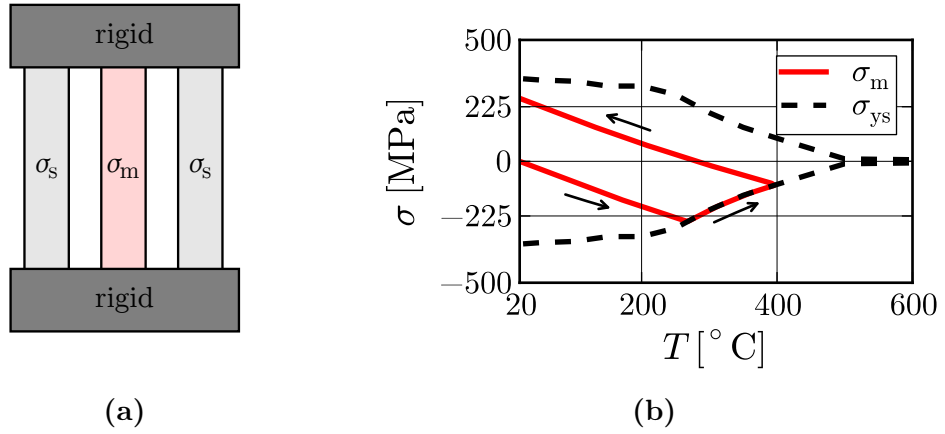


Figure 2.1: (a) Set-up of the thought experiment and (b) evolution of the residual stresses in the middle bar due to the applied thermal cycle [31].

First, three stress free aluminium bars of equal length and cross section at room temperature  $T_0$  are rigidly connected by two blocks at their ends. The middle bar then is heated up. Since the two side bars are rigidly connected, they respond to the thermal expansion of the middle bar and the stress in each side bar  $\sigma_s$  has always half the amplitude as the stress in the middle bar  $\sigma_m$  but with opposite sign. This can be expressed as [31]:

$$\sigma_s = -\frac{1}{2} \sigma_m \quad (2.1)$$

where are  $\sigma_s$  the stress in each side bar and  $\sigma_m$  the stress in the middle bar.

Additionally, due to the rigid connection, the length of all bars must be the same at any time what leads to the expression [31]:

$$\frac{\sigma_s}{E(T_0)} = \frac{\sigma_m}{E(T)} + \alpha(T - T_0) \quad (2.2)$$

where are  $T$  the temperature,  $T_0$  the room temperature,  $E$  the Young's modulus and  $\alpha$  the coefficient of thermal expansion.

Combining Eq. 2.1 with Eq. 2.2 and solving the equation with respect to the stress in the middle bar  $\sigma_m$  leads to [31]:

$$\sigma_m = -\alpha (T - T_0) \frac{2 E(T_0)}{1 + [2 E(T_0)/E(T)]} \quad (2.3)$$

Of course the maximum possible stress is limited by the temperature dependent yield stress  $\sigma_{ys}$ . Hence, when the stress in one of the bars tries to exceed  $\sigma_{ys}$  the result is a plastic deformation of that bar.

Figure 2.1b shows the corresponding evolution of the stress in the middle bar  $\sigma_m$  while heating it up to a peak temperature of  $T = 400$  °C and subsequent cooling it down to room temperature again. The used material properties are the same as used for the process simulations presented in chapter 5.

During the heating, the middle bar tries to expand, but the free expansion is constrained by the side bars. Hence  $\sigma_m$  becomes increasingly negative with increasing temperature until it reaches the yield stress  $\sigma_{ys}$ . From here onwards,  $\sigma_m$  is limited to the yield stress curve and follows it under plastic yielding until reaching the peak temperature  $T = 400$  °C. In the following, the middle bar cools down to room temperature again. Hence,  $\sigma_m$  decreases, changes sign from negative to positive stresses at a temperature above room temperature and reaches a final positive value at room temperature. The observed non-linear behaviour during the elastic loading and unloading is due to the non-linearity of  $E(T)$ .

From Eq. 2.1 the final stress in each of the two side bars  $\sigma_s$  is compressive with half the amplitude of  $\sigma_m$ . This final distribution with a high induced tensile stress in the heating area and balancing compressive stresses in the surrounding material is typical for heating induced residual stresses.

## 2.3 Numerical prediction of heating induced residual stresses

To predict heating-induced residual stresses, a subsequently coupled thermal and mechanical FE analysis must be conducted. As first step, a thermal simulation is conducted and the results are used in the following mechanical analysis to include the thermal strains attributable to thermal expansions [34]. This approach of subsequently coupled thermal and mechanical FE analysis is commonly used for structural welding simulations [12, 32, 35]. A thorough overview of the topic is presented, for example, by Radaj in [32]. For further orientation, [35, 36] also provide some general discussion of the impact of specific simplifications and modelling strategies on the achievable quality of the results.

A large amount of research work has been conducted in the past decades on the simulation of steel welding, but only a few studies have been published on its application to aluminium aerospace alloys. For example, in [8–10] friction stir welding of aerospace aluminium alloys was investigated. In [11, 12, 37–40], the resulting distortions and residual stresses after laser beam welding of aluminium T-joints were predicted. In [13, 41] the fusion welding of AA2024 butt joints was studied, and the impact of the testing conditions used to gain the needed temperature-dependent

material properties on the prediction results was discussed.

The next two sections give the details of the model that will be employed later for the prediction of the laser heating residual stresses. The presented model set-up can be seen as prototype for such simulations. For other application cases, it might be suitable to change minor details, like the used hardening law or the heat source definition, but the general approach remains the same.

### 2.3.1 Thermal FE analysis

For the thermal analysis, a pure heat conduction model including heat sinks and sources is used. The governing differential equation is given as [34]:

$$\rho(T) c(T) \frac{\partial T}{\partial t} - \mathbf{div} (\lambda(T) \mathbf{grad} T) - Q = 0 \quad (2.4)$$

where are  $T$  the temperature,  $c$  the temperature dependent specific heat,  $\rho$  the temperature dependent density,  $\lambda$  the temperature dependent thermal conductivity and  $Q$  the temperature and/or time dependent heat flux density (heat sources, boundary conditions).

The heat flux density of the heat source  $Q_{\text{in}}$  can be modelled for example as a Goldak ellipsoid volume heat source using the space coordinates  $x, y, z$  and the time  $t$  [32, 34]:

$$Q_{\text{in}}(x, y, z, t) = Q_0 \exp \left( -\frac{(y - y_0 - v_y t)^2}{A_{\text{HS}}^2} - \frac{(x - x_0)^2}{B_{\text{HS}}^2} - \frac{(z - z_0)^2}{C_{\text{HS}}^2} \right) \quad (2.5)$$

where are  $Q_0$  the heat source amplitude,  $(x_0, y_0, z_0)$  the start position of the heat source centre,  $(A, B, C)$  the heat source shape parameters and  $v_y$  the travelling speed of the heat source in  $y$ -direction. Following this definition, the heat source travels in positive  $y$ -direction with the speed  $v_y$ .

The heat exchange between model surface and environment is defined as combination of convective and radiative heat loss with the surface heat flux density [34]:

$$Q_{\text{out}}(x_s, y_s, z_s, T) = -h_c(T - T_0) - \sigma_r \epsilon_r [T^4 - T_0^4] \quad (2.6)$$

where are  $(x_s, y_s, z_s)$  the surface coordinates,  $T$  the absolute surface temperature,  $T_0$  the absolute ambient temperature,  $h_c$  the coefficient of convective thermal exchange,  $\sigma_r$  the Stefan Boltzmann constant and  $\epsilon_r$  the thermal emissivity.

This simulation approach does not account for the real physical interaction between heat source and material. Hence, the thermal boundary conditions need to be calibrated on an experimental basis with the goal to identify a good representation of

the real process conditions. Best practise for welding simulations is to characterise the global transient temperature field by thermocouple measurements for specific positions and the localised heat input by the shape of molten zone measured in optical macro cross-sections. Then, the thermal boundary conditions are varied iteratively in order to minimise the prediction error compared to the measurement data.

In general, the reached peak temperatures in the simulations are dominated by the heat source definition and the fade of the temperature after the heat source passed is directly related to the heat exchange with the environment.

### 2.3.2 Mechanical FE analysis

In the mechanical analysis elasto-plastic material behaviour with isotropic hardening and an additive decomposition of the total strain increment is assumed [34, 42]:

$$d\epsilon = d\epsilon^e + d\epsilon^p + d\epsilon^{th} \quad (2.7)$$

where are  $d\epsilon$  the total strain increment,  $d\epsilon^e$  the elastic strain increment,  $d\epsilon^p$  the plastic strain increment and  $d\epsilon^{th}$  the thermal strain increment.

During the calculations, the thermal strains are updated for each time step on the basis of the results of the thermal analysis and the thermal strain increment  $d\epsilon^{th}$  is expressed as [34, 42]:

$$d\epsilon_{ij}^{th} = \alpha_{ij} dT \delta_{ij} \quad (2.8)$$

where are  $\alpha$  the thermal expansion coefficient,  $dT$  the temperature increment and  $\delta_{ij}$  the Kronecker delta.

The elasticity law is written as [42]:

$$d\epsilon_{ij}^e = \frac{1 + \nu}{E(T)} d\sigma_{ij} - \frac{\nu}{E(T)} d\sigma_{kk} \delta_{ij} \quad (2.9)$$

where are  $E$  the temperature dependent Young's modulus,  $\nu$  the Poisson's ratio,  $d\epsilon^e$  the elastic strain increment and  $d\sigma$  the stress increment.

The bounds of the elastic regime are defined by the yield function  $F$ , which is dependent on the stress tensor  $\sigma$  and the yield stress  $\sigma_{ys}$  [34, 42]:

$$F(\sigma, \sigma_{ys}(T, \epsilon_{eq}^p)) \leq 0 \quad (2.10)$$

$$\epsilon_{eq}^p = \int \sqrt{\frac{2}{3}} d\epsilon^p : d\epsilon^p \quad (2.11)$$

where are  $\epsilon_{eq}^p$  the cumulative plastic strain,  $\sigma$  the stress tensor and  $\sigma_{ys}$  the yield stress.

Since isotropic hardening is assumed, the yield stress  $\sigma_{ys}$  becomes dependent on both the temperature  $T$  and the cumulative plastic strain  $\epsilon_{eq}^p$ . Using the von Mises criterion, the yield surface in the stress space is more specifically defined as [42]:

$$F(\sigma, \sigma_{ys}(T, \epsilon_{eq}^p)) = \sigma_{eq} - \sigma_{ys}(T, \epsilon_{eq}^p) \quad (2.12)$$

$$\sigma_{eq} = \sqrt{\frac{3}{2} s : s} \quad (2.13)$$

$$s_{ij} = \sigma_{ij} - \frac{\sigma_{kk}}{3} \delta_{ij} \quad (2.14)$$

where are  $\epsilon_{eq}^p$  the cumulative plastic strain,  $\sigma$  the stress tensor,  $\sigma_{ys}$  the yield stress,  $\sigma_{eq}$  the Mises stress and  $s_{ij}$  the stress deviator tensor.

Accordingly, the flow rule  $F = 0$  can be equally expressed as  $\sigma_{eq} = \sigma_{ys}$ . If the flow rule and the loading condition are satisfied, i.e.  $\sigma_{eq}$  aims to exceed the yield surface, plastic flow occurs. The plastic strain increment  $d\epsilon^p$  is then defined as [42]:

$$d\epsilon_{ij}^p = d\epsilon_{eq}^p \frac{\partial F}{\partial \sigma_{ij}} = d\epsilon_{eq}^p \frac{3}{2} \frac{s_{ij}}{\sigma_{ys}} \quad (2.15)$$

where  $d\epsilon_{eq}^p$  represents the increment of the cumulative plastic strain, which can be determined from the condition that the yield criterion must be satisfied at all times during plastic straining [42]:

$$F(\sigma_{ij} + d\sigma_{ij}, \epsilon_{eq}^p + d\epsilon_{eq}^p) = F(\sigma_{ij}, \epsilon_{eq}^p) + \frac{\partial F}{\partial \sigma_{ij}} d\sigma_{ij} + \frac{\partial F}{\partial \epsilon_{eq}^p} d\epsilon_{eq}^p = 0 \quad (2.16)$$

$$\Rightarrow d\epsilon_{eq}^p = \left( \frac{d\sigma_{ys}}{d\epsilon_{eq}^p} \right)^{-1} \frac{3}{2} \frac{s_{ij}}{\sigma_{ys}} d\sigma_{ij} \quad (2.17)$$

where  $d\sigma_{ys}/d\epsilon_{eq}^p$  represents the slope of the plastic stress-strain curve that governs the amount of the isotropic hardening.

### 2.3.3 Material data

A sensitive point for both thermal and mechanical analysis is the need of material data covering the whole temperature range from room temperature up to the melting temperature. Especially for new materials, such as high strength aircraft aluminium alloys, such data is not available in the literature. Moreover, the measurement of such data is not trivial, since especially for precipitation hardened aluminium alloys the yield stress shows a strong dependency on the exposure time to the testing temperature.

For example, during the laser heating process the material is exposed only for a

couple of seconds to temperatures above 250°C. Hence, it can be expected that using material data from tests with long hold times at temperature before testing, as they can be found for example in [43] for many aluminium alloys, is not leading to reasonable prediction results [13]. To gain accurate predictions, material data being representative for the real process conditions has to be used.

Some researchers also developed approaches to account for the changes of the precipitation state during welding or heating in detail on basis of the transient temperatures [44–46]. While these models were used successfully to predict the hardness distribution found in aluminium welds [45, 46], the needed model calibration for a specific material is connected with a high experimental effort. However, the effect of including such models in the numerical welding simulation was found to lead only to very slight changes of the predicted residual stresses for single pass aircraft aluminium welds [12, 41] under the condition that the material properties used in the simulation are representative for the real process conditions. However, not including such models has the consequence that the process simulation is not capable to deliver reasonable prediction results for multiple passes of heating or welding at the same position.

In the presented study no model accounting for the changes of the precipitation state was used in the process simulations. Hence, for the solving of the design optimisation problem including two heating lines in section 6.2 the parameter combinations leading to a multiple heating at the same position were explicitly excluded.

## 2.4 The stress intensity factor concept

One objective of fracture mechanics is to derive predictions of the fracture or fatigue failure of real structures or components that can contain cracks on the basis of experiments carried out on coupon specimens. The linear elastic stress intensity factor  $K$  is a measure for the local loading conditions at the crack tip. Equation 2.18 gives a general definition of the stress intensity factor  $K$  [47]:

$$K = \sigma \sqrt{\pi a} f(a) \quad (2.18)$$

where are  $\sigma$  the applied stress,  $a$  the crack length and  $f(a)$  the form function.

Following this definition,  $K$  is directly linked to the crack length  $a$  and the applied stress  $\sigma$ , while the influence of the specimen or component geometry is added as separate form function  $f(a)$ , that itself depends on the crack length again. By using  $K$  to relate physical phenomena like fatigue crack growth or static failure directly to the loading conditions at the crack tip, it becomes possible to compare cases with the completely different crack lengths, applied loads and geometries.

## 2.5 Numerical fracture mechanics analysis using the MVCCT approach

There are many approaches to calculate the stress intensity factor  $K$  using either the elastic stress field or the energy balance approach [47, 48].

In the following, an introduction to an energy balance based approach, the modified virtual crack closure technique (MVCCT) or sometimes also referred to as modified crack closure integral (MCCI), is given. This method has shown to be very suitable for the calculation of stress intensity factors in residual stress fields [6, 49] and will therefore be used for the calculations in the later sections.

Based on the Griffith energy balance approach it is possible to link  $K$  to the energy release rate  $G$ .  $G$  describes the change of the elastically stored energy due to an incremental crack extension  $da$  [47]:

$$K = \sqrt{G E} \quad (\text{plane stress}) \quad (2.19)$$

where are  $K$  the stress intensity factor,  $G$  the energy release rate and  $E$  the Young's modulus.

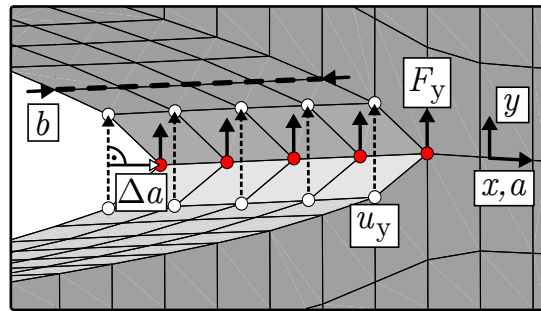
To get an estimate of  $G$ , a linear elastic FE model containing an artificial crack of the length  $a$  is created and solved including all relevant boundary conditions like applied loads or initial stresses. Then, the MVCCT approach as sketched in Fig. 2.2a is applied [48]:

$$G = \frac{1}{2 \cdot b \cdot \Delta a} \sum F_y \cdot u_y \quad (2.20)$$

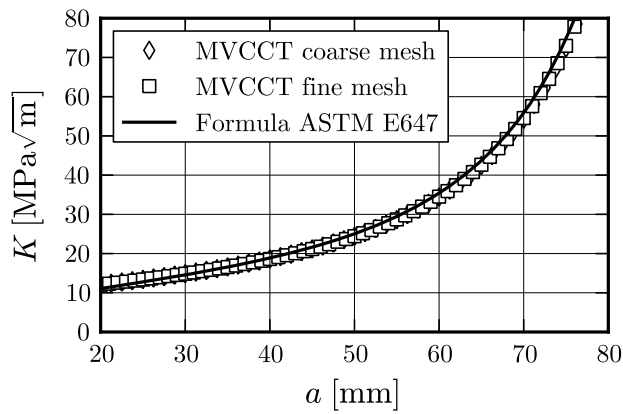
where are  $b$  the specimen thickness,  $F_y$  the nodal cutting forces of the crack tip nodes and  $u_y$  the nodal displacements of the nodes located on the crack faces at a distance  $\Delta a$  behind the crack tip.

In this approach the nodal cutting forces at the crack tip and the displacements of the nodes on the crack faces directly behind are used to estimate the energy change due to the crack extension of one increment  $\Delta a$ . To get the energy release rate, this energy change needs to be normalised to the product of the crack increment  $\Delta a$  and the specimen thickness  $b$ . The stress intensity factor  $K$  can then be directly calculated using  $G$  in Eq. 2.19.

As the name suggests, the MVCCT approach is based on the Virtual Crack Closure Technique (VCCT) [50]. In this basic version for each crack length two simulations are carried out. In the first simulation the cutting forces of the crack tip nodes are extracted. For the second simulation the crack is extended one crack growth increment  $\Delta a$  and then, the displacement of the former crack tip nodes is extracted. The underlying assumption of the MVCCT approach is that the displacement of the



(a)



(b)

Figure 2.2: (a) Schematic view of the extraction of  $K$  via the MVCCT approach and (b) calculated  $K$  from the handbook solution given in ASTM E647 in comparison to two numerical estimations using the MVCCT with different element sizes for an aluminium C(T)100 specimen. The results of the two numerical estimations of  $K$  overlap each other.

nodes directly behind the crack tip is approximately equal to the displacement of former crack tip nodes after crack extension of one small increment. Or in other words that the structural response stays self similar with a small crack extension of  $\Delta a$ .

Figure 2.2b shows the numerically calculated stress intensity factors using the MVCCT approach and the handbook solution given in ASTM E647 [51] for an aluminium C(T)100 specimen having a thickness of 5 mm for a constant applied load of  $F = 4.10$  kN. One of the big advantages of the energy balance based approaches is its mesh insensitivity, since no exact knowledge of the singular stress field at the crack tip is needed. In the given example the results for a coarse mesh consisting of only 38 000 linear solid elements with a constant edge length of 1.25 mm and a fine mesh consisting of 200 000 linear solid elements are shown. For the fine mesh the element edge length was refined to 0.25 mm along the crack path. As seen, the refined meshing had no visible effect on the extracted  $K$ .

## 2.6 Fatigue crack growth

The term fatigue crack growth (FCG) describes the extension of an existing crack under applied cyclic loading conditions. One basic attribute of FCG is that a crack extension takes place even for such low applied loads that a single loading would not generate a measurable crack extension. However, due to the high number of loading cycles, even smallest crack extension increments are summed up to a measurable quantity [52].

Following the stress intensity approach, the conditions at the crack tip during cyclic loading can be expressed as [47, 52]:

$$\Delta K = K_{\max} - K_{\min} \quad (2.21)$$

$$R = K_{\min}/K_{\max} \quad (2.22)$$

where are  $\Delta K$  the stress intensity factor range,  $R$  the stress intensity factor ratio,  $K_{\min}$  the minimum applied load of the load cycle and  $K_{\max}$  the maximum applied load of the load cycle.

Based on experimental examinations it is possible now to correlate the fatigue crack growth rate  $da/dN$  to these two quantities [47, 52]:

$$da/dN = f(\Delta K, R) \quad (2.23)$$

where is  $da/dN$  the fatigue crack growth rate.

The experimentally found characteristics are shown in Fig. 2.3. As seen, it is possible to divide the crack growth into three regions. While the lower limit in region

I is given by the threshold stress intensity factor range  $\Delta K_{th}$ , where no crack growth can be observed, the upper limit in region III is given by the fracture toughness  $K_c$ . In between an area can be found with a linear dependency between  $\log da/dN$  and  $\log \Delta K$ , region II. All discussions in the later sections will be limited to the behaviour in that region, the so called Paris region.

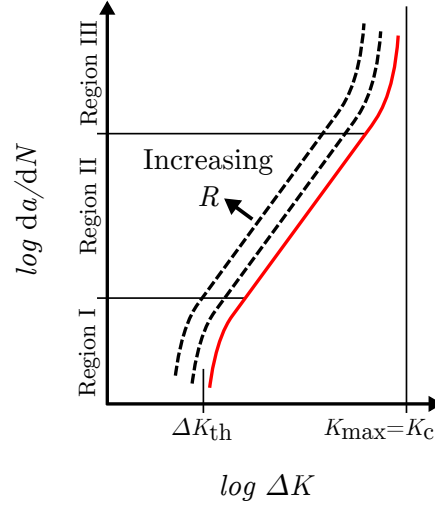


Figure 2.3: Characteristics of the fatigue crack growth rate curve  $da/dN(\Delta K)$  [47, 52].

## 2.7 Prediction of FCG using empirical crack growth laws

Empirical crack growth laws are mathematical models that try to express the experimentally found dependencies shown in Fig. 2.3. The most prominent and most simple one is the Paris law [52] giving the name to region II and describing the seen linear dependence for constant  $R$ :

$$da/dN = C \Delta K^n \quad (2.24)$$

where are  $da/dN$  the fatigue crack growth rate,  $\Delta K$  the stress intensity factor range and  $C$ ,  $n$  material constants.

As denoted in Fig. 2.3, an increase of  $R$  leads to a shift of the whole curve towards higher  $da/dN$  and lower  $\Delta K$  [47, 52]. The most simple empirical crack growth law, which is sensitive to  $\Delta K$  and  $R$  is the Walker equation [53]:

$$da/dN = C \left[ \Delta K [1 - R]^{m-1} \right]^n \quad (2.25)$$

where are  $da/dN$  the fatigue crack growth rate,  $\Delta K$  the stress intensity factor range,  $R$  the stress intensity factor ratio and  $C, n, m$  material constants.

There exists a broad variety of different and more complex crack growth laws like for example the NASGROW equation that also describe the behaviour in region I and region III [47, 52]. However, the larger number of material constants is drastically increasing the experimental effort to calibrate these models for the use with new materials. Thus, the Walker equation as given in Eq. 2.25 will be used in the later sections.

The number of loading cycles  $N$  until reaching a specific crack length  $a$  can be obtained by the integration of the inverse of the predicted crack growth rate. For the Walker equation given in Eq. 2.25 this integration leads to the expression:

$$\int_0^N dN = \int_{a_0}^a \left( C \left[ \Delta K [1 - R]^{m-1} \right]^n \right)^{-1} da \quad (2.26)$$

The right-hand side of Eq. 2.26 can be evaluated by numerical integration using the corresponding calculated  $\Delta K$  and  $R$  as supporting points to obtain the function  $N(a)$ . Under the assumption that only crack growth rates larger than zero exist, the inverse function is unique and yields the desired crack length as a function of the number of loading cycles  $a(N) = N^{-1}(a)$ .

## 2.8 Damage tolerance

The Damage tolerance philosophy for the design of aircraft structures was developed in the 1970s. This concept was born due to the rising awareness that the commonly used safe life design philosophy was not protecting against designs that are intolerant to defects emerging from manufacturing or service use [20]. Therefore the main objective of damage tolerant design is to enable the structure to withstand existing defects of a detectable size. This way it becomes possible to find the defects in periodical inspections before they grow to a size that leads to a catastrophic failure [20, 54, 55].

For damage tolerant design an evaluation of the structure needs to be performed under typical load and environmental conditions to show that catastrophic failure will be avoided throughout the whole operational life. This can only be reached if an adequate inspection and maintenance program is established for all structural elements whose failure, if remained undetected, would lead to the loss of the aircraft [54]. The basic principle of such a damage tolerance evaluation is shown in Fig. 2.4.

The first step of the damage tolerance evaluation is a residual strength analysis.

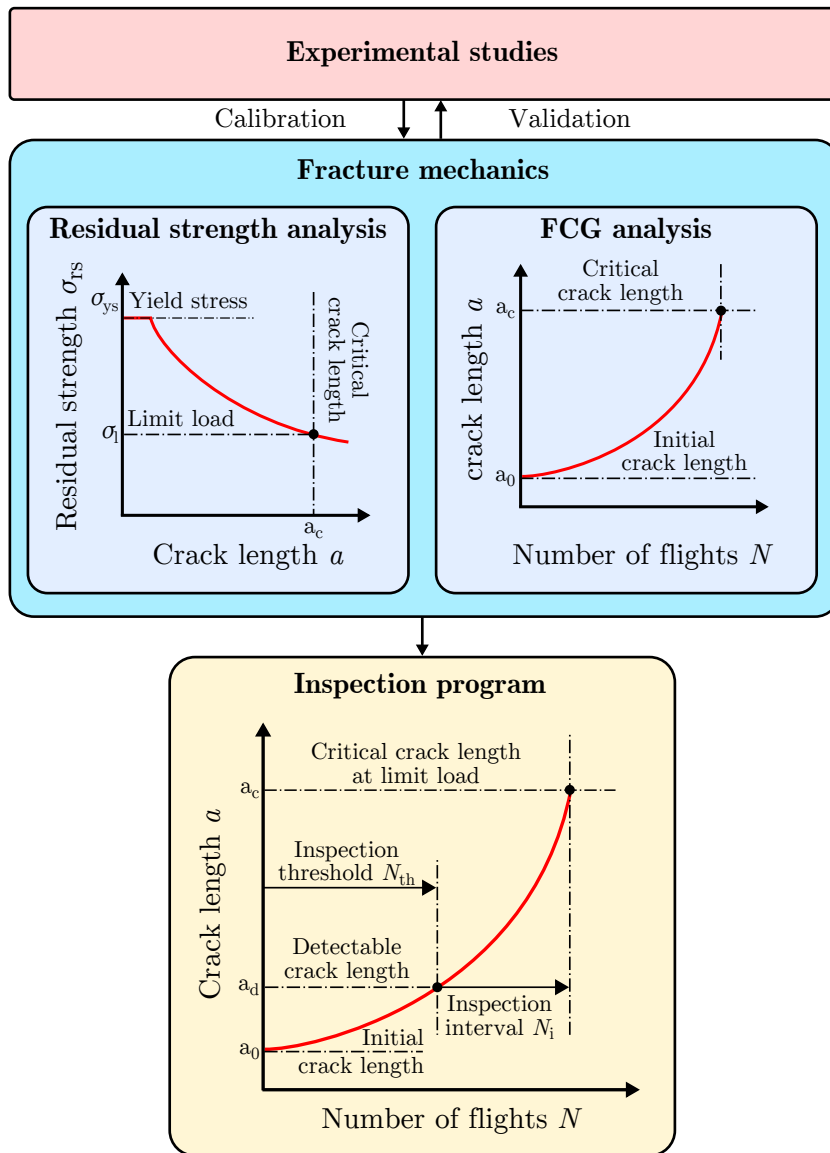


Figure 2.4: Damage tolerance evaluation of aircraft structures [20, 54, 55].

The residual strength  $\sigma_{rs}$  is the maximum static load that a structure containing a crack of the length  $a$  can bear without catastrophic failure. While the maximum value of  $\sigma_{rs}$  is given by the yield strength  $\sigma_{ys}$  when the structure does not contain a crack,  $\sigma_{rs}$  drops fast with increasing crack length  $a$ . The comparison of  $\sigma_{rs}$  with the maximum expected operational load, the so called limit load  $\sigma_l$ , defines the critical crack length  $a_c$  at which a catastrophic failure of the structure can be expected under service loads.

As second step a fatigue crack growth analysis is conducted to estimate the crack growth behaviour for a crack with an initial crack length  $a_0$  until reaching the identified critical length  $a_c$ . The initial crack length  $a_0$  is defined as the maximum crack length that can be expected to be present after production. Hence,  $a_0$  is strongly dependent on the production conditions and the employed quality control.

On this basis it is possible now in a third step to establish an inspection program. The chosen inspection method dictates the lower limit for the detectable crack length  $a_d$ . The inspection threshold  $N_{th}$  is defined as the number of flight loading cycles needed to grow a crack with the initial length  $a_0$  to a detectable length of  $a_d$ . This means that  $N_{th}$  represents the earliest operation time after which the presence of detectable cracks can be expected and hence an inspection is needed for the first time. Due to the influence of  $a_0$  and  $a_d$ , the inspection threshold  $N_{th}$  is strongly dependent on both the production conditions and the planned inspection technique. The interval  $N_i$  in which periodical inspections are needed after exceeding  $N_{th}$  can now be defined as the time span that a crack of the length  $a_d$  needs to reach the critical length  $a_c$ . Thus, it is ensured that any crack will be detected before leading to a catastrophic failure of the structure.

The whole damage tolerance analysis of course needs to be supported by experiments to generate a sufficient data basis for the calibration of the used fracture mechanics models and to validate the prediction results for specific, representative cases. Therefore, during the development of new aircraft the scale of experiments reaches from normal lab scale coupon testing in the early design stages to the testing of whole aircraft segments in the final certification stages.

Further details including the discussion of important design parameters like initial crack length, design loads, material selection and geometrical features on the damage tolerance capabilities can be found for example in the online version of the Handbook for Damage Tolerant Design [20].

With regard to the topic of this work it can be stated, that a retardation of the fatigue crack growth without reduction of the residual strength capabilities would lead to improved damage tolerance capabilities in terms of a longer total lifetime before reaching the critical crack length. This improvements could give a direct economic benefit since they lead to longer inspection thresholds and/or a longer inspection intervals. However, as already explained in the beginning, the official acceptance and credit arising from the use of residual stress based life enhancement methods is

currently only limited.

## 2.9 Accepted processes for life enhancement via residual stresses

This section gives a short introduction on accepted residual stress based life enhance techniques. While the cold expansion and shot peening processes are already employed in the aircraft industry for the last decades [1, 17], laser shock peening is perhaps the most promising new technology gaining increasing interest during the last years. The section is closed by a review on research work aiming to used heating as a life enhancement method and a brief comparison of heating to the presented established processes.

### 2.9.1 Cold expansion of holes

Even though a lot of different versions of the process variants have been developed, the basic principle is always the same. An oversized, tapered mandrel is pulled through a hole or a cutout in order to plastically widen it, what leads to the formation of permanent compressive residual stresses around the hole [18]. Figure 2.5 shows the working principle for the so called split sleeve process and the corresponding created residual stress field.

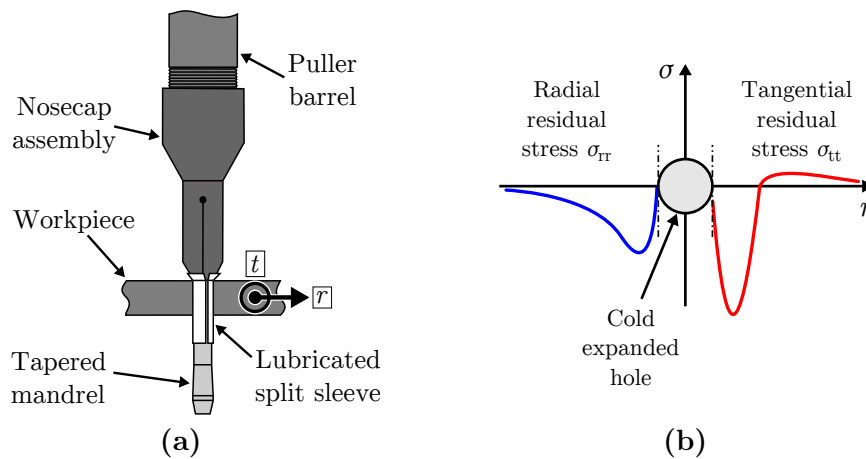


Figure 2.5: (a) Working principle of split sleeve cold expansion process and (b) resulting residual stress state after cold expansion [18, 56].

The cold expansion technique is the most prominent and accepted method introducing compressive residual stresses around fastener holes in the aircraft industry. During the last 30-40 years it has been demonstrated, that significant life extensions can be reached with this technique even when small cracks are already present [17]. Especially for sustaining an ageing aircraft fleet with riveted metallic airframes this process offers an effective and easy to apply method for life extension [18].

### **2.9.2 Shot peening**

Shot peening is maybe the most widely used process for fatigue life enhancement of metallic structures [1]. As shown in Fig. 2.6 small spherical media like glass, ceramic or metal spheres are shot with high speed onto the work piece surface, each causing a local plastic deformation dimple. This procedure results in the formation of compressive residual stresses in a surface near material layer. The compressive residual stresses are balanced out by tensile residual stresses in the core of the workpiece. The depth of layer containing compressive residual stresses is only in the range of some tenths of a millimetre [57].

Hence, shot peening is mainly effective in retarding surface fatigue crack initiation and early crack growth. Since most fatigue cracks in highly loaded aerospace structures and components originate from the surface, shot peening is a feasible and accepted process for fatigue life enhancement of airframe structures and jet engine parts [1, 19, 57, 58]. However, due to the very limited depth of the area of compressive residual stresses, shot peening seems to have only little effect once through thickness cracks are already present [59].

### **2.9.3 Laser shock peening**

Laser shock peening also produces compressive residual stresses in a surface near material layer by a bombardment of the surface. However, as shown in Fig. 2.7 the process principle is different from conventional shot peening.

The workpiece surface is covered with an ablative layer that assures a constant energy absorption and a water film that is transparent for the laser. The irradiation with a high intensity laser pulse leads to the explosive formation of a plasma, creating a shock wave that is travelling along the thickness direction of the workpiece. In the surface near areas where the strains caused by the shock wave exceed the dynamic yield stress, plastic deformation leads to the formation of compressive residual stresses [60].

Compared to the conventional shot peening process, the compressive stress amplitude is in the same range, but the compressive residual stresses reach up to depths in the range of some millimetres. Additionally, laser shock peening results in a rather small surface roughness.

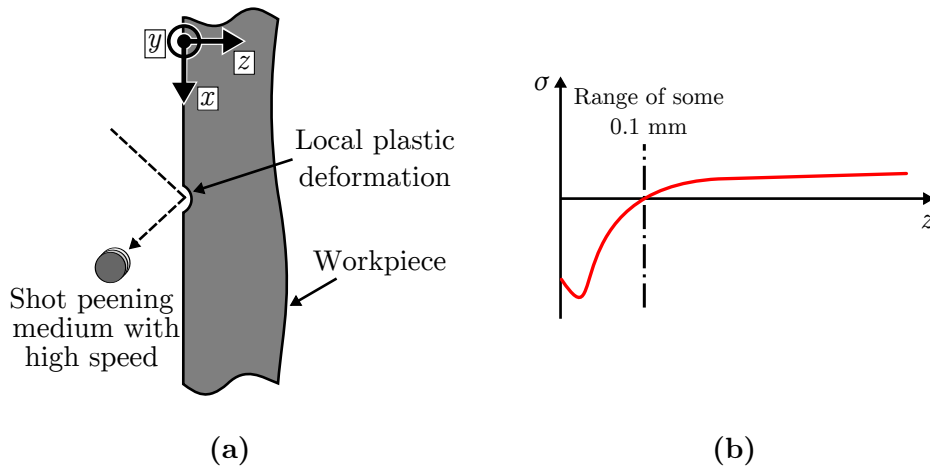


Figure 2.6: (a) Working principle of the shot peening process and (b) resulting residual stress state after shot peening [1, 57].

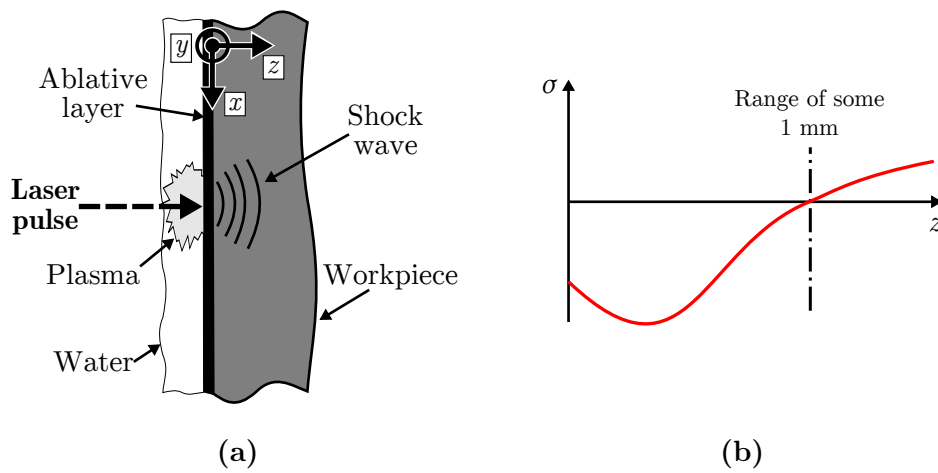


Figure 2.7: (a) Working principle of the laser shock peening process and (b) resulting residual stress state after laser shock peening [1, 60].

Due to these advantages, today laser shock peening is an established process for the fatigue life enhancement of jet engine fan blades [1, 61, 62] and there is ongoing research for applying the process also for the life enhancement of highly stressed thick section aluminium airframe components [63, 64].

Some researchers have found, that in contrast to conventional shot peening, laser shock peening can also be used to retard the growth of long fatigue cracks [59, 65–67]. One main aspect in the conducted studies was to improve the fatigue crack growth behaviour of specimens containing welds and accordingly welding induced residual stresses prior to the laser shock peening [59, 65, 66].

However, the conducted studies using high strength aluminium aircraft alloys used material with a thickness  $b$  in the range of  $6 \text{ mm} < b < 28 \text{ mm}$ . As it seems, there are some problems to successfully apply the process also to thin walled material with a thickness of approximately 2 mm what would be in a realistic range for aircraft fuselage skin applications.

## 2.10 Heating as alternate process for life enhancement

While the heating induced residual stresses are normally seen as detrimental side effect especially from welding, several researchers also examined the possibility of thoughtfully inducing heating residual stresses for the improvement of the fatigue performance of structures and components.

In an early work published by Gurney [21] local spot heating was used as life extension and repair technique. Spot heating was applied to generate different stress states at the run-in and run-out positions of double-fillet welded mild-steel specimens. Significant improvement of the S-N behaviour was found. By comparing the results to those of specimens being subjected to a local mechanical pressing with a punch that produced without any doubt compressive stresses in the critical positions, it was concluded that the observed effect in the heated specimens was mainly due to residual stresses. This work was later taken one step further by Harrison [22]. In this work the spot heating technique was used to repair welded fatigue specimens on which premature cracking was observed at the run-in. It could be shown that by the application of spot heating the fatigue life of specimens could be extended significantly.

Verma and Ray [23–25] carried out some mainly experimentally based work, comparing the observed retardation effects of the fatigue crack growth rates in steel specimens after spot heating to the ones observed after single overloads. They examined the impact of process parameters like spot heating position or heating temperature and concluded that the effects of spot heating and of single overloads can be compared in general. However the underlying physical effects were not further investigated.

Some authors combined the heating and mechanical loading of cracked specimens

and components [68–73]. However, the aim of the proposed procedures was not a direct generation of thermal induced residual stresses. The heating was only applied to promote the plastic yielding under applied load at the crack tip, by lowering the yield stress. This approach showed very promising results. For one case [71] it was even possible to completely arrest a crack in a mild steel plate with an applied stress intensity  $K_{\text{appl}} = 20 \text{ MPa}\sqrt{\text{m}}$ . However, the method is only applicable to specimens or structures already containing cracks or sharp notches and if mechanical loading is easy to perform. If these two conditions are met, it can be a suitable way for fatigue life extension as for example demonstrated for the case of aluminium gas cylinders in [72].

In the work presented by Tsay et al. [26, 27, 29] a laser was used to create heating lines on C(T) specimens made of stainless steel. Afterwards, fatigue crack growth tests were performed. It was concluded that the observed retardation effects were caused by the heating induced residual stresses, since the effect vanished after a stress relieve heat treatment. The experimental work was also accompanied by some simulations [28], in which an analytical approach was used to predict the thermal profile due to heating in conjunction with an elastic-plastic FE model to get an estimate for the induced residual stresses. Even though the development of the residual stress state under subsequent crack extension was studied, no quantitative analysis on the resulting impact on the crack growth rates was performed.

In a study by Jang et al. [30] a gas torch was used to create a heating line on C(T) specimens made of mild steel and fatigue crack growth experiments were performed. Two specimens with different heat inputs were examined and the measured fatigue crack growth was compared to a base material specimen. For the specimen with a high heat input a complete arrest of the crack growth was found, while the specimen with the lower heat input showed a retarded fatigue crack growth compared to the tested base material specimen. The heating induced residual stresses were predicted using thermo-mechanical FE analysis. The resulting model containing the final predicted residual stresses was used in a next step to estimate the opening load of the crack faces as function of the crack length. These calculated opening loads were then used in a crack closure based model for the prediction of the fatigue crack growth. The achieved prediction results indicate, that this approach qualitatively can predict the measured retardation effect. However, the employed crack closure approach for the prediction of fatigue crack growth including the residual stresses is not ideal, since it does not describe the experimental conditions sufficiently. In contrast, the presented basic idea to use a process simulation for the prediction of the residual stresses as basis for the following fracture mechanics simulations is the same as followed in chapter 4 of this work.

In Fig. 2.8a the heating principle is now translated to the process that will be used in this thesis as approach for the retardation of the fatigue crack growth in aircraft aluminium alloy specimens. A heating source, in our case a defocused laser beam,

is used to create a heating line by travelling along the  $y$ -direction on the workpiece surface. The laser as heating tool seems very favourable, since the used automatised systems guarantee a high process stability and reproducibility, while the process itself works contactless. This makes it possible to easily translate the process also to large and/or complex shaped structures. The residual stress state after this treatment is shown in Fig. 2.8b and is very similar to welding residual stresses. However, during heating one goal is to avoid local melting.

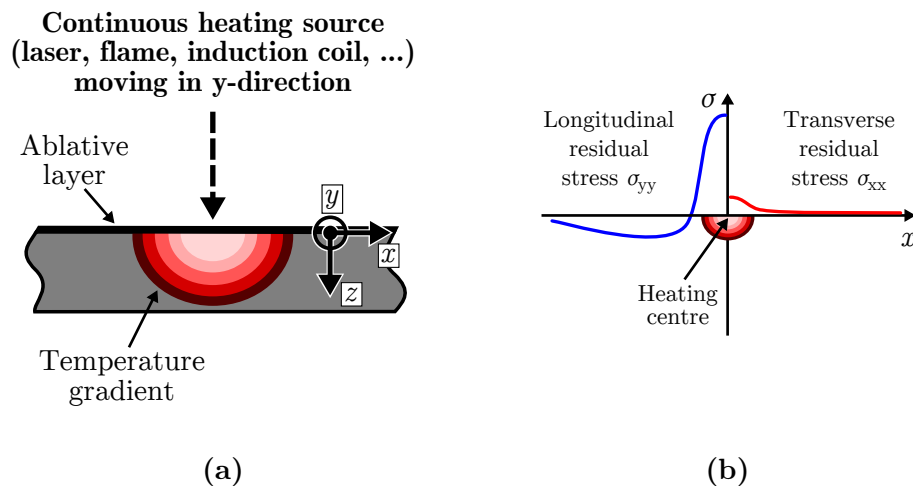


Figure 2.8: (a) Working principle of the heating process and (b) resulting residual stress state after heating with a heat source travelling along the  $y$ -direction.

## 2.11 Comparison of heating and the established processes

As discussed in section 2.2 also the heating induced residual stresses are a result of nonuniform plastic deformation. However, while the established processes create this plastic deformation pure mechanically, during heating it is a result of nonuniform thermal expansion, that leads to local yielding.

With regard to the final residual stress state, it can be stated, that shot peening and laser shock peening create a residual stress gradient through the thickness of the workpiece with compressive stresses near the treated surface and tensile stresses in deeper regions. Cold expansion creates compressive residual stresses in the vicinity of the treated holes with a nearly constant amplitude through the thickness that are balanced out by moderate tensile residual stresses further away. In contrast, heating

produces an area of high tensile residual stresses in the vicinity of the heating area, that cause balancing compressive residual stresses with a moderate amplitude, but in a large surrounding area.

While the cold expansion process due to its working principle is limited to holes and cutouts, the other processes, including heating, can be applied to arbitrary geometries. However, it seems to be difficult to apply the laser shock peening process to thin walled workpieces with a thickness of only some millimetres.

While shot peening only retards effectively the initiation and early growth of surface cracks, laser shock peening, cold expansion and heating can be used also for the retardation of the growth of present through thickness cracks. This makes them in particular interesting in the context of damage tolerance, since here the basis for the evaluation is always an initial small macroscopic flaw or crack.

Shot peening and cold expansion have already been used for the last decades in the aircraft production and maintenance. Laser shock peening can be seen as a promising new approach with a broad potential application field. While laser shock peening is already an established process in the production and enhancement of jet engine parts, the application to other structural airframe components is subject of ongoing research work. In contrast, life enhancement by heating has so far found little attention for aircraft applications.

The possibility to create through thickness compressive residual stresses in large areas makes the heating process unique compared to the other approaches. Thus, heating has the potential to be applied for application cases that are so far not covered by the established processes. Therefore, the presented work aims to demonstrate the applicability and effectiveness of the heating method in order to retard fatigue crack growth in aircraft aluminium structures.



## 3 Laser heating - Proof of concept

In this chapter the experimental proof of concept that laser heating can be used to retard the fatigue crack growth in aircraft aluminium alloys is given.

A defocused laser is used to create one heating line on aluminium C(T)100 specimens at a given distance to the crack tip. After some remarks on the used material and the specimen design, the details on the process are given followed by the results of the experimental characterisation of the transient temperature fields via thermocouple measurements. The resulting influence on micro structure, hardness, tensile properties, residual stresses and, most important, fatigue crack growth was measured and compared to the original base material properties.

### 3.1 Material: Aluminium-Lithium alloy 2198

Up to the solubility limit, each weight percent addition of lithium to aluminium alloys decreases the specific weight by approximately 3 % and increases the elastic modulus by approximately 5 % [43, 74–77] what makes Al-Li-alloys very interesting for aircraft applications.

A first generation of Al-Li alloys was developed in the 1950s and 1960s mainly for military aircraft applications [77]. The two most prominent alloys were the Al-Cu-Li alloy 2020 (USA) and the Al-Mg-Li alloy 1420 (Russia). Both with a high specific strength and elastic modulus, but suffering from low ductility and low fracture toughness [74, 75, 77]. This shortcomings could be linked to strain localisations due to the employed main strengthening phase  $\delta'$  ( $Al_3Cu$ ) and the formation of precipitation free zones next to the grain boundaries [74, 75]. The underlying effects are described in [75] and [74].

In the 1980s a second generation of high lithium containing alloys (2.0–2.5 wt.% Li) like 8090, 2090, 2091, 1446 and 1460 were developed. These alloys provided high density benefits up to 10% and contained additionally to  $\delta'$  the precipitated phases  $T_1$  ( $Al_2CuLi$ ) and/or S ( $Al_2CuMg$ ), which improved to some extent the fracture toughness. However, although used for some fighter jet and helicopter applications this second generation alloys had only limited commercial success [74, 77].

The latest generation of Al-Li alloys was developed in the 1990s. In comparison to the prior alloys, they show an improved ductility and fracture toughness due to a reduction of the Li content (< 2.0 wt.% Li). In these alloys the main strengthening

Table 3.1: Chemical composition of AA2198 (wt.%) [76, 78].

Cu	Li	Zn	Mn	Mg	Zr	Si	Ag	Fe
2.9 – 3.5	0.8 – 1.1	≤ 0.35	≤ 0.5	0.25 – 0.8	0.04 – 0.18	≤ 0.08	0.1 – 0.5	≤ 0.01

phase was  $T_1$  ( $Al_2CuLi$ ). Alloys like 2195, 2x96, 2x97 and 2098 gained commercial application mostly in the USA. These alloys were able to match the balance between strength and damage tolerance of standard aircraft alloys like 2024 or 7050 [77].

However, recent metallic airframes use more advanced high strength and high damage tolerant alloys. For this reason the Al-Cu-Mg-Li alloy 2198 was developed by Alcan (since 2011 Constellium) as new aircraft skin material with the goal to reach a higher static strength than AA7475 and better damage tolerance capabilities than AA2524 [76, 77]. The alloy 2198 is a derivative of AA2098 with a lower copper content, some other minor chemistry adoptions and an optimised thermo-mechanical processing [76]. The limits for the chemical composition are given in Table 3.1.

The thermo-mechanical treatment during the production leads to a microstructure consisting of very flat, pancake-like grains lying in the L-T plane, and a pronounced anisotropy of the mechanical properties [78].

It is very probable that AA2198 will be used in future metallic aircraft structures, since it provides attractive mechanical properties and it is weldable via laser beam welding and friction stir welding [76, 77, 79]. Therefore, this new alloy was used for the presented work.

## 3.2 Specimen design

A batch of C(T)100 specimens in the L-T orientation with a notch length  $a_0 = 20$  mm as well as rectangular pieces of the size 125 mm x 120 mm were produced from a sheet of AA2198 in T3 temper with a nominal thickness of 5 mm. Afterwards, a heat treatment to reach T8 temper was conducted. The dimensions of the C(T)100 specimens were in accordance with ASTM E647 [51] as shown in Fig. 3.1a. However, the thickness of only 5 mm is lower than the standard requirements but common for thin sheet testing.

During the fatigue crack growth experiments, the majority of tested specimens unfortunately showed such severe deviations of the crack path that a clear evaluation of the results according to ASTM E647 [51] was questionable. Therefore, a second batch of specimens with the same dimensions but in the T-L orientation was prepared from the same AA2198 sheet as used before and the fatigue crack growth tests were repeated. Even though some crack deviation could also be observed for this second series of tests, it was significantly less pronounced than in the first series. Hence, the

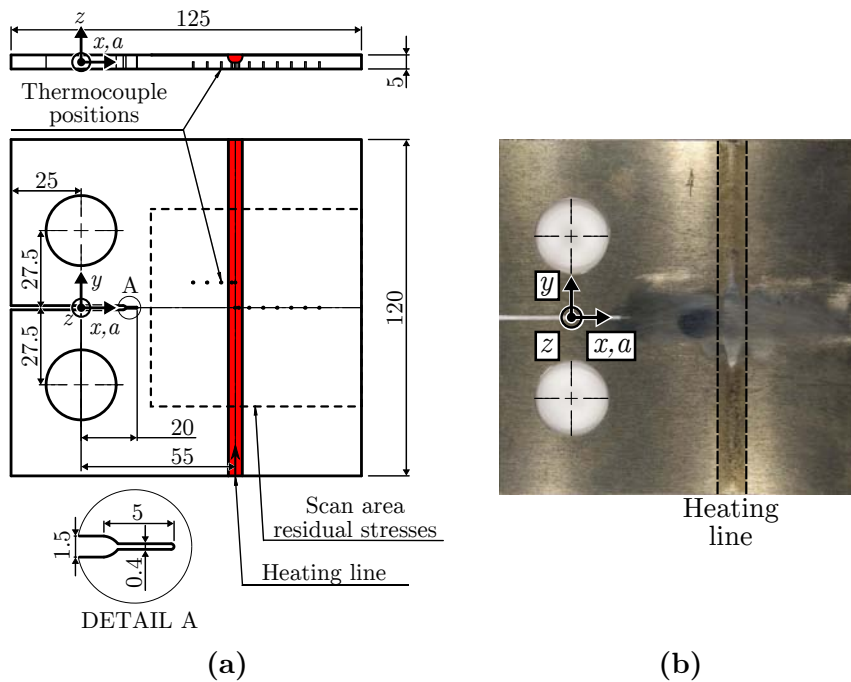


Figure 3.1: (a) Sketch of the C(T)100 specimen geometry with the corresponding coordinate definitions (measures given are in millimetres). (b) Picture of a laser heated AA2198 T8 C(T)100 specimen before the fatigue testing. The specimen surface along the expected crack path has been manually polished for the optical crack length measurements.

results from the second test series in T-L orientation are presented in section 3.9. In this section also a comparison of the measured base material fatigue crack growth is given for T-L and L-T orientation to demonstrate that the properties in both orientations are comparable.

With regard to the specimen naming the following system was used. All specimen names start with a prefix BM for base material or LH for laser heated specimens, which is followed by a suffix consisting of a code for the performed experiment (thermo couple measurement (TC), macro cross section (CS), micro hardness measurements (MH), tensile test (TT), residual stress measurements (RS) or fatigue crack growth test (FCG)). When needed, the name was extended by a further suffix to indicate the material temper, the specimen orientation or the exact measurement position, for example heating zone (HZ), heat affected zone (HAZ) or area with base material properties (BM).

### 3.3 Laser heating process

Following the principle introduced in section 2.10, for the performed experiments a Nd:YAG laser was used to produce a line of laser heating on the surface of the prepared C(T)100 specimens. For this, the laser travelled with a constant speed of  $v_y = 3.33$  mm/s in positive  $y$ -direction from one edge of the specimen to the other. Figure 3.2 shows photographs of the set-up used for laser heating.

The same process parameter set was used for all specimens with the heating line centre positioned at  $x_h = 55$  mm. Since the goal was to apply the heating without local melting of the material, a welding optic was used, but the working distance was increased to obtain a laser spot diameter of approximately 5 mm.

On the irradiated surface a layer of silicon carbide powder with a thickness of 0.5 mm was placed to ensure an equal absorption of the laser light for all specimens

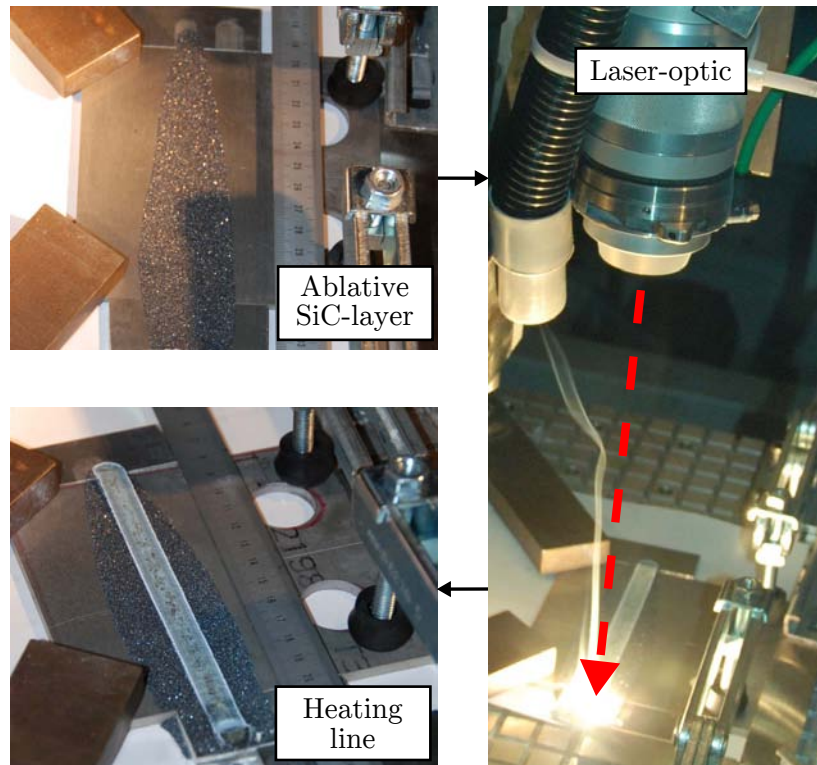


Figure 3.2: Used laser heating process. Before heating, the heating area was covered with an ablative SiC powder layer.

as shown in Fig. 3.2. After the treatment a slight out of plane distortion of the specimens in the range of approximately 1 mm could be observed. As shown in Fig. 3.1b, along the heating line a slight colour change on the surface with a slight roughness increase could be observed, but no signs of melting were found.

### 3.4 Thermocouple measurements

The transient temperature distribution during laser heating was characterised using 12 type K thermocouples. The thermocouples were placed in the prepared rectangular pieces of AA2198 T8 having the outer dimensions of C(T)100 specimens as shown in Fig. 3.3.

Table 3.2 gives the exact positioning of the thermocouples. They were placed in holes drilled to a depth of half the specimen thickness from the far side of the laser heating as indicated in Fig. 3.1a. For the data acquisition a computer-based measurement system with a sampling rate of 400 Hz was used.

Figure 3.4a shows the measured transient temperature cycles for three selected thermocouple positions. The time axis in Fig. 3.4a was adjusted in a way that the peak temperature for the thermocouple position TC-12 was reached at  $t = 0$  s.

Figure 3.4b shows the extracted peak temperature  $T_{max}$  as function of the  $x$ -position of the thermocouples. The  $T_{max}$  distribution is symmetrical around the centre of the heating zone (HZ) at  $x_h = 55$  mm, where it reaches a maximum of approximately 380°C. Only one of the thermocouples at this position shows a significant lower  $T_{max}$ , compared to the other three in the middle of the HZ. This is a

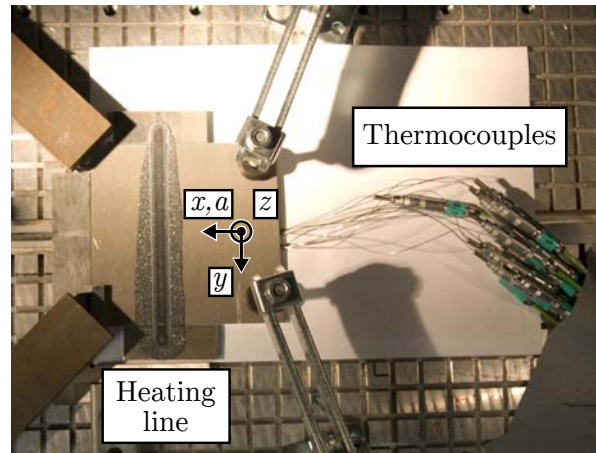
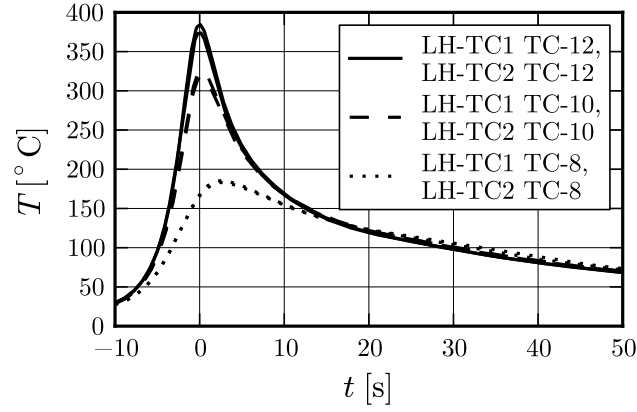


Figure 3.3: Measurement set-up for the thermocouple measurements of the laser heating process.

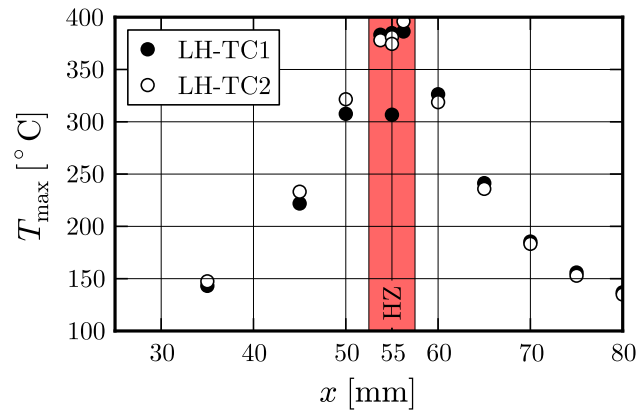
Table 3.2: Thermocouple positions

TC Name	$x$ [mm]	$y$ [mm]	$z$ [mm]
TC-1	55.00	9.00	0.00
TC-2	53.75	9.00	0.00
TC-3	50.00	9.00	0.00
TC-4	45.00	9.00	0.00
TC-5	35.00	9.00	0.00
TC-6	80.00	0.00	0.00
TC-7	75.00	0.00	0.00
TC-8	70.00	0.00	0.00
TC-9	65.00	0.00	0.00
TC-10	60.00	0.00	0.00
TC-11	56.25	0.00	0.00
TC-12	55.00	0.00	0.00

measurement error due to a loss of thermal contact between specimen and thermocouple in the drilled hole. In general, the results of the two individual measurements LH-TC-1 and LH-TC-2 are in good agreement.



(a)



(b)

Figure 3.4: Thermocouple measurements results for the two specimens LH-TC1 and LH-TC2. (a) Measured temperature cycles for three of the thermocouple positions given in Table 3.2 and (b) extracted peak temperature  $T_{\max}$  as function of the  $x$ -position. The shaded area indicates the lateral extension of the heating zone (HZ) that corresponds to the spot diameter of the defocused laser.

### 3.5 Microscopical examinations

The resulting microstructure after laser heating was studied using a light optical microscope (OM) and a scanning electron microscope (SEM) in conjunction with the electron back scatter diffraction technique (EBSD).

Figure 3.5 shows a light optical microscope picture of the laser heating area cut from the specimen LH-CS. The depicted vertical structuring is due to the elongated pancake-like grain structure, resulting from the thermo-mechanical treatment during the production. Only beneath the laser irradiated surface area, that is indicated by the white arrows, a slight colour change can be seen in a semi elliptical area. However, no signs of partial melting or surface crack formation can be found.

Figure 3.6 shows two scanning electron microscope (SEM) pictures of the grain structure in the same specimen using the EBSD technique to distinguish different grains. In Fig. 3.6a the grain structure for a position far away from the heating zone is shown, being representative for the base material grain structure (BM). It consists of layers of elongated grains in the  $x$ -direction. Figure 3.6b shows a corresponding area directly from the heating zone (HZ). Here, additionally to the large elongated grains, many small grains can be found. The formation of small grains in the HZ indicates a thermally activated partial recrystallisation of this area.

### 3.6 Micro hardness measurements

Changes of the local mechanical properties due to the laser heating were measured via micro hardness measurements using the set-up shown in Fig. 3.7. For each indent with the Vickers indenter a load of 0.2 kp with a hold time of 20 s was used.

Figure 3.8a shows a false colour plot of the results of a micro hardness area scan performed on the specimen LH-MH. As seen, a significant drop of the micro hardness can be found in the area beneath the laser irradiated surface. Figure 3.8b shows the results for  $z = 1.8$  mm as line plot. The dark shaded area indicates the lateral extension of the heating zone (HZ) with  $52.5 \text{ mm} < x < 57.5 \text{ mm}$ . The hardness drop is limited to a heat affected zone (HAZ) with  $45.0 \text{ mm} < x < 65.0 \text{ mm}$ , which is marked light shaded in Fig. 3.8b. The remaining part of the specimen shows the hardness of the base material (BM).

The micro hardness measurements indicate a clear change of the mechanical properties in the area of the HAZ and the HZ. In this area the hardness drops from the base material value of approximately 155 HV 0.2 kp to approximately 100 HV 0.2 kp. However, the observed severe changes of the hardness are not very likely to be the result of the observed changes in the grain structure.

As the performed thermocouple measurements showed (see Fig. 3.4), in the HAZ and the HZ peak temperatures of  $225^\circ\text{C} < T_{max} < 380^\circ\text{C}$  have been reached. These

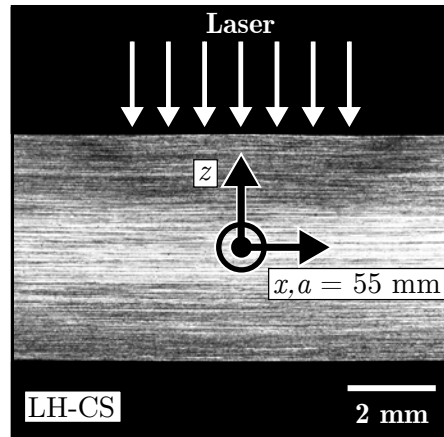


Figure 3.5: Cross section macrograph ( $x$ - $z$  plane) of the specimen LH-CS at the indicated heating line centre position  $x_{heating} = 55$  mm.

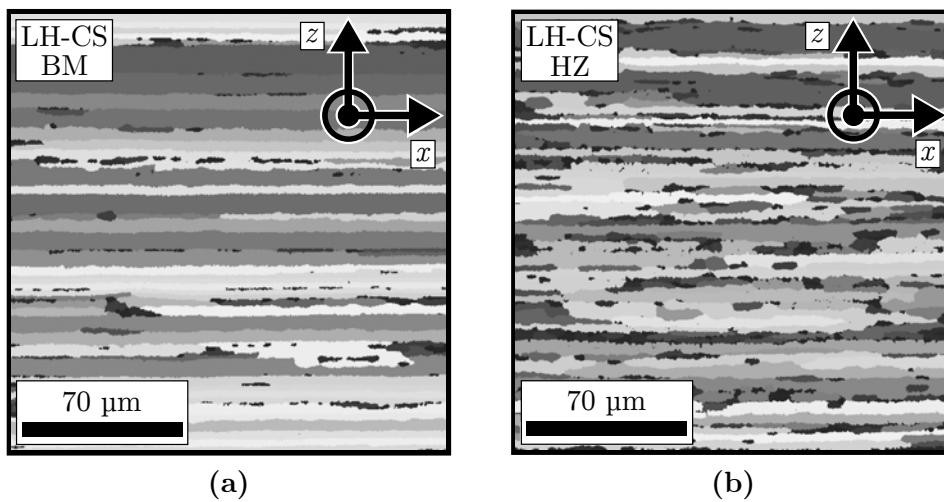


Figure 3.6: Grain structure of the specimen LH-CS after laser heating: (a) position far away from the heating zone and (b) in the heating zone. Different grey values indicate different grains.

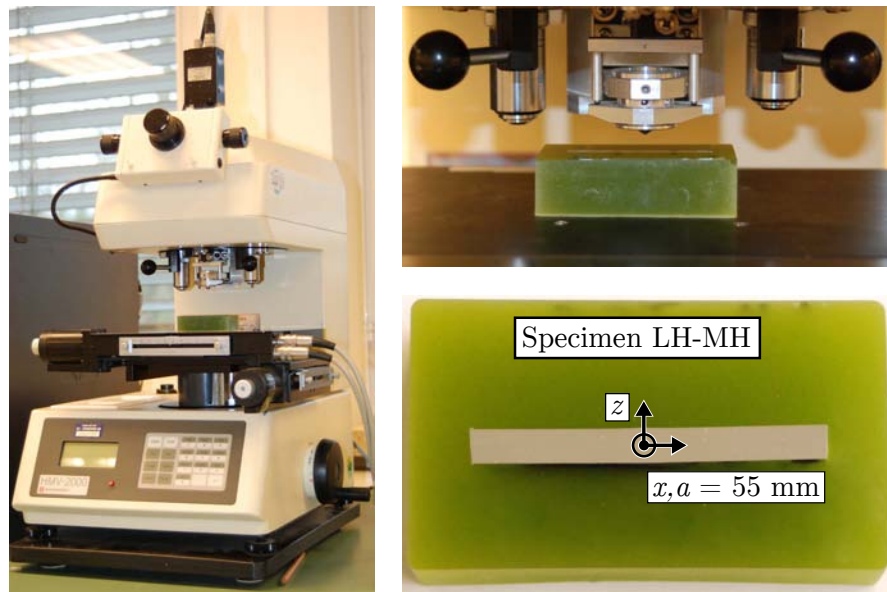


Figure 3.7: Set-up for the micro hardness measurements.

temperatures are way above the normal tempering temperatures used for this material. This suggests that the excessive heating in HAZ and HZ most likely changed the precipitation state substantially, what explains the measured drop of the hardness in this areas.

### 3.7 Tensile tests

Tensile tests specimens were produced from the same sheet of AA2198 used for the C(T)100 specimens according to DIN 50125 [80] and EN 10002 [81]. Base material tests for T8 and T3 temper were performed for rolling (L) and transverse (T) direction. To gain an estimate on the influence of the laser heating on the static strength an additional set of specimens was manufactured from a piece of AA2198 T8 containing one heating line. As shown in Fig. 3.9, this specimens were oriented in the rolling direction (L) with the heating area lying in the middle of the gauge length.

For each configuration three specimens were tested using a Schenck-Trebel RM100 testing machine modernised with a Zwick Dups controlling unit and a Fiedler WS-160 laser extensometer as shown in Fig. 3.9. The tests were conducted with a constant cross head speed and for all the tests an initial gauge length  $l_0 \approx 80$  mm was used.

Figure 3.10a shows the results of the base material characterisation. In general, the peak aged T8 condition shows a higher yield strength  $\sigma_{ys}$  and a less pronounced

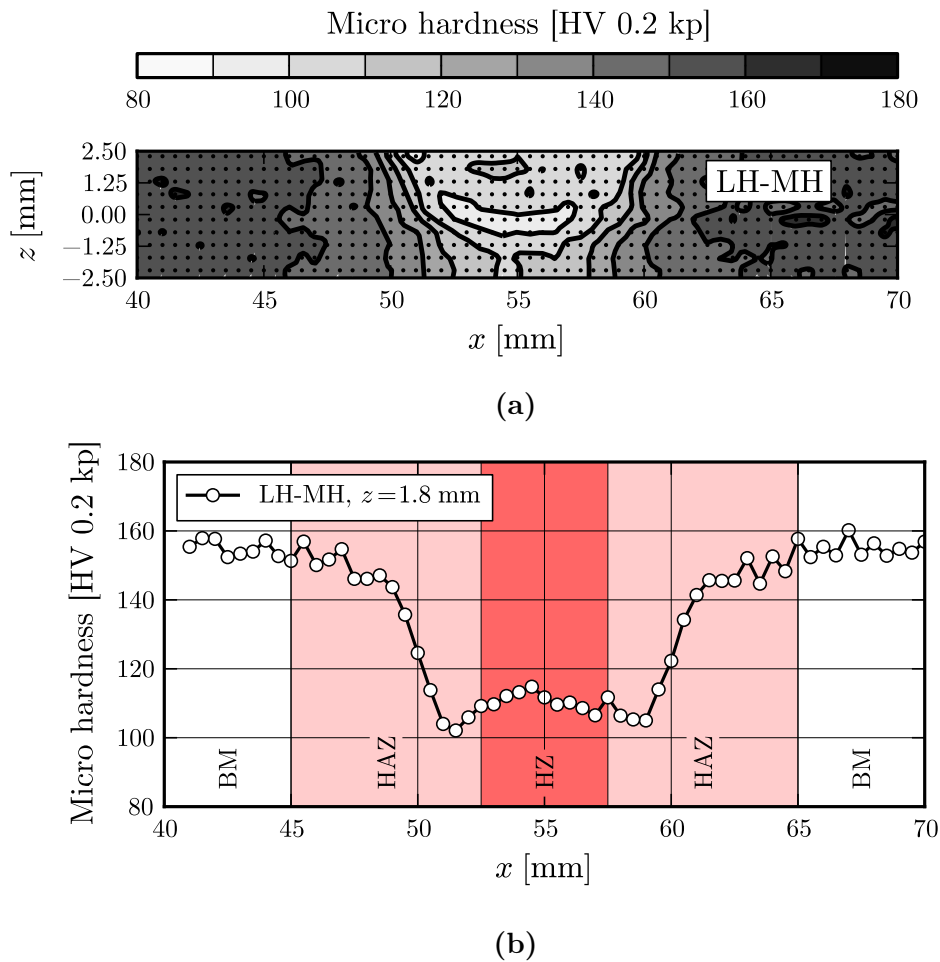


Figure 3.8: (a) Measured micro hardness area scan for the specimen LH-MH. The black dots indicate the measurement positions. The contours were created using a natural neighbour interpolation. (b) Line scan of the micro hardness for  $z = 1.8$  mm. Shaded in different colours are the lateral extensions of the heating zone (HZ), the heat affected zone (HAZ) and the remaining area with base material properties (BM).

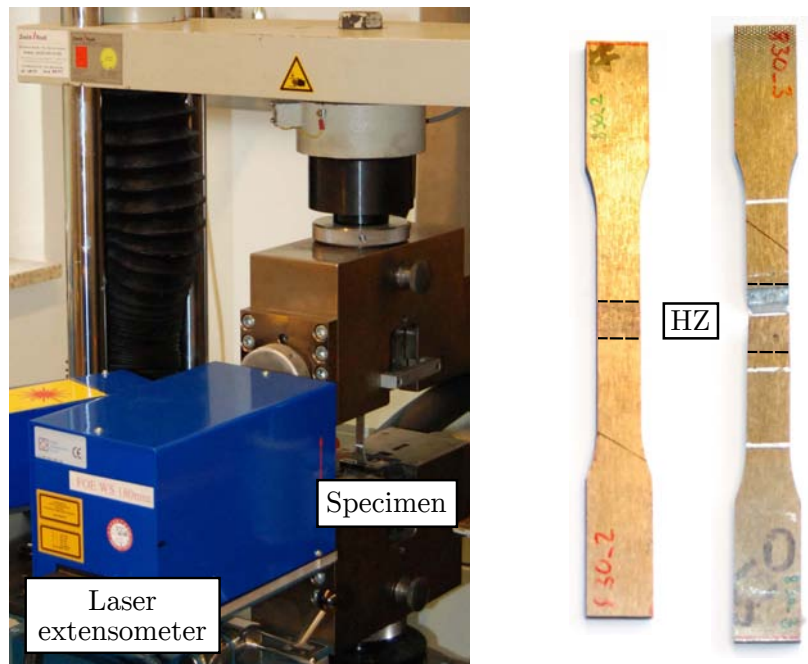
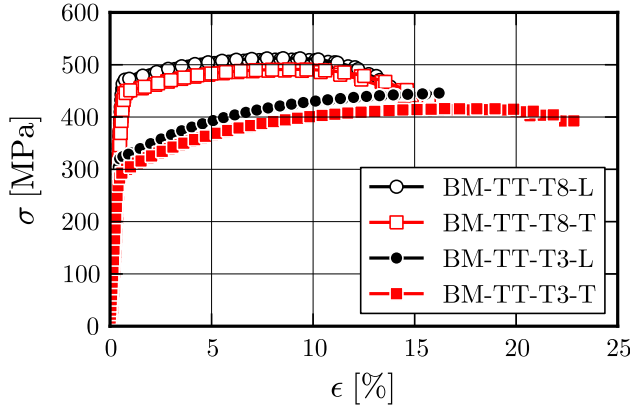


Figure 3.9: Set-up for the tensile test and pictures of two specimens containing a laser heating line.

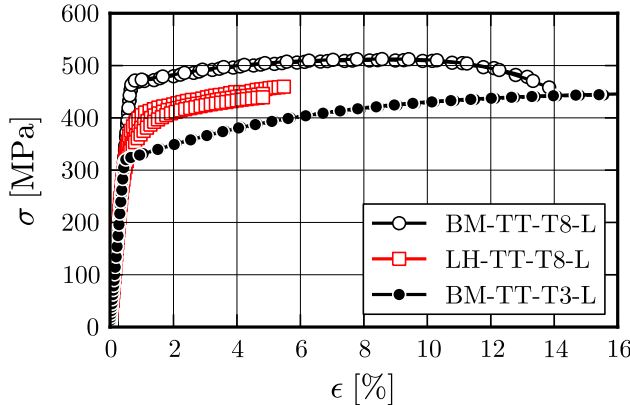
hardening behaviour compared to the solution heat treated, cold worked T3 temper. For both tempers the whole stress-strain-curves for the tests in L-direction are slightly above the ones from the tests in T-direction.

In Fig. 3.10b the results of the laser heated specimens are compared to the corresponding base material results. Table 3.3 gives the Young's modulus  $E$ , the yield stress  $\sigma_{ys}$  (0.2% plastic strain) and the ultimate tensile strength  $\sigma_{uts}$  calculated from the measurement data for all specimens in comparison to literature values for the base material taken from [78, 82]. For both the T3 and T8 temper the results are in good agreement with the published values.

As shown in Fig. 3.10b, the stress-strain curves measured for the specimens containing a laser heating line (LH-TT-T8-L) are lying between the base material curves for T8 and T3 temper. This behaviour can be explained as result of the local softening due to a change of the precipitation state in HZ and HAZ as indicated by the micro hardness measurement presented in section 3.6. The observed reduction of the elongation at fracture is also a result of the local softening. The local softening leads to a localisation of the plastic yielding in the heating area, which is comparatively small with regard to the total gauge length.



(a)



(b)

Figure 3.10: Tensile test results for AA2198 specimens (a) base material specimens in T8 L-direction, T3 L-direction, T8 T-direction, T3 T-direction. (b) T8 specimens containing a laser heating line in the middle of the gauge length compared to the base material specimens in L-direction. For clarity, only every 60th point of the measurement data is shown.

Table 3.3: Tensile test results in comparison to literature values [78, 82].

Temper	Orientation	Data	$E$ [GPa]	$\sigma_{ys}$ [MPa]	$\sigma_{uts}$ [MPa]
T8	L	BM-TT-T8-L	71	470	511
T8	L	[82]	71	475	516
T8	L	[78]	–	490	530
T8	T	BM-TT-T8-T	72	449	490
T8	T	[82]	71	450	499
T8	T	[78]	–	470	512
T3	L	BM-TT-T3-L	71	324	445
T3	L	[78]	–	324	442
T3	T	BM-TT-T3-T	72	294	416
T3	T	[78]	–	300	416
T8 & LH	L	LH-TT-T8-L	74	356	448

### 3.8 Residual stress measurements

Prior to the residual stress measurements, a fatigue crack with a length of  $a = 30$  mm was grown in the examined laser heated specimen (LH-RS) under the same loading conditions that were later also used for the fatigue crack growth experiments. Thus, the specimen was subjected to 240 000 loading cycles before the residual stress measurements were carried out. The synchrotron diffraction experiments were performed at the HARWI II beamline of HZG at DESY with a photon energy of 70 keV and a beam cross section of 1 mm x 1 mm. A Mar555 area detector was used to record several complete diffraction rings. Approximately 1000 single pictures were recorded for a scan of the area in front of the crack tip. Copper paste was placed on one side of the specimen, covering the whole scan area marked in Fig. 3.1a. Figure 3.11 shows the measurement set-up, the prepared specimen and an example detector picture.

For the evaluation of the detector data, a routine in the programming language Python was written that allows using the information of the complete measured Al-{311} ring for the calculations. As first step in the evaluation, the detector data was transformed from Cartesian coordinates  $(x,y,z)$  into spherical coordinates  $(r,\theta)$ . Then, it was divided into 720 small sectors, each representing one individual direction  $\theta$ .

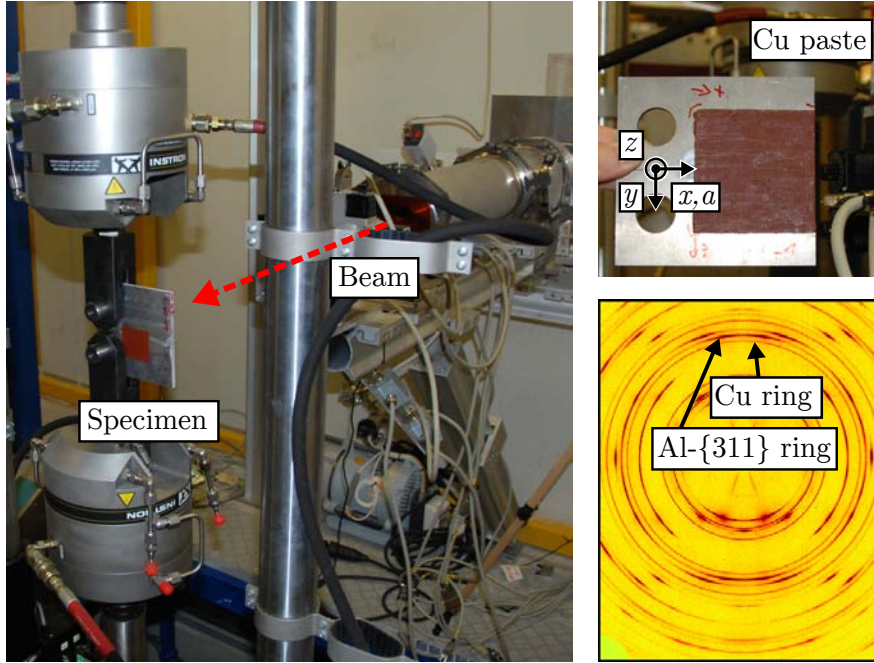


Figure 3.11: Set-up for the residual stress measurements. The detector is not shown in the picture. It was placed approximately 1 m behind the specimen to record several complete diffraction rings as shown in the example detector picture where dark colours indicate high measured photon intensities. In the upper right corner, a close-up view of the examined specimen with copper paste on its backside is shown.

As a next step, the shift of the Al- $\{311\}$  peak and the resulting elastic strain in the corresponding  $\theta$ -direction  $\epsilon'(\theta)$  were calculated for each sector. During this calculation step, the relative position of the Al- $\{311\}$  peak in comparison to the neighbouring copper peak was used, instead of the absolute position of the Al- $\{311\}$  peak. This way, the calculation results become insensitive to specimen misalignment or distortions.

In a final step, an optimisation algorithm was used to get the best fit for the global strains  $\epsilon_{xx}$ ,  $\epsilon_{yy}$  and  $\epsilon_{xy}$  using the 720 individually calculated  $\epsilon'(\theta)$ :

$$\epsilon'(\theta) = \epsilon_{xx} \cos^2(\theta) + \epsilon_{xy} \sin(2\theta) + \epsilon_{yy} \sin^2(\theta) \quad (3.1)$$

For the following calculations of the resulting stresses, a Young's modulus  $E = 70$  GPa and a Poisson's ratio  $\nu = 0.35$  were assumed. The stress-free lattice parameter was manually adjusted to  $d_0 = 1.217$  Å in a way that the transverse residual stresses  $\sigma_{xx}$

became zero at the specimen edge ( $x = 100$  mm).

As known from measurement results for aluminium welds [14, 83], the heating induced change of the precipitation state in HZ and HAZ also leads to a variation of the stress-free lattice parameter, what has a substantial effect on the calculated absolute values of the single residual stress components. However, the influence of a change of the stress-free lattice parameter on the calculated stress differences  $\Delta\sigma = \sigma_{yy} - \sigma_{xx}$  is negligible. Hence, the whole presented discussion is based on  $\Delta\sigma$ . Since the transverse residual stresses  $\sigma_{xx}$  are expected to be very small [14, 83],  $\Delta\sigma$  represents primarily the state of the longitudinal residual stress component  $\sigma_{yy}$ .

The results obtained after the evaluation of the raw data represent averaged values for the stresses in the gauge volume of 1 mm x 1 mm x 5 mm. This means that a gradient of the stress state in  $z$ -direction can not be decomposed and the measured stress values give an average through the whole specimen thickness.

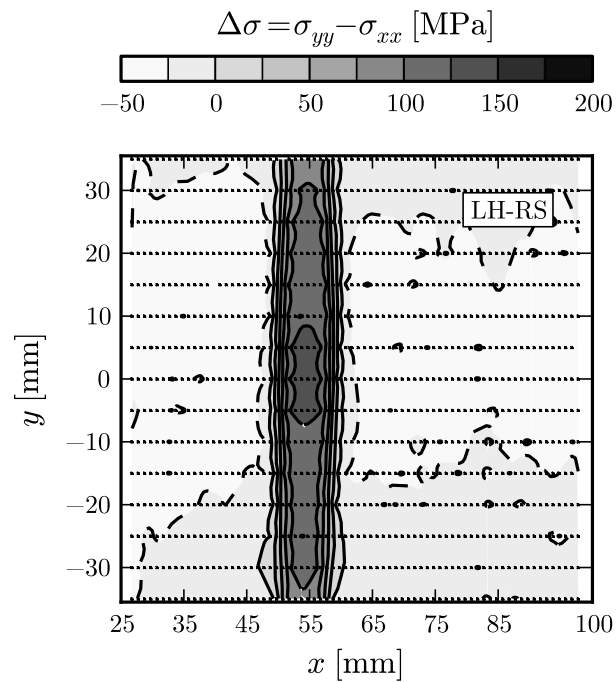
Figure 3.12a shows a contour plot of  $\Delta\sigma = \sigma_{yy} - \sigma_{xx}$  for the specimen LH-RS. Figure 3.12b shows the results as line scan by averaging the corresponding data over  $y$  in the bounds of  $-12$  mm to  $12$  mm for each position  $x$ . As seen, high positive values of  $\Delta\sigma$  can be found in the HZ and HAZ, indicating high tensile longitudinal residual stresses  $\sigma_{yy}$ . In the surrounding areas moderate negative values of  $\Delta\sigma$  can be seen, indicating compressive longitudinal residual stresses  $\sigma_{yy}$ .

An almost constant  $\Delta\sigma \approx -30$  MPa can be found for  $30$  mm  $< x < 47$  mm. The value of  $\Delta\sigma$  increases then from  $x = 47$  mm onwards, change sign at  $x = 49$  mm and reach a maximum plateau of 130 MPa between  $52$  mm  $< x < 57$  mm what corresponds approximately to the lateral extension of the HZ. With increasing  $x$ -position the values of  $\Delta\sigma$  drop again, change the sign to negative values at  $x = 60$  mm and reach an almost constant level of  $\Delta\sigma \approx -30$  MPa again for  $x \geq 62$  mm.

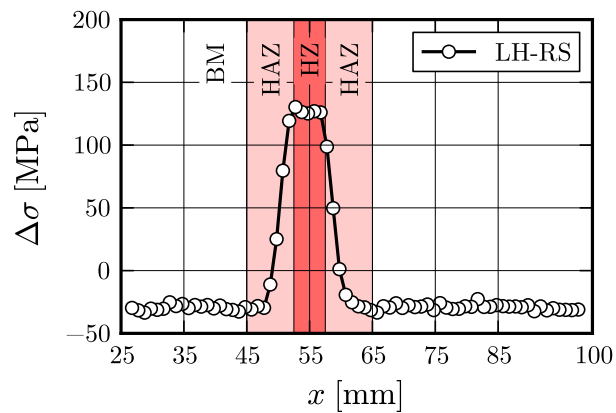
### 3.9 Fatigue crack growth tests

Fatigue crack growth experiments were performed force controlled under constant amplitude loading conditions using a servo hydraulic testing machine as shown in Fig. 3.13. The crack length was monitored directly via optical measurements and indirectly via a clip gauge spanned over the notch, that recorded the opening of the notch faces. On basis of the optical crack length measurement results, a polynomial fitting function was established to convert the clip data into crack length data.

For the calculation of the crack growth rates, the incremental polynomial method as recommended in ASTM E647 Appendix X1.2 [51] with a fitting half window size  $n = 4$  was used. To suppress any effect of fatigue crack initiation at the initial notch tip ( $a_0 = 20$  mm), the number of loading cycles  $N$  was reset to zero in the evaluation for all specimens after the crack reached a length of  $a = 25$  mm.



(a)



(b)

Figure 3.12: (a) Measured area scan of the mean stress difference  $\Delta\sigma$  for the specimen LH-RS. The black dots indicate the measurement positions, while the contours were created using a natural neighbour interpolation. (b) Line scan computed by averaging the area scan data in  $y$  direction in the bounds of  $-12$  mm to  $12$  mm.

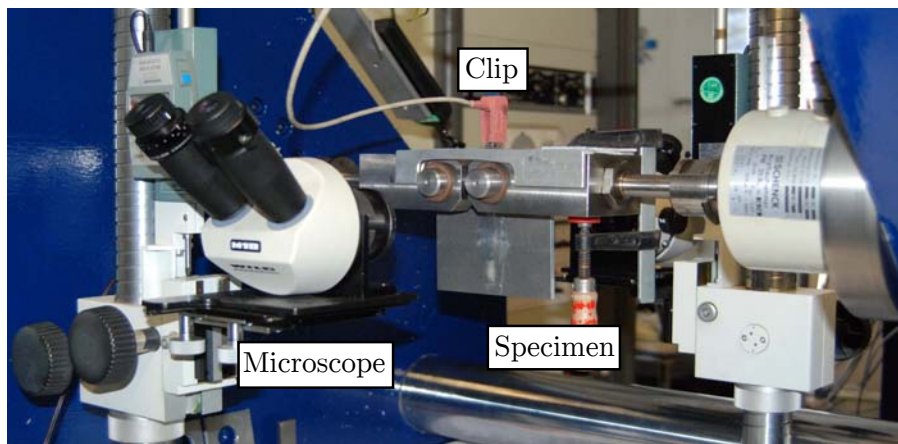


Figure 3.13: Set-up for the fatigue crack growth measurements.

### 3.9.1 Calibration of the Walker equation

For the use in the numerical predictions the Walker equation given in Eq. 2.25, was calibrated for the used material AA2198 in T8 temper. Therefore, fatigue crack growth tests were performed for five base material specimens with constant stress intensity factor ratios  $R$  (two specimens  $R = 0.01$ , two specimens  $R = 0.1$ , one specimen  $R = 0.7$ ). These tests were conducted in T-L orientation and the fatigue crack growth rates were calculated. Based on this data the best fit for the three material parameters  $C$ ,  $n$  and  $m$  of the Walker equation was identified, using an optimisation routine minimising the least square error between measurement data and Walker equation prediction. Figure 3.14 shows the measurement and the corresponding predicted fatigue crack growth rates using the identified best fit for the material parameters  $n = 2.80$ ,  $m = 0.67$  and  $C = 1.15 \cdot 10^{-10}$  m/cycle.

Additionally, in Fig. 3.14 the FCG data from the only valid base material test in L-T orientation with  $R = 0.1$  is shown. This data was not used during the calibration of the Walker equation. The measured fatigue crack growth rate in L-T direction is only slightly lower than in T-L orientation under same loading conditions. In general, the crack growth rate for both orientations is comparable.

### 3.9.2 Comparison of base material and laser heated specimens

The tests comparing the fatigue crack growth of base material and laser heated specimens were performed under constant amplitude loading with  $F_{max} = 4.41$  kN and  $R = 0.1$ . This way  $\Delta K_{appl}$  changes gradually between  $13 \text{ MPa}\sqrt{\text{m}} \leq \Delta K_{appl} \leq 35 \text{ MPa}\sqrt{\text{m}}$  for  $25 \text{ mm} \leq a \leq 60 \text{ mm}$ . This lays in the typical load range for damage

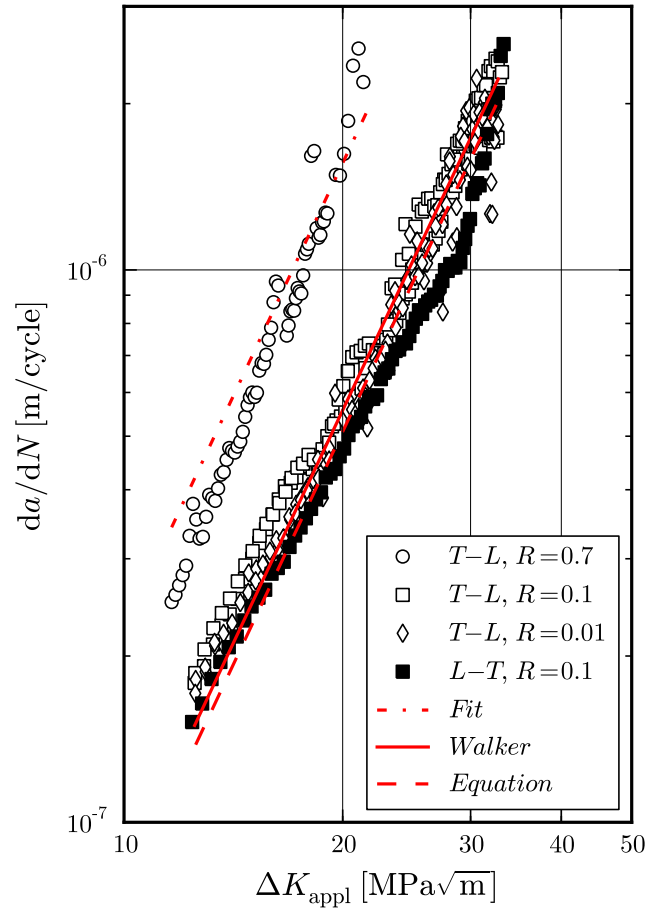


Figure 3.14: Calibration of the Walker equation for AA2198 T8 in T-L orientation. The open symbols show the measured  $da/dN$  for the base material specimens in T-L orientation. The filled black square symbols show the results for one base material specimen in L-T orientation. The lines show the best fit of the Walker equation based on the measurement data in T-L orientation. For clarity, only every 5th point of the measurement data is shown.

tolerance tests of primary aluminium aircraft structural members.

Table 3.4 contains the measured maximum crack deviations for the tested specimens. All deviations lay within the validity threshold of  $20^\circ$  defined in ASTM E647 [51].

Figure 3.15a shows the measured crack length  $a$  as a function of the loading cycles  $N$  for two base material specimens and three laser heated specimens. The crack growth of the two base material specimens (BM-FCG) is shown as open diamond symbols. Compared to the behaviour of the base material specimens the crack growth in the laser heated (LH-FCG) specimens is substantial slower, as can be seen from the higher number of cycles needed for reaching the final crack length.

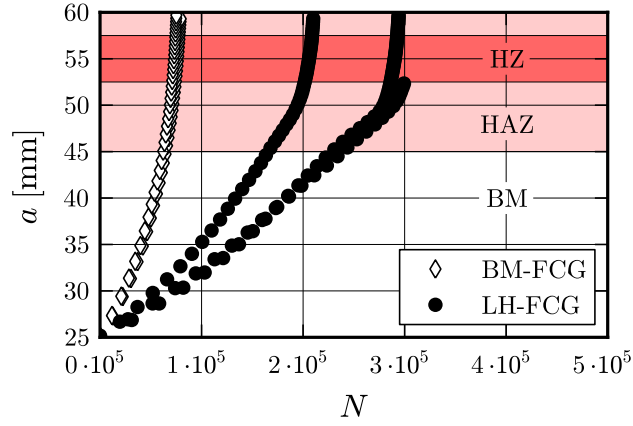
Figure 3.15b presents the crack growth rates calculated on basis of the data shown in Fig. 3.15a. For the base material specimens a nearly linear dependence between crack growth rate and crack length can be found in the semi-logarithmic plot. For the laser heated specimens a nearly constant shift downwards on the  $da/dN$ -axis can be seen, until the crack growth rates start to increase at  $a = 48$  mm and nearly reach the same values as for the base material specimens at  $a = 58$  mm.

While the measurement curves of the base material specimens basically overlap each other, one of the three laser heated specimens shows a slightly faster crack growth than the two others. As discussed later in chapter 5, this behaviour can be explained by slight changes of the process conditions during the specimen manufacturing. This conclusion seems plausible, since the specimen showing the faster crack growth (LH-FCG-11) was manufactured in a different batch approximately two years after the two other specimens (LH-FCG-2, LH-FCG-3). This points out, that future work has to address the issue of process control and repeatability.

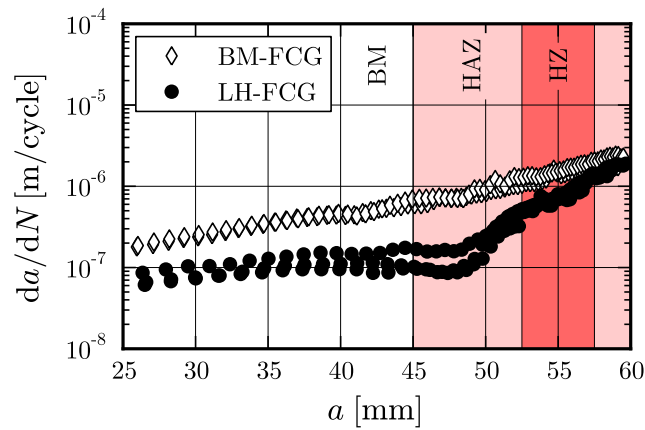
While in the HAZ and the HZ an effect of the changed microstructure on the fatigue crack growth can not be excluded, the observed crack growth retardation for  $a < 45$  mm is clearly a result of the residual stresses alone. In this area the measured residual stress differences  $\Delta\sigma$  indicate the presence of compressive longitudinal residual stresses  $\sigma_{yy}$ . Since these compressive residual stresses act parallel to the applied load  $F$ , the combination of the applied load and the residual stresses leads to a

Table 3.4: Measured specimen thickness and maximum crack deviation.

Specimen	Thickness [mm]	Crack Deviation [ $^\circ$ ]
BM-FCG-2	5.07	11.3
BM-FCG-3	5.07	3.1
LH-FCG-2	5.07	11.4
LH-FCG-3	5.07	7.3
LH-FCG-11	5.07	3.5



(a)



(b)

Figure 3.15: (a) Measured crack length  $a$  as function of the loading cycles  $N$  and (b) calculated fatigue crack growth rate  $da/dN$  as function of the crack length  $a$ . Shown are the results for two base material specimens (BM-FCG) and three laser heated specimens (LH-FCG) tested in T-L orientation. For clarity, only every 5th point of the measurement data is shown.

reduction of the total stress intensity factor  $K_{tot}$ .

### 3.10 Fractographic examination

After the fatigue test, a fractographic examination was performed for the laser heated specimens LH-FCG-3. The right side of Fig. 3.16 shows a macro overview picture of the examined crack face indicating the locations for the pictures with increasing magnifications. For the higher magnification pictures in the two left columns, a JEOL JSM-6490LV SEM using a acceleration voltage of 25 kV at a working distance of 20 mm was used.

In general, the examined crack face shows the characteristic features of a trans-crystalline fatigue crack in aluminium which are fatigue fracture paths, fatigue striations and fatigue lines.

However, for the positions  $x = 35$  mm,  $x = 40$  mm and  $x = 45$  mm particularly in the surface near areas of the crack face signs of local plastic deformation are found what indicates a contact of the crack faces during the cyclic loading. This is very pronounced for the areas marked in Fig. 3.16.

A visible change can be seen for the position  $x = 50$  mm. Here, no further signs of local plastic deformation can be found on the crack face. Instead, fatigue fracture paths with steps and sporadic split fatigue lines are found. For  $x = 55$  mm again no signs of plastic deformation due to crack face contact can be found. However, the spacing of the fatigue fracture paths and an number of split fatigue lines is increasing. Additionally, insular areas of shear fracture can be found. This indicates a rapid increase of the acting stress intensity factor range.

### 3.11 Discussion - Proof of concept

As indicated by the microscopical examinations, a small effect of the laser heating on the grain structure was found. The formation of small grains in the HZ indicates a thermally activated partial recrystallisation in this area. However, no signs of partial melting or surface crack formation were found.

The micro hardness measurement and tensile test results indicate a clear change of the mechanical properties in the area of the HAZ and the HZ. The thermocouple measurements showed that in the HAZ and the HZ peak temperatures of  $225^{\circ}\text{C} < T_{max} < 380^{\circ}\text{C}$  have been reached. This suggests that the excessive heating in HAZ and HZ changed the precipitation state substantially, explaining the measured drop of hardness and yield stress.

As expected, the obtained residual stress distribution after laser heating was found to be very similar to the one found after welding, with high tensile longitudinal

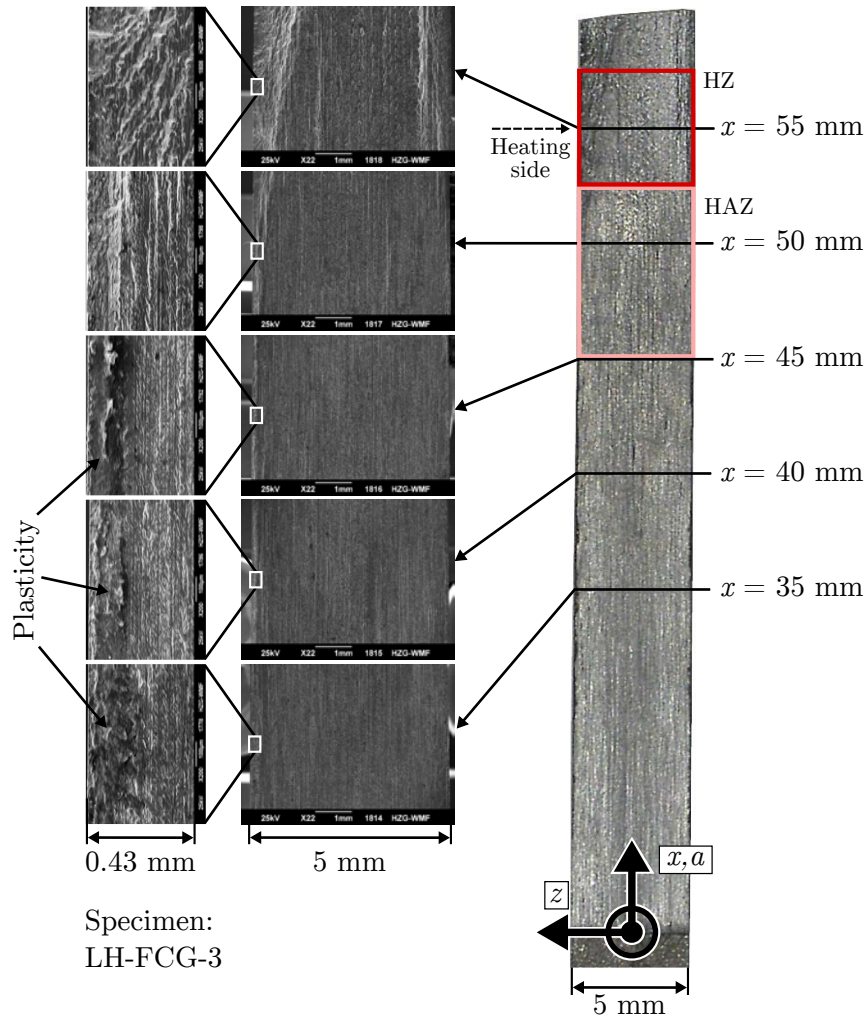


Figure 3.16: Fractographic examination of the laser heated specimen LH-FCG-3 after the fatigue testing.

residual stresses in the HZ which are balanced by compressive longitudinal residual stresses in the surrounding areas.

While in the HAZ and the HZ an effect of the changed microstructure on the fatigue crack growth can not be excluded, the observed crack growth retardation for  $a < 45$  mm, what corresponds to the area with base material properties, is clearly a result of the residual stresses alone. In this area the measured residual stress differences  $\Delta\sigma$  indicate the presence of compressive longitudinal residual stresses  $\sigma_{yy}$ . Since these compressive residual stresses act parallel to the external applied load  $F$ , their main effect is a reduction of the total stress intensity factor  $K_{tot}$  at the crack tip, resulting from the combination of the applied load and the residual stresses.

As a consequence, there are two major effects of the residual stresses on the crack growth:

1. If the crack faces stay completely open during the cyclic loading under combined loading with external load and residual stresses, the residual stresses influence  $K_{tot}$  under minimum and maximum load in the same way. Accordingly, their only impact is a shift of the stress intensity ratio. For compressive residual stresses  $R_{appl} > R_{tot}$  and for tensile residual stresses  $R_{appl} < R_{tot}$ . Since the crack growth rate is rather insensitive to the stress ratio, this leads only to a small effects compared to the stress free state.
2. In the presence of large compressive residual stresses, it is possible that the crack faces close completely even for loads larger than the minimum applied load. In this case  $K_{tot}(F_{max}) < K_{appl}(F_{max})$  and due to the closed crack faces  $K_{tot}(F_{min}) = 0$ . Hence, the total stress intensity factor range  $\Delta K_{tot}$  is reduced and the total stress intensity factor ratio  $R_{tot} = 0$ . Since the crack growth rate is very sensitive to the stress intensity factor range, this can create a huge retardation effect.

Based on the fractographic examination, the measured crack growth in the laser heated specimens can be explained in the following way. While the crack was growing through the areas of compressive residual stresses, the crack faces touched each other during the cyclic loading as indicated by the deformed areas on the examined crack face. This was leading to a reduction of  $\Delta K_{tot}$  and accordingly a large retardation effect. However, after the crack tip entered the area of tensile residual stresses, the retardation effect vanished since the tensile residual stresses increase  $K_{tot}(F_{min})$  and  $K_{tot}(F_{max})$ , what promoted a complete opening of the crack faces during the cyclic loading. Thus, no more deformed areas on the crack faces were found.

In the transition region from compressive to tensile residual stresses the crack opening behaviour is more complex. A comprehensive presentation of the underlying mechanisms was published for example by Schnubel et al. in [7], where the prediction

of crack growth rates for a crack growing through a residual stress field similar to the one shown in Fig. 3.12 was discussed.

In summary, the presented results deliver the desired experimental proof of concept – It is possible to effectively retard the fatigue crack growth in aluminium C(T)100 specimens via laser heating. The lifetime of the laser heated specimens was increased to approximately 200%-300% of the one of the tested base material specimens and the observed fatigue crack growth retardation is clearly dominated by the induced residual stresses.



## 4 FCG prediction methodology

As seen in the previous chapter, a retardation of the fatigue crack growth due to laser heating is not found in the heating area, where the tensile stresses are induced, but in the surrounding areas with balancing compressive residual stresses. Hence, the correct positioning of the heating area is the key parameter to improve the fatigue performance. Therefore, this chapter is dedicated to the development of a quantitative numerical prediction methodology for the fatigue crack growth in laser heated specimens that can be used for design optimisation studies.

One very favourable way for reaching this goal is the combination of numerical process simulation and fracture mechanics analysis. While the fundamentals of the used numerical methods were discussed already in section 2, in this chapter more specific information on the global prediction approach and the specific implementation for the laser heating process shall be given.

### 4.1 Commonly used methodology

As already mentioned in the introduction chapter, the brisk interest in the last years to address the effects of residual stresses in the prediction methods used for damage tolerance evaluation of aircraft structures [3–5] is related to the growing interest in the aircraft industry to use advanced manufacturing technologies like laser beam welding or friction stir welding for the production of metallic integral airframe structures [84, 85]. These processes inevitably induce significant amounts of residual stresses [11, 15, 16, 38].

The underlying scientific topic, the prediction of the fatigue crack growth in structures and components containing residual stresses is a classical fracture mechanics problem and during the last decades, the methodology consisting of the following steps has found common acceptance [3, 5, 49, 86–95]:

- Measurement of the component of the residual stresses that acts perpendicular to the crack growth direction.
- Extraction of the residual stress intensity factor  $K_{\text{res}}$  due to the internal residual stresses using for example the finite element method (FEM) or the weight function method (WFM).

- Calculation of the total stress intensity  $K_{\text{tot}} = K_{\text{res}} + K_{\text{appl}}$  as the sum of  $K_{\text{res}}$  and the applied stress intensity  $K_{\text{appl}}$  using the superposition law.
- Calculation of the fatigue crack growth rate  $da/dN$  by using  $K_{\text{tot}}$  in an empirical crack growth law, such as the Walker equation.

An aspect that has been addressed by some researchers in the past [4, 89] is the potential influence of the redistribution of the residual stresses due to the crack growth on the predictions. By the use of the FEM for the calculation of  $K_{\text{res}}$  such redistribution effects are included naturally in the simulations.

## 4.2 Limitations of the commonly used methodology

In general, this approach shows good results. However, with regard to the presented laser heating of C(T)100 specimens there are two major limitations that need to be addressed:

- For cracks growing through compressive residual stress fields, nonlinear contact corrections are needed to ensure a physical sound description of the experimental conditions in the predictions [86]. Hence, the superposition law is not valid any more. The underlying effects and their impact on the predicted fatigue crack growth rates have been discussed by Schnubel et al. detailed in [7].
- Residual stress measurements are costly, difficult to perform and they normally only deliver specific components of the stress tensor. This issue becomes even more critical when thinking on large and/or complex shaped structures or components as they are commonly found in an aircraft. Additionally, the gained results are only representative for the specific case that has been examined. This causes the need to perform a large number of measurements, if for example a design parameters like the heating line position shall be examined.

## 4.3 Extended prediction methodology

Motivated by these points and adopting the idea presented by Jang et al. [30] to use numerical predictions of heating induced residual stresses as basis for the following fracture mechanics analysis, the extended methodology shown in Fig. 4.1 was developed, consisting of the following steps:

1. Use of a thermal FE analysis to predict the transient heating temperature field.
2. Use of a mechanical FE analysis incorporating the thermal expansions and temperature dependent plasticity to predict the full residual stress field after heating.



This way, it becomes possible to validate the prediction methodology for a specific case on an experimental basis and then use the validated model afterwards for the numerically based design optimisation, before cost- and time consuming experimental studies are started.

Only little literature is available describing such coupling of the numerical methods as proposed. One work pointing into the same direction was published very recently [96]. Here, also structural process simulation was coupled with following mechanical simulations for the calculation of  $K_{\text{res}}$  in a steel butt-weld. However, the resulting crack growth rates were only predicted for one crack length under different applied loads, the crack tip was situated in an area of tensile residual stresses and the predicted crack growth rates were not validated experimentally.

In another work [97] residual stresses after the welding of thick steel sections were predicted via three dimensional structural welding simulation. Afterwards, the results were used for linear elastic fracture mechanics simulations of the through thickness crack growth at the weld root.

As already stated in section 2.10, the study presented by Jang et al. [30] provided major input for the development of the proposed extended prediction methodology, since it described a strategy to predict the observed fatigue crack growth retardation due to heating induced residual stresses on basis of numerical process simulation results. However, the crack closure based fracture mechanics analysis used by Jang et al. [30] does not describe the complex opening behaviour of the crack faces in the residual stress field physically sound. Therefore, the achieved prediction results only showed a qualitative agreement with the measurement results.

### 4.4 Implementation of the extended prediction methodology

The implementation of this approach was realised using the programming language Python for embedding two commercial FE codes – Sysweld for the heating process simulation and Abaqus for the numerical fracture mechanics analysis – as shown in Fig. 4.2. Since the developed methodology shall be used for design optimisation studies, including parametric changes of different design parameters, one challenge during the implementation of the proposed approach was to provide a full automatization of the job execution and result extraction. This was realised via a master Python routine that managed the event-driven triggering of all calculation and extraction steps as a further development of an approach presented in [98].

Before the starting of the calculations, some input data needs to be specified as seen in the left column of Fig. 4.2. In detail, these are the boundary conditions, the material properties and the mesh definition for both the Sysweld process simulation and the Abaqus fracture mechanics analysis. In addition, for the Abaqus fracture

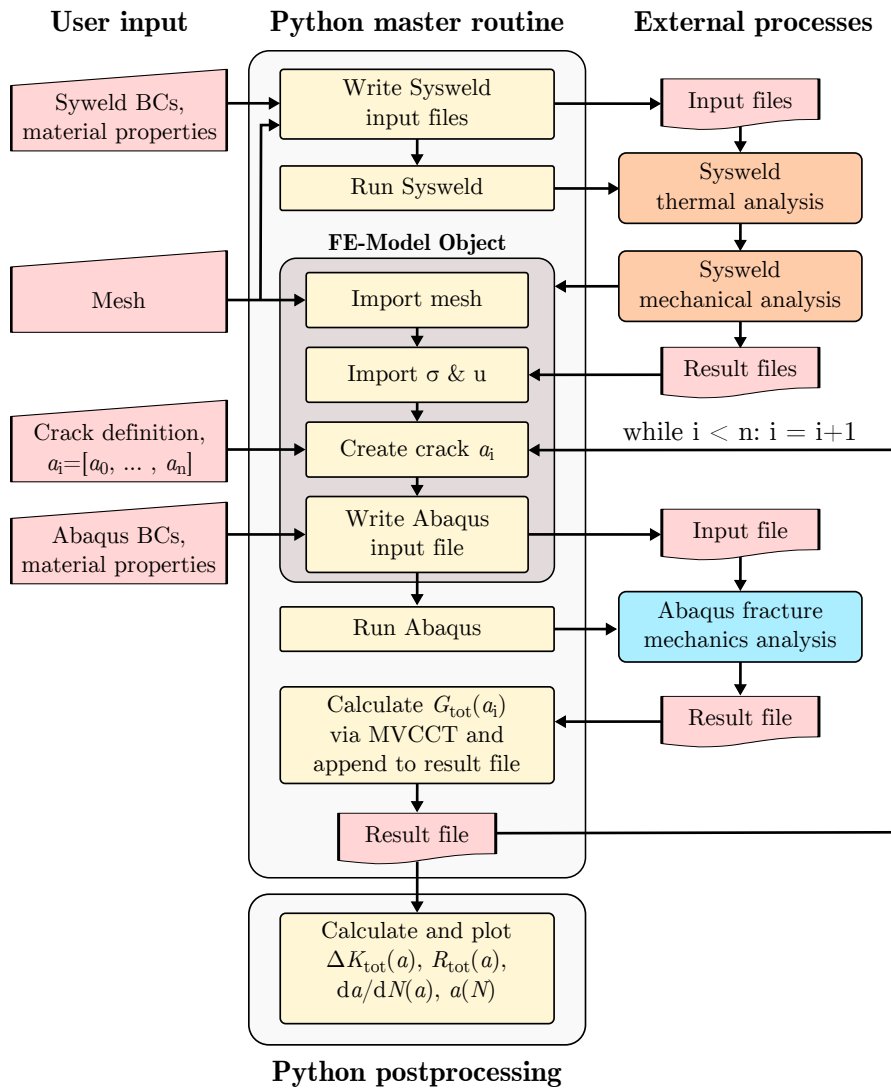


Figure 4.2: Implementation of the developed approach using the programming language Python to couple the two commercial FE codes Sysweld and Abaqus.

mechanics analysis also the applied loads, the crack plane, the crack growth direction and the specific crack lengths  $a_i$  for which calculations shall be performed must be defined.

Based on the data provided, the Python master routine first generates the Sysweld input files needed for the computations, then starts the Sysweld simulation and waits for the running Sysweld job to finish.

Triggered by the termination of the Sysweld job, an object of the programmed Python class FE-Model is initialised. Then, the complete mesh definition, the calculated distortions  $u$  and the residual stresses  $\sigma$  are imported. The FE-Model object provides a method to generate an artificial crack by doubling the nodes and relabelling the corresponding element definitions internally. This routine is then used to generate an artificial crack of the defined length  $a_i$ . Based on this definitions, an Abaqus input file is written including the artificial crack, the contact definitions on the crack faces and the applied loads.

As next step, the execution of the Abaqus simulation is triggered by the Python master routine. After the Abaqus simulation finishes, the master routine extracts the needed results for the following calculations via the MVCCT approach and calculates the total energy release rate  $G_{\text{tot}}(a_i)$  for all applied loads and appends them to an internal result file. Then, it checks if a further Abaqus simulation with a different crack length  $a_{i+1}$  needs to be performed. If so, the subroutine of the FE-Model object for introducing the new crack length is called again and the new Abaqus simulation is started for  $a = a_{i+1}$ .

In a post processing step, after the termination of all Abaqus simulations ( $a = a_n$ ), the internal result file containing the calculated  $G_{\text{tot}}(a)$  is evaluated. This means that  $K_{\text{tot}}(a)$ ,  $\Delta K_{\text{tot}}(a)$  as well as  $R_{\text{tot}}(a)$  are calculated for each crack length and inserted in the Walker equation to predict  $da/dN$ . As last step,  $da/dN$  is numerically integrated for the calculation of  $a(N)$ .

# 5 Validation of the FCG prediction methodology

In this chapter the prediction methodology developed in chapter 4 will be applied to the case of a AA2198 C(T)100 specimen with a heating line at  $x_h = 55$  mm that was experimentally studied in chapter 3. The goal is to validate every step of the prediction methodology based on the comparison with the experimental results for this specific case.

## 5.1 Mesh

For the process simulation as well as for the fracture mechanics simulation the mesh shown in Fig. 5.1 is used.

The outer mesh dimensions correspond to the ones of the C(T)100 specimens used in the experimental characterisation ( $125 \text{ mm} \times 120 \text{ mm} \times 5 \text{ mm}$ ). The whole mesh, except of the elements in the vicinity of the starter notch, consists of linear brick elements with a constant edge length of 1.25 mm (approximately 38 000 linear elements). To reduce the modelling effort, the fixture holes were not modelled. However, in con-

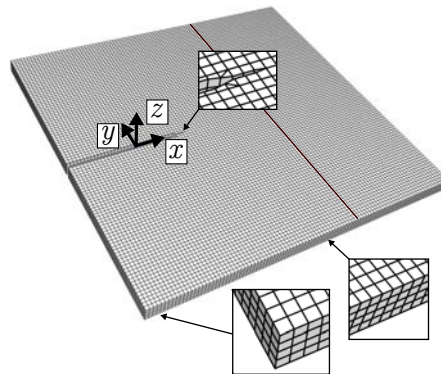


Figure 5.1: Sketch of the build FE mesh representing a C(T)100 specimen with a thickness of 5 mm, consisting of linear bricks elements with a constant edge length of 1.25 mm.

trast to a previous study [7], the geometry of the starter notch has been modelled explicitly, since the locally changed stiffness has an influence on the final residual stress state during the process simulation. The use of the identical meshes for all simulation steps allows a direct transfer of the simulation results from the process simulation to the fracture mechanics simulations.

## 5.2 Thermal FE analysis

The temperature dependent material properties used in the thermal part of the process simulation are shown in Fig. 5.2. Since no measurement data was available for AA2198-T8, most of the properties were adopted from the Sysweld material database AlSiMg. However, since the thermal conductivity  $\lambda$  has a large influence on the prediction results [99], it was taken from [8] for AA2195. AA2195 is also an aluminium-lithium alloy. Compared to AA2198, the chemical composition of AA2195 shows a similar lithium but a higher copper content.

Following the introduction given in section 2.3.1, a Goldak ellipsoid volume heat source (Eq. 2.5) was used for modelling the heat flux into the model. Since the specimens were clamped on a table during laser heating, as shown in Fig. 3.2, two separate thermal contact conditions were defined to describe the heat exchange. One for the whole upper surface of the specimen ( $z_s > -2.5$  mm) that is only in thermal contact with the surrounding air and another one for the lower surface of the specimen that is in thermal contact with the table ( $z_s = -2.5$  mm).

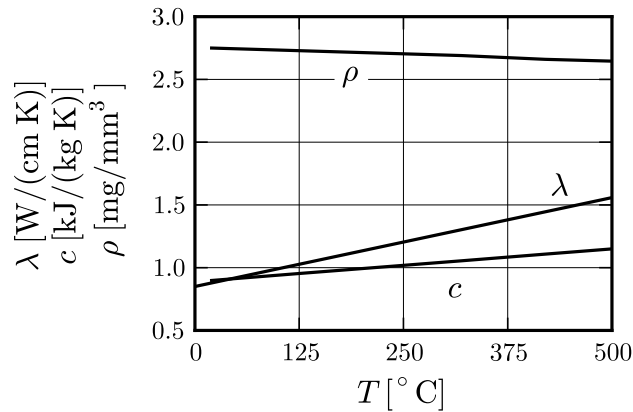


Figure 5.2: Temperature dependent material properties used for the thermal process simulation. Shown are the density  $\rho$ , the thermal conduction  $\lambda$  and the specific heat  $c$ .

Table 5.1: Calibrated thermal boundary conditions.

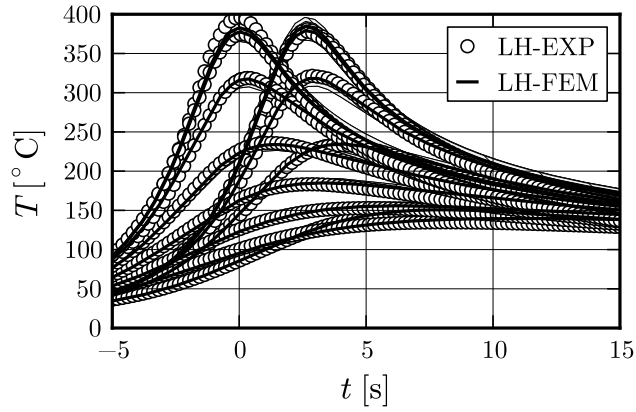
$(x_0, y_0, z_0)$	=	(55.0 mm, -60.0 mm, 2.5 mm)
$v_y$	=	3.33 mm/s
$A$	=	4.0 mm
$B$	=	4.0 mm
$C$	=	0.5 mm
$Q_0$	=	26.0 W/mm <sup>3</sup>
$h_c$	=	$\begin{cases} 75.0 \text{ W}/(\text{m}^2 \text{ K}) & , \text{ if } z_s = -2.5 \\ 25.0 \text{ W}/(\text{m}^2 \text{ K}) & , \text{ if } z_s > -2.5 \end{cases}$
$\sigma_r$	=	$5.67 \cdot 10^{-8} \text{ W}/(\text{m}^2 \text{ K}^4)$
$\epsilon_r$	=	0.8

As already explained in section 2.3.1, the first step in the thermal process simulation is the iterative calibration of this thermal boundary conditions on basis of experimental measurements. In our case, this was done on basis of the thermocouple and mirco hardness measurements presented in chapter 3. Even though for the presented study this calibration was done manually, as it is common practise, the performed calculations inspired to start working on the development of an automatised approach to handle this time consuming calibration step for future applications. The first achievements have been recently presented by Schnubel et al. [100] for the case of the thermal simulation of aluminium laser butt welding. After the calibration using the new automatised approach, a mean deviation of only 5 °C between measurement and simulation results was reached. The results of the performed manual iterative calibration of the thermal boundary conditions used for the laser heating process are given in Table 5.1. The nomenclature is in accordance to the definitions made in section 2.3.

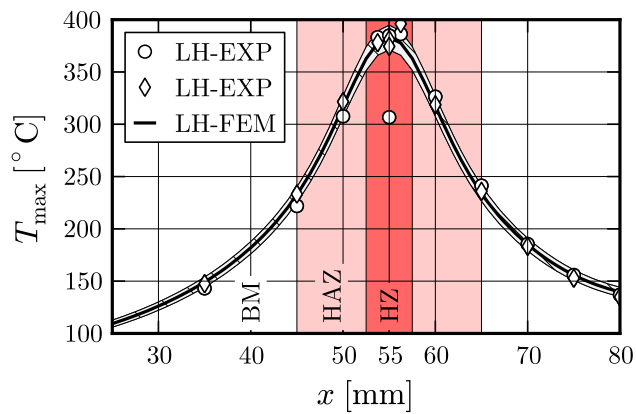
Figure 5.3a gives the comparison of the transient measured and predicted temperatures for the thermo couple positions. Figure 5.3b shows the comparison of the measured (LH-EXP) and numerically predicted (LH-FEM) peak temperatures  $T_{\max}$  during the thermo cycle as function of the  $x$ -position. As shown, an excellent agreement was achieved with the calibrated heat source amplitude  $Q_0 = 26.0 \text{ W}/\text{mm}^3$ .

To study the sensitivity of the prediction results on the value of the most important calibration parameter, which is the heat source amplitude  $Q_0$ , the variation range of the results for  $Q_0 = 26 \pm 1 \text{ W}/\text{mm}^3$  is shown as light grey hatched area in Fig. 5.3b. This variation of  $Q_0$  only leads to a moderate shift of approximately  $\pm 12 \text{ °C}$  in the predicted peak temperatures at the middle of the HZ, what is also in the range of the observed scatter of the measured peak temperatures.

The comparisons shown in Fig. 5.3 prove that the global heat input, the ther-



(a)



(b)

Figure 5.3: Comparison of the thermocouple measurements (LH-EXP) and the results of the thermal FE analysis (LH-FEM) using the calibrated heat source amplitude  $Q_0 = 26.0 \text{ W/mm}^3$ . Shown are (a) the measured and simulated transient temperatures and (b) the measured and simulated peak temperatures. The hatched light grey area indicates the variation of the results for  $Q_0 = 26 \pm 1 \text{ W/mm}^3$ .

mal conduction and the heat exchange with the environment of the experiment were matched very well by the calibrated thermal simulation. However, to gain reasonable residual stress predictions, also the very localised heat input in the heating zone needs to match the experiment. Because of that, the local heat input for welding simulations is normally calibrated on basis of the lateral extension and shape of the molten zone which can be measured directly in optical macro-graphs. Since no melting occurs during laser heating, that approach was not applicable. However, Fig. 5.4 shows an overlay of the micro hardness measurement results ( $HV$  colour plot see Fig. 3.8a) and selected isothermal contours of the numerically predicted peak temperatures  $T_{\max}$ . It is reasonable to compare those two quantities, since the drop in hardness is a direct consequence of the changes of the precipitation state due to the heating cycles [13, 41, 44–46]. The bounds of the zones with different hardness match well the predicted  $T_{\max}$  iso-contours, indicating that also the local heat input in the simulation is in good agreement with the real process using the calibrated thermal model with  $Q_0 = 26.0 \text{ W/mm}^3$ .

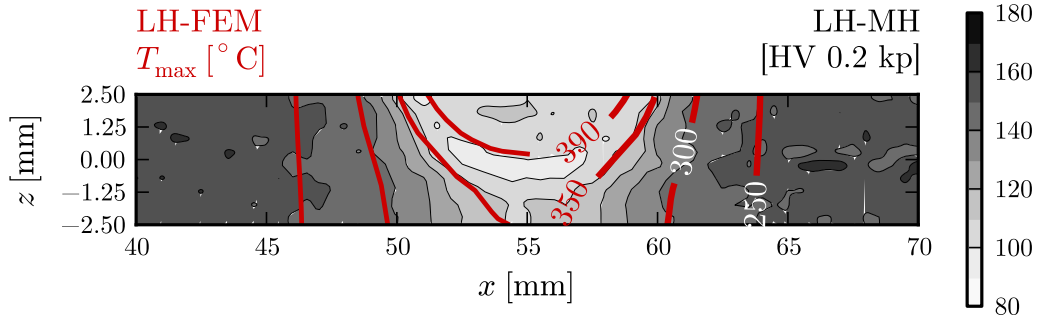


Figure 5.4: Overlay of the micro hardness measurement results (LH-MH) and the iso-contours of the numerically predicted peak temperatures  $T_{\max}$  (LH-FEM).

### 5.3 Mechanical FE analysis

The temperature dependent material properties used in the mechanical part of the process simulation are given in Fig. 5.5. Except for the yield stress  $\sigma_{ys}$ , these values were also adopted from the Sysweld material database AlSiMg. Since the temperature dependent yield stress influences the prediction results significantly [99], literature values from [13] were used of the material AA2024-T3 with a hold time at testing temperature of only 10 s. As described in section 2.3, it is crucial that the testing

condition for the measurement of the used material properties are representative for the simulated process. The data given in [13] fulfils that need and furthermore the mechanical properties of AA2024 are closer to AA2198 than the ones provided by the Sysweld material database AlSiMg. The gained simulation results clearly indicated, that plastic yielding during laser heating for the discussed case only takes place for  $T > 250$  °C. Even though the yield stress at room temperature for AA2024-T3 is significantly smaller than for AA2198-T8, the assumed yield stress for  $T > 250$  °C governs the development of the residual stresses and the room temperature values have no influence at all.

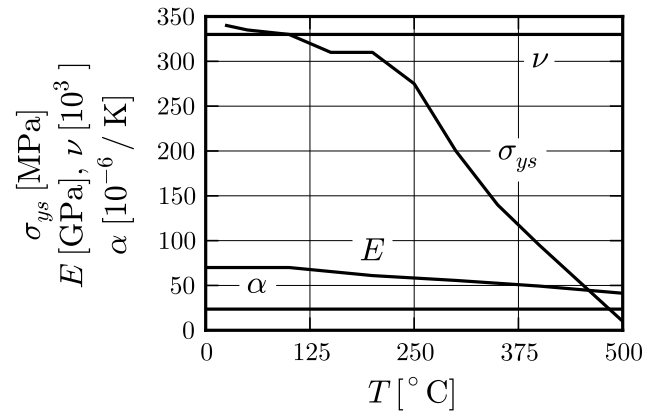
The clamping conditions during the laser heating were modelled in the mechanical analysis using elastic constraints on the nodes in the same areas as in the experiment (see Fig. 3.2) on the top and the bottom surface of the specimen. The chosen stiffness value of  $\approx 0.4$  kN/mm for each clamping position in each direction adopts results published in [101]. Furthermore, rigid body motion was prevented by applying additional rigid constraints for three nodes. To check the influence of the defined clamping conditions on the predicted residual stresses, also simulations without constraints and with rigid constraints at the clamping positions were performed. The predicted residual stresses for the simulation with the chosen elastic constraint of  $\approx 0.4$  kN/mm and the one obtained without constraints were nearly identical. The simulation with rigid constraints showed a slightly different stress distribution and some plastic yielding around the clamping areas. As stated, for the presented simulation the model with elastic constraints was used.

Figure 5.6 and Fig. 5.7 show the comparison of the measured and predicted residual stress difference  $\Delta\sigma = \sigma_{yy} - \sigma_{xx}$ . As seen in Fig. 5.6, the general pattern is the same for measurements and simulations. Looking at the calculated line scans in Fig. 5.7 it can be stated that the mechanical simulation based on the calibrated thermal model ( $Q_0 = 26$  W/mm<sup>3</sup>) delivers a reasonable prediction for the residual stresses, even though slightly higher values are predicted in the HZ compared to the measurements.

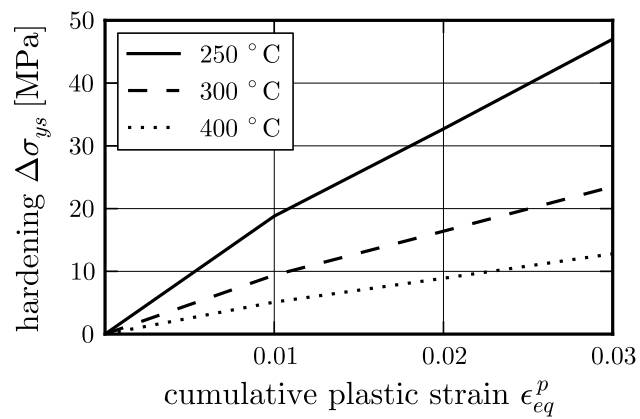
A variation of  $Q_0 = 26 \pm 1$  W/mm<sup>3</sup> leads to changes of the predicted stress differences up to 15 MPa in the HZ, while the changes in the BM areas are only in the range of 3 MPa.

In addition to the stress differences, the numerically predicted longitudinal stresses  $\sigma_{yy}$  (dotted) and transverse stresses  $\sigma_{xx}$  (dashed) are shown in Fig. 5.7. The amplitude of the transverse stresses  $\sigma_{xx}$  is rather small compared to the one of the longitudinal stresses  $\sigma_{yy}$ . Thus,  $\Delta\sigma$  is dominated by the contribution of  $\sigma_{yy}$  and both  $\Delta\sigma$  as well as  $\sigma_{yy}$  change sign from negative to positive values at  $x = 49$  mm.

Since the predicted stress differences are directly linked to the applied temperature dependent material properties and especially the yield stress  $\sigma_{ys}$ , a further improvement of the prediction quality might be achieved by using the temperature dependent  $\sigma_{ys}$  of the specimen material AA2198-T8. This should be considered for future work. Moreover, due to the large number of measurement positions needed for the prepa-

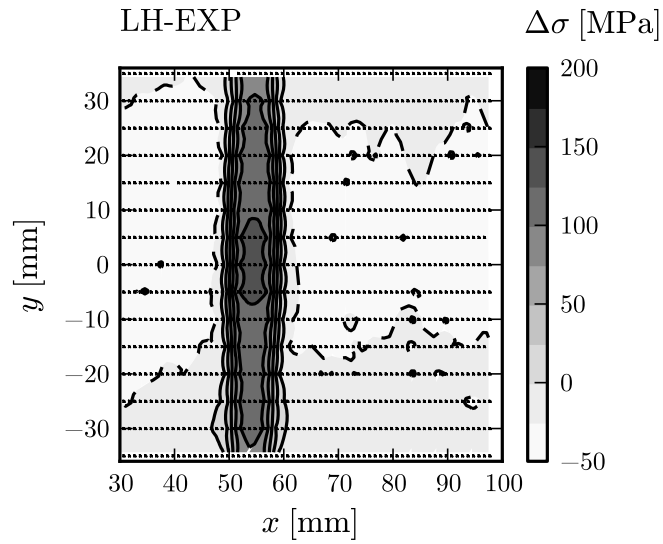


(a)

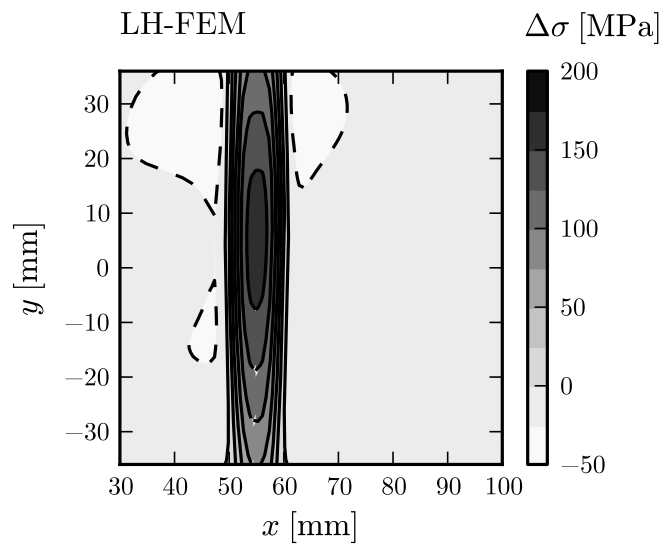


(b)

Figure 5.5: (a) Temperature dependent material properties used for the mechanical process simulation and (b) three of the look up curves used for the yield stress increase  $\Delta\sigma_{ys}$  due to the isotropic hardening. The full data set covers the temperature range  $0\text{ }^\circ\text{C} < T < 500\text{ }^\circ\text{C}$  with nine curves.



(a)



(b)

Figure 5.6: Comparison of the (a) measured and (b) predicted residual stress differences  $\Delta\sigma = \sigma_{yy} - \sigma_{xx}$ . The numerical results have been averaged through the specimen thickness to make them comparable to the measured results.

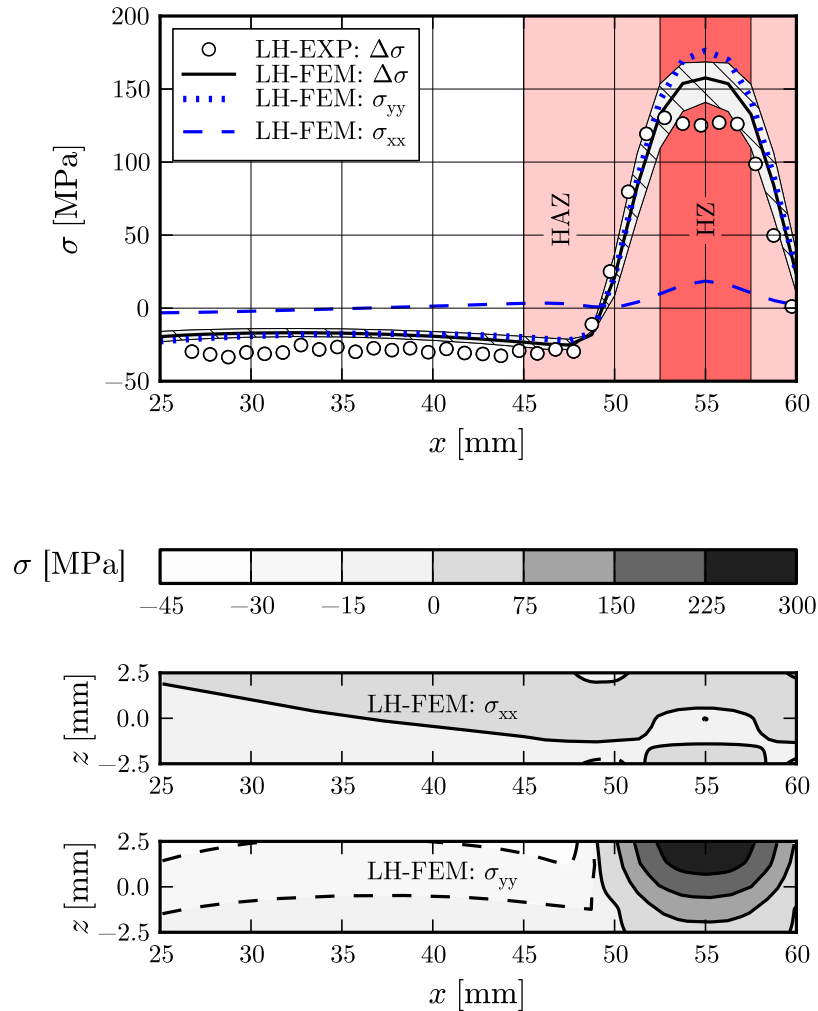


Figure 5.7: The upper graph shows line scans computed by averaging the area scan data given in Fig. 5.6 over the  $y$  coordinate for  $-12 \text{ mm} < y < 12 \text{ mm}$ . The measured  $\Delta\sigma$  are shown as open circle symbols and the predicted  $\Delta\sigma$  as solid black line. Additionally, as hatched light grey area the variation of the results is shown for an assumed uncertainty of  $Q_0 = 26 \pm 1 \text{ W/mm}^3$  and the numerical prediction results for the single stress components  $\sigma_{yy}$  (dotted) and  $\sigma_{xx}$  (dashed) are plotted. The lower two graphs show cross section plots of the predicted  $\sigma_{yy}$  and  $\sigma_{xx}$  averaged over the same region.

ration of a stress map as presented in Fig. 5.6, residual stress measurements were only performed on one specimen. Future work should also investigate the potential scatter of the measurement results by performing residual stress measurements on more specimens with a reduced number of measurement positions per specimen.

Another interesting detail arises when looking at the cross section plots of the predicted  $\sigma_{yy}$  and  $\sigma_{xx}$  (lower two contour plots of Fig. 5.7). While the predicted  $\sigma_{xx}$  shows no pronounced gradient in the  $z$ -direction, a large gradient through the thickness is predicted for  $\sigma_{yy}$ , particularly in the heating area, with maximum values in the range of 300 MPa. Future work should consider this finding, since the highly localised tensile stresses might cause localised plastic yielding under high static loads.

## 5.4 Fracture mechanics analysis

As already explained, for the fracture mechanics analysis a separate simulation was defined for each crack length  $a$ , using the deformed mesh and the full stress field from the last time step of the process simulation after cooling to room temperature. In this mechanical restart simulations pure linear elastic material behaviour with a Young's modulus  $E = 73$  GPa and a Poisson's ratio  $\nu = 0.33$  was assumed.

The applied boundary conditions are sketched in Fig. 5.8. The displacement  $u$  for the node in the mid-thickness of the specimen at the centre position of the lower fixture hole was constrained rigidly. For the corresponding node in the centre position of the upper fixture,  $u_x$  and  $u_z$  were blocked, allowing movement only in the  $y$  direction. To this single node, the external load  $F_{\text{appl}}$  was applied. To prevent rigid body motion, the displacement in the  $z$  direction was blocked for a third node lying on the symmetry plane of the specimen on the right boundary of the model.

The introduction of a crack with the desired length  $a$  was realised by cutting the model open along the specified crack path. This was done by doubling the nodes on the  $x$ - $z$ -plane at  $y = 0$ , with an  $x$ -coordinate smaller than the desired crack length  $a$  and redefining the corresponding element definitions. That allows the crack faces behind the crack tip to move independently, including opening and overlapping. To avoid a physically unreasonable overlapping, a hard contact condition was added on the created crack faces including the starter notch [7].

For each crack length the nodal displacements and forces at the crack tip were extracted and used for the calculation of  $K_{\text{tot}}(F_{\text{appl}}, a)$  via the MVCCT approach introduced in section 2.4. The results of this extraction of  $K_{\text{tot}}(F_{\text{max}} = 4.41 \text{ kN}, a)$  and  $K_{\text{tot}}(F_{\text{min}} = 0.44 \text{ kN}, a)$  based on the predicted laser heating residual stresses are shown in the upper graph of Fig. 5.9 using the open circle symbols (LH-FEM). For comparison, also the results calculated for a model without residual stresses are shown using the open diamond symbols (BM-FEM). This results from the model without residual stresses correspond to base material behaviour.

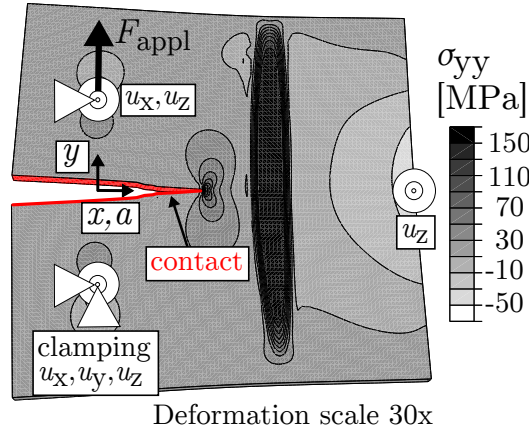


Figure 5.8: Sketch of the fracture mechanics restart simulation model with the applied boundary conditions.

For  $a < 49$  mm the crack tip is situated in the area of compressive longitudinal stresses  $\sigma_{yy}$  for the simulation including the laser heating residual stresses. Hence, the  $K_{tot}(F_{max})$  is lowered in comparison to the simulations without residual stresses. Under minimum applied load the crack faces at the crack tip stay completely closed as indicated by  $K_{tot}(F_{min}) = 0 \text{ MPa}\sqrt{\text{m}}$ . After the crack tip enters the area of tensile longitudinal residual stresses  $\sigma_{yy}$ , for  $a > 49$  mm, the values of  $K_{tot}(F_{min})$  and  $K_{tot}(F_{max})$  increase subsequently until both exceed the corresponding values from the simulations without residual stresses.

This is in agreement with the results of the fractographic examination (see Fig. 3.16) indicating a contact of the crack faces for the specific positions  $x = 35$  mm,  $x = 40$  mm and  $x = 45$  mm. At the same time, for  $x = 50$  mm and 55 mm no signs of crack face contact were found.

As shown in the lower two graphs of Fig. 5.9,  $\Delta K_{tot}$  (see Eq. 2.21) and  $R_{tot}$  (see Eq. 2.22) were calculated on basis of the extracted  $K_{tot}$ . Interestingly, the modulation of  $K_{tot}$  caused by the residual stresses, reduced  $\Delta K_{tot}$  in comparison to the simulation without residual stresses for all crack lengths.  $R_{tot}$  became zero while the crack tip was in the area of compressive  $\sigma_{yy}$  and increased to a value up to nearly 0.5 in the area of high tensile stresses  $\sigma_{yy}$  (HZ). For such a large value range of  $R_{tot}$ , the proper choice of the crack growth law in form of the Walker equation (see Eq. 2.25) is important, as shown in Fig. 3.14. Additionally, the small variation of the prediction results for an assumed uncertainty of  $Q_0 = 26 \pm 1 \text{ W/mm}^3$  is shown.

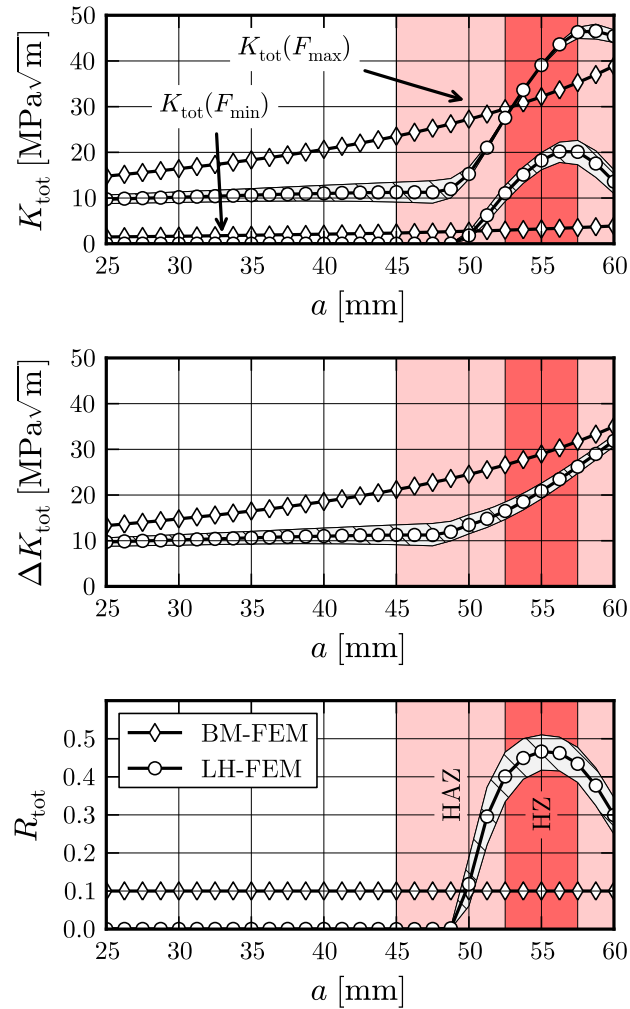


Figure 5.9: Extracted total stress intensity factor  $K_{\text{tot}}$ , total stress intensity factor range  $\Delta K_{\text{tot}}$  and total stress intensity factor ratio  $R_{\text{tot}}$ . The hatched light grey area indicates the variation of the results for an assumed uncertainty of  $Q_0 = 26 \pm 1 \text{ W/mm}^3$ .

## 5.5 Empirical crack growth law

For the prediction of  $da/dN$  the calculated  $\Delta K_{tot}$  and  $R_{tot}$  (Fig. 5.9) were used in the Walker equation (Eq. 2.25) with the fitted AA2198-T8 material constants from section 3.9. A comparison of the predicted behaviour to the measured crack growth rates from base material specimens (BM-EXP) and laser heated specimens (LH-EXP) is shown in Fig. 5.10.

The prediction results are in good agreement with the experimental data. For the base material specimens without residual stresses this shows that the calibration of the Walker equation parameters was done correctly. The agreement of the predictions and the measurement results for the laser heated specimens shows further that the developed approach is able to predict the impact of the induced residual stresses on the fatigue crack growth rate with high accuracy.

The crack length as function of the number of cycles calculated as defined in Eq. 2.26 is shown in Fig. 5.11 together with the results obtained in the experiment. Here, also a good agreement between prediction and measurement results was found.

The variation of the predictions due to the assumed calibration uncertainty of the thermal analysis of  $Q_0 = 26 \pm 1 \text{ W/mm}^3$  is for  $da/dN(a)$  and  $a(N)$  in the same range as the correspondingly observed scatter of the measurement results. This observation implies that the scatter of the measurement data can be explained by a slight variation of the process peak temperatures in the range of only  $\pm 12 \text{ }^\circ\text{C}$  or changes of the longitudinal compressive residual stresses in the range of only 3 MPa, respectively.

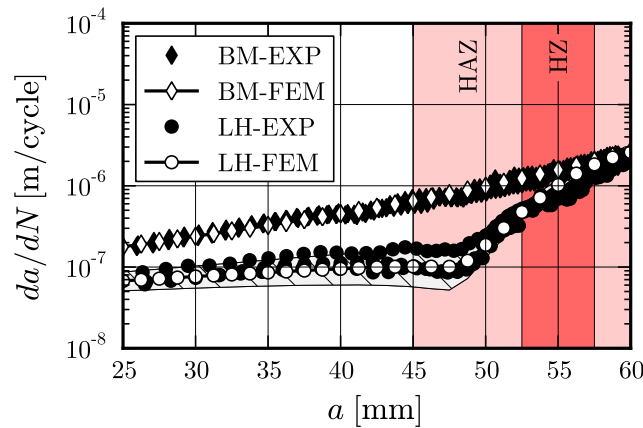


Figure 5.10: Comparison of the numerically predicted and the experimentally measured crack growth rates  $da/dN$  as function of the crack length  $a$ . The hatched light grey area indicates the variation of the prediction results for an assumed uncertainty of  $Q_0 = 26 \pm 1 \text{ W/mm}^3$ .

The observed substantial impact of small changes of the process temperatures or the residual stresses on the predicted  $a(N)$  is easy to understand since small but systematic changes of  $da/dN$  accumulate over the whole lifetime.

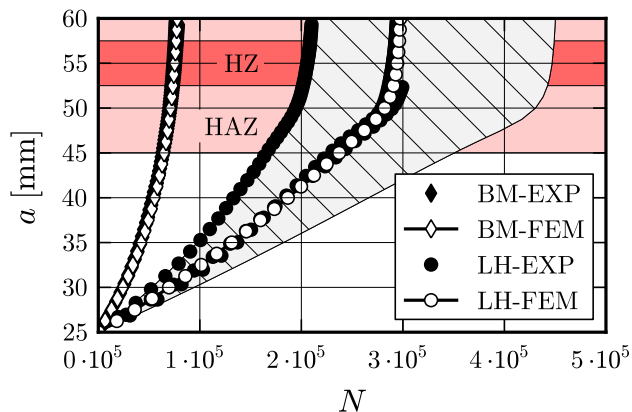


Figure 5.11: Experimentally measured and predicted crack length  $a$  as function of the loading cycles  $N$  for base material specimens and laser heated specimens. The hatched light grey area indicates the variation of the prediction results for an assumed uncertainty of  $Q_0 = 26 \pm 1 \text{ W/mm}^3$ .

## 5.6 Discussion - Validation of the FCG prediction methodology

By the direct comparison of the predictions with the measurement results for each analysis step, it was demonstrated that the developed numerical methodology works accurate.

The additional simulations with  $Q_0 = 26 \pm 1 \text{ W/mm}^3$  showed that the observed scatter of the measured fatigue crack growth data can be explained by small variations of the process peak temperatures  $T_{\max}$  in the range of only  $\pm 12 \text{ }^\circ\text{C}$ . This observation highlights that the development a proper strategy for process control must be addressed in future work.

The predicted and measured crack growth rates matched well also for those areas that showed a changed microstructure (HZ, HAZ) in the experimental examinations. Since the predictions did not account for effects of such microstructural changes on the mechanical properties, this is another indication that the observed retardation effect is attributable to the induced residual stresses alone.

Based on the obtained results, it is possible to identify the reduction of the total

stress intensity factor range  $\Delta K_{\text{tot}}$  as main retardation effect caused by a closure of the crack faces even for forces above the minimum applied load. This is consistent with the conclusions drawn at the end of chapter 3 based on the fractographic examination of the crack faces.

## 6 Design optimisation

In this chapter, the modelling approach which has been validated in the previous chapter was used to solve two simplified design optimisation problems. The objective was to find the optimum positioning of either one or two heating lines on a C(T)100 specimen that leads to a maximised total lifetime. Finally, the prediction results were validated experimentally for selected cases.

### 6.1 Positioning of one heating line

Figure 6.1 shows the principle of the first design optimisation study on the positioning of one heating line. The goal of the optimisation was to identify the heating line position  $x_{h,opt}$  leading to a maximum number of load cycles  $N$  before a crack with an initial length  $a_0 = 25$  mm reaches a final crack length of  $a = 60$  mm.

The model set-up was adopted from the validation case presented in the previous chapter, including boundary conditions and material properties. The applied loads were increased to 150% of the original values. Additionally, the heating line position  $x_h$  was varied in steps of 2.5 mm for  $25 \text{ mm} \leq x_h \leq 85 \text{ mm}$ .

Figure 6.2 shows the predicted number of cycles to reach the final crack length  $N(a = 60 \text{ mm})$  as function of the heating line position  $x_h$ . For the given design

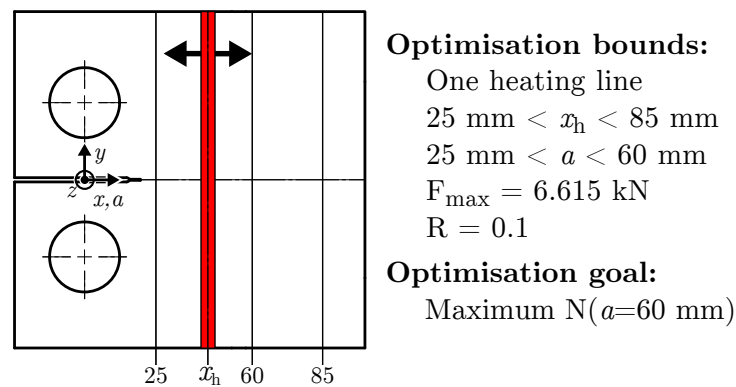


Figure 6.1: Set-up, bounds and goal of the performed optimisation study on the positioning of one heating line.

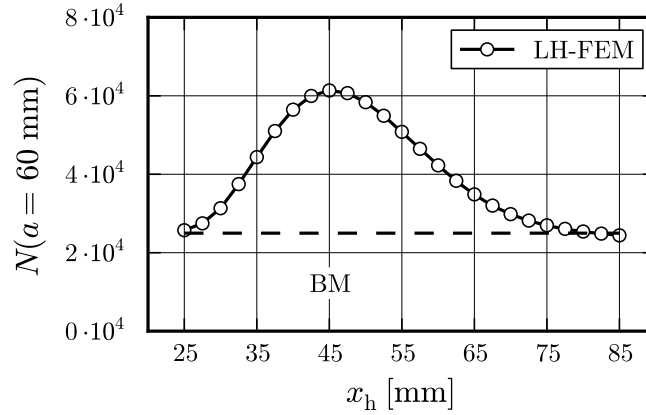


Figure 6.2: Predicted number of cycles (LH-FEM) to reach the final crack length  $N(a = 60 \text{ mm})$  as function of the heating line position  $x_h$ .

optimisation problem, the optimum line position can be identified as  $x_h = x_{h,\text{opt}} = 45 \text{ mm}$ .

The predicted fatigue crack growth behaviour was experimentally validated for the three heating line positions  $x_h = 35 \text{ mm}$ ,  $x_h = x_{h,\text{opt}} = 45 \text{ mm}$  and  $x_h = 55 \text{ mm}$ . In a first attempt to perform these tests, an initial fatigue crack of the length  $a = 24 \text{ mm}$  was introduced to the specimens prior to the application of the laser heating as described in section 3.3. However, this procedure did not prevent a formation of secondary cracks at the fixture holes during the tests, as expected, but further promoted that phenomenon. For each of the three heating line positions one specimen was tested and in each of these tests secondary cracks growing from the fixture holes were found, while the growth of the main crack was arrested.

In order to explain the observed behaviour, a further process simulation model was prepared including also a sharp initial fatigue crack. The simulation results suggested that the transient process stress fields were leading to the formation of a large plastic zone at the crack tip, i.e. a kind of overload effect. From fatigue experiments with varying amplitude loading it is well known that such formation of a plastic zone can significantly retard the fatigue crack growth [47, 52].

To avoid further problems with secondary cracking from the fixture holes, for all remaining specimens the fatigue crack introduced prior to laser heating was removed together with the formed plastic zone by extending the initial notch length from  $x = 20 \text{ mm}$  to  $x = 30 \text{ mm}$  via machining and the fatigue crack growth tests were completed.

The fatigue crack growth rates  $da/dN$  calculated on basis of the optical crack length measurement data are shown in Fig. 6.3 in comparison to the predictions. The

observed scatter of the experimental data is a result of small changes of the process conditions during the specimen manufacturing as discussed at the end of the previous chapter. The predictions match the experimental results within the experimental scatter, indicating that the chosen optimisation approach provides correct predictions.

Figure 6.3 also shows two opposing effects. On the one hand, the initial fatigue crack growth is the slower the closer the heating line position  $x_h$  is to the initial position of the crack tip ( $a_0 = 25$  mm). On the other hand, the period of slow crack growth is the shorter the closer the heating line position  $x_h$  is to the initial position of

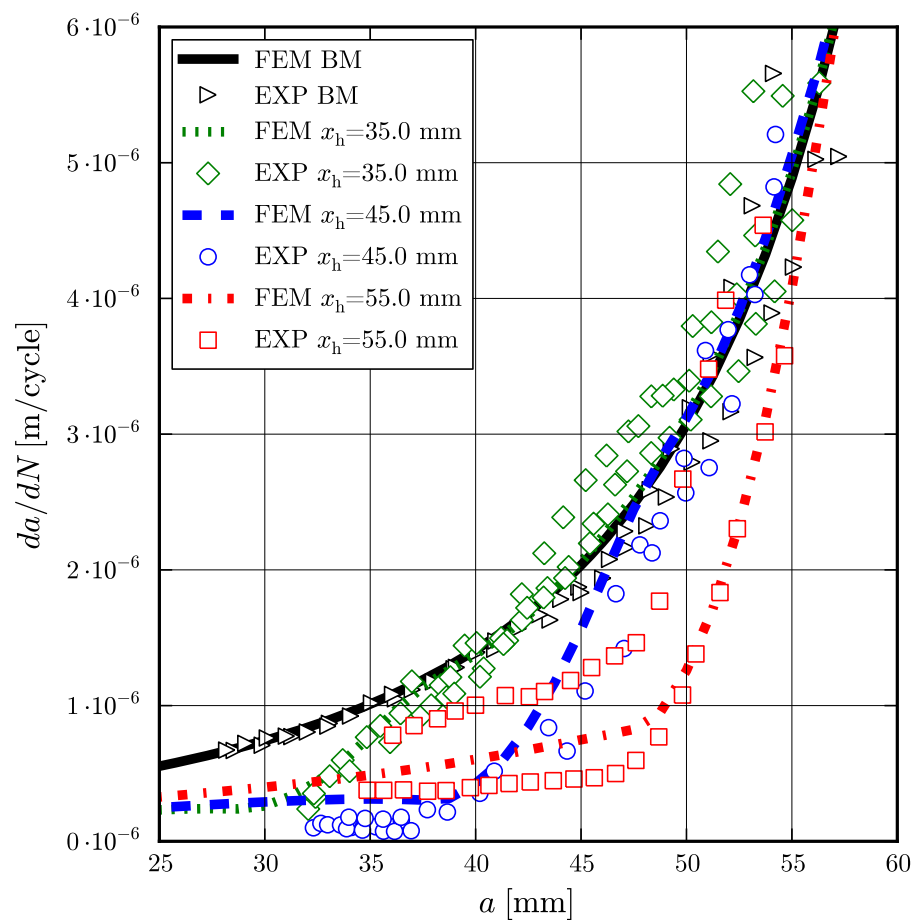


Figure 6.3: Predicted and measured fatigue crack growth rate  $da/dN$  as function of the crack length  $a$  for three selected heating line positions  $x_h$ .

the crack tip ( $a_0 = 25$  mm), since the crack growth is only retarded significantly until the crack tip reaches the corresponding heating line position at  $x_h$ . In conclusion, the identified optimum position  $x_{h,opt}$  gives the best balance between this two opposing effects for the chosen optimisation bounds.

## 6.2 Positioning of two heating lines

Figure 6.4 shows the principle of the second design optimisation study on the positioning of two heating lines. In the process simulations the application of two heating lines was executed by running a first analysis creating a heating line at  $x_{h1}$  that was followed by a second restart simulation creating a heating line at  $x_{h2}$  while using the simulation results of the first run as initial values. The remaining model parameters for the process simulation like the clamping conditions or the material properties remained unchanged.

As seen from the micro hardness measurements presented earlier in Fig. 3.8, laser heating leads to a change of the local mechanical properties in the HZ and the HAZ. By implication, this includes also the temperature dependent yield stress  $\sigma_{ys}(T)$ . On the one hand, the heating induced residual stresses are highly dependent on  $\sigma_{ys}(T)$  in the heating area as discussed in section 2.2. On the other hand, the process simulation does not capture the local changes of  $\sigma_{ys}(T)$  after the application of a first heating line. Hence, for cases in which the second heating line is placed on top of the first one, the process simulation does not deliver correct predictions for the final residual stress state. For this reason the optimisation bounds shown in Fig. 6.4 specifically exclude the designs with  $x_{h1} = x_{h2}$ .

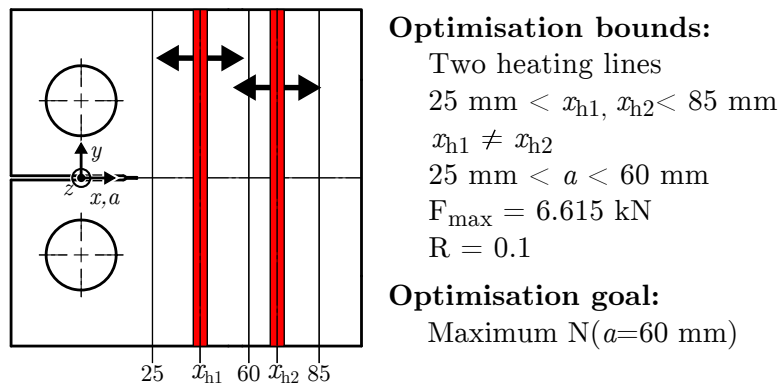


Figure 6.4: Set-up, bounds and goal of the performed optimisation study on the positioning of two heating lines.

The remaining optimisation bounds are chosen similar as for the previous example with only one heating line. The positions of the two heating lines were allowed to change independently within the interval  $25 \text{ mm} < x_{h1}, x_{h2} < 85 \text{ mm}$  and the crack growth for  $25 \text{ mm} < a < 60 \text{ mm}$  was considered. The optimisation goal was the identification of the optimum heating line position combination  $x_{h1,opt}$  and  $x_{h2,opt}$  resulting in a maximum number of cycles  $N$  until reaching the final crack length  $a = 60 \text{ mm}$ .

Due to the increased number of possible combinations of  $x_{h1}$  and  $x_{h2}$  compared to the positioning of only one line, a coarser grid for the discretely simulated combinations with a step width of 10 mm was chosen. Excluding the combinations with  $x_{h1} = x_{h2}$  leaves a total of 42 simulation runs to calculate all allowed combinations of the heating line positions using the given grid step width in the given bounds.

Figure 6.5 shows the predicted  $N(a = 60 \text{ mm})$  as function of  $x_{h1}$  and  $x_{h2}$ . The contour plot was generated using the natural neighbour interpolation on basis of the 42 specifically simulated positioning combinations. The parameter region excluded from the predictions, with  $x_{h1} = x_{h2}$ , is marked red and hatched. The results are not exactly symmetric with regard of the sequence of the line positioning. For example, the predicted  $N(a = 60 \text{ mm})$  for  $x_{h1} = 55 \text{ mm}, x_{h2} = 45 \text{ mm}$  is larger than for  $x_{h1} = 45 \text{ mm}, x_{h2} = 55 \text{ mm}$ . The optimum configuration can be identified as the combination  $x_{h1,opt} = 55 \text{ mm}$  and  $x_{h2,opt} = 45 \text{ mm}$ .

In Fig. 6.6 a comparison of the predicted  $N(a = 60 \text{ mm})$  is given for the base material, the configuration containing only one heating line at  $x_h = x_{h1,opt} = 55 \text{ mm}$  and the identified optimum configuration for two heating lines ( $x_{h1,opt} = 55 \text{ mm}, x_{h2,opt} = 45 \text{ mm}$ ). By applying one heating line at  $x_h = x_{h1,opt} = 55 \text{ mm}$ , the total predicted lifetime is increased by approximately 100% compared to the base material behaviour. The addition of a second heating line at  $x_{h2,opt} = 45 \text{ mm}$  leads to an increase of the predicted total lifetime of approximately 900% compared to the base material behaviour.

For the identified optimum configuration, with  $x_{h1,opt} = 55 \text{ mm}$  and  $x_{h2,opt} = 45 \text{ mm}$ , the predictions have been validated experimentally. The specimens for these tests were prepared along with the ones used in the previous section for the validation experiments with only one heating line. A fatigue crack of  $a = 24 \text{ mm}$  was induced prior to the laser heating. Then, the first laser heating line was applied at  $x_{h1,opt} = 55 \text{ mm}$ . After the specimens cooled down to room temperature, the silicon carbide powder from the first run was removed and the specimen surface was manually cleaned prior to the application of the second heating line at  $x_{h2,opt} = 45 \text{ mm}$ . The clamping of the specimens was removed after the application of the second heating line and the following cooling to room temperature. For this set of specimens the initial notch was also extended from  $x = 20 \text{ mm}$  to  $x = 30 \text{ mm}$  after the laser heating to remove the initial fatigue crack and the process induced plastic zone in front of the crack tip. Then, testing was performed using the same conditions as described in the previous

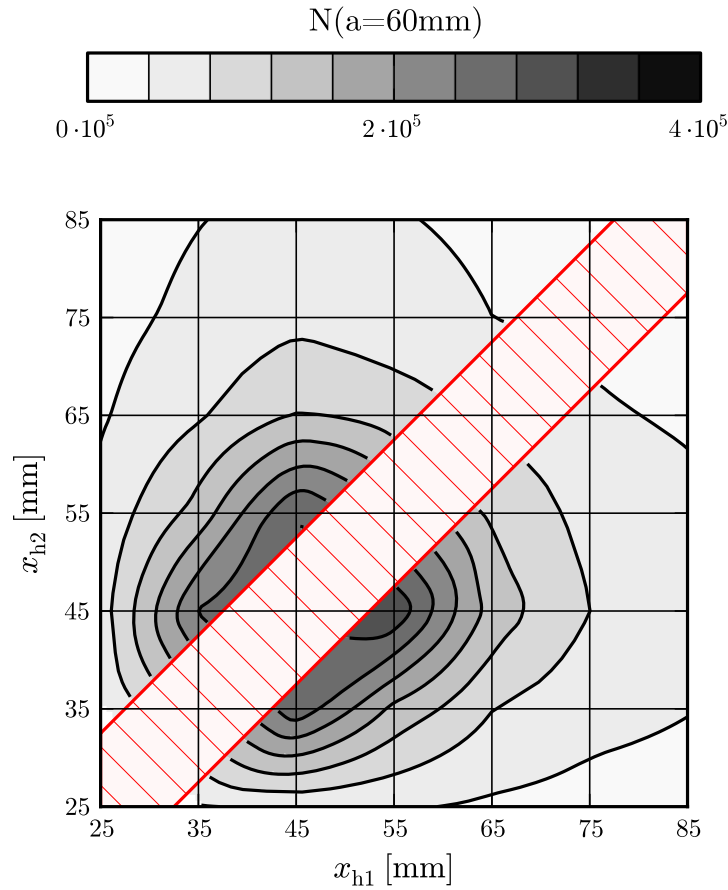


Figure 6.5: Predicted number of cycles until reaching the final crack length  $N(a = 60 \text{ mm})$  as function of the heating line positions  $x_{h1}$  and  $x_{h2}$ . The intersection points of the grid give the discrete combinations of heating line positions for which simulations were performed. The contours were calculated using the natural neighbour interpolation. The red hatched parameter area was excluded from the simulations, since there underlying assumptions of the process simulation are violated.

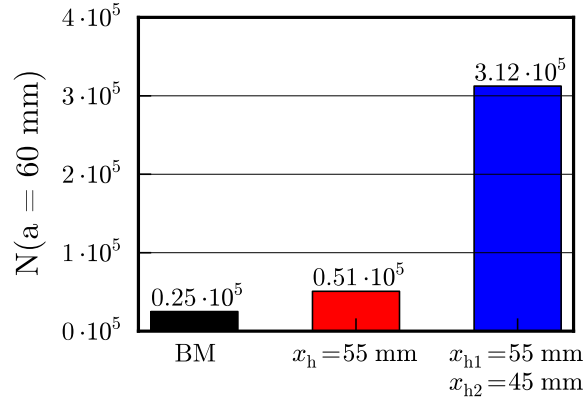


Figure 6.6: Bar plot of the predicted number of cycles until reaching the final crack length  $N(a = 60 \text{ mm})$  for the cases base material without heating line (BM), one heating line at  $x_h = 55 \text{ mm}$  and two heating lines at  $x_{h1,\text{opt}} = 55 \text{ mm}$ ,  $x_{h2,\text{opt}} = 45 \text{ mm}$ .

section.

Figure 6.7 shows the predicted fatigue crack growth rate for the optimum configuration, with  $x_{h1,\text{opt}} = 55 \text{ mm}$  and  $x_{h2,\text{opt}} = 45 \text{ mm}$ , together with the experimental results based on the optical crack length measurement data. The predictions match the experimental results within the experimental scatter, indicating that the chosen optimisation approach provides correct predictions also for this case.

For comparison, in Fig. 6.7 also the results for the base material and the configuration containing only one heating line at  $x_h = x_{h1,\text{opt}} = 55 \text{ mm}$  are shown. The addition of the second heating line at  $x_{h2,\text{opt}} = 45 \text{ mm}$  leads to a drop of the initial crack growth rate compared to the configuration with only one heating line at  $x_h = x_{h1,\text{opt}} = 55 \text{ mm}$ . However, after reaching the position  $x_{h2,\text{opt}} = 45 \text{ mm}$  the crack growth rate does not directly increase as it is the case for the specimens containing only one heating line at this position (see Fig. 6.3,  $x_h = 45 \text{ mm}$ ). Instead, the crack growth is further retarded and shows a similar behaviour as the specimen containing only one heating line at  $x_h = x_{h1,\text{opt}} = 55 \text{ mm}$ . In conclusion, this means that the significantly increased total lifetime  $N(a = 60 \text{ mm})$  for the optimum configuration, i.e.  $x_{h1,\text{opt}} = 55 \text{ mm}$  and  $x_{h2,\text{opt}} = 45 \text{ mm}$ , is a result of a decrease of the initial crack growth rate in addition to a longer preservation of the retardation effect in comparison to the designs containing only one heating line.

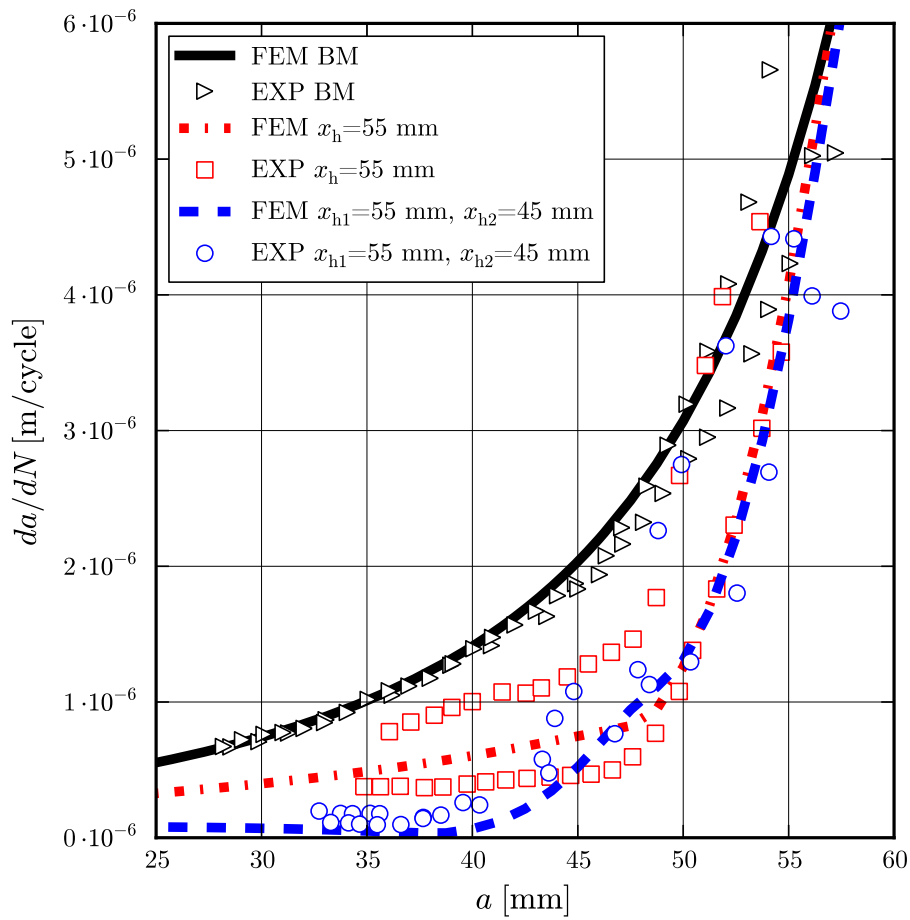


Figure 6.7: Predicted and measured fatigue crack growth rate for the cases base material without heating line (BM), one heating line at  $x_h = 55$  mm and two heating lines at  $x_{h1,opt} = 55$  mm,  $x_{h2,opt} = 45$  mm.



## 7 Conclusions

It was experimentally demonstrated that it is possible to significantly retard the fatigue crack growth via laser heating. Experiments were carried out on C(T)100 specimens made from the new aircraft aluminium-lithium alloys AA2198 in the peak aged T8 temper. The main scope of the experimental study was the measurement of the process temperature field, the induced residual stresses and the resulting impact on the fatigue crack growth.

Despite the observed heating induced modification of the precipitation state and the connected change of the mechanical properties, the fatigue crack growth experiments showed a significant retardation of the crack growth in the laser heated specimens in comparison to base material specimens. These results demonstrate the eligibility of laser heating as life enhancement method for aircraft applications. However, since damage tolerant design has to address fatigue crack growth and residual strength at the same time, one focus of future work should be to clarify the impact of laser heating on the residual strength of components and structures.

The experimental proof of concept was followed by the development of an extended prediction methodology, combining numerical process simulation for the prediction of the heating induced residual stresses with numerical fracture mechanics simulations to predict the fatigue crack growth. In contrast to the commonly used methodology, the developed approach delivers correct predictions for cracks growing through compressive residual stress fields and, in addition, it is possible to virtually study the impact of the variation of design parameters like the heating line position or the specimen geometry without a need for further experiments.

After its implementation, the developed prediction methodology was validated by comparing the numerical analysis results for each step with the corresponding experimental results. It was demonstrated that the developed approach is capable to deliver accurate predictions of the fatigue crack growth. The simulations with slightly changed heat inputs highlighted, that even small variations of the process conditions can have a substantial impact on the fatigue crack growth in laser heated specimens. This observation gives a reasonable explanation for the observed scatter of the measured fatigue crack growth data and highlights the need for improved process control in order to further decrease that scatter.

Finally, the developed prediction methodology was used to solve two design optimisation problems, i.e. the positioning of either one or two heating lines on a C(T)100 specimen. To validate the general applicability of this strategy, a final set of specimens

was manufactured and tested for selected cases. For all tested cases the predictions matched the experimental results within the experimental scatter.

The presented study demonstrated the potential of the developed numerical approach to optimise the fatigue crack growth life of specimens containing laser heating lines on the laboratory scale. Hence, the next challenge for future work is to scale up this approach to larger component-like specimens and, finally, to real aircraft components. The presented work provides a good starting point for this up-scaling. However, the expected increase of FE model size and the corresponding calculation times in particular for the transient process simulation might necessitate the development and implementation of simplified approaches for the prediction of the heating induced residual stresses. Moreover, the fracture mechanics analysis used in the presented prediction methodology should be extended to capture effects attributable to the complex loading conditions for real components such as deviations of the crack path.

# Bibliography

- [1] McClung RC. A literature survey on the stability and significance of residual stresses during fatigue. *Fatigue & Fracture of Engineering Materials & Structures* 2007;30(3):173–205. doi:10.1111/j.1460-2695.2007.01102.x.
- [2] Ball D. The influence of residual stress on the design of aircraft primary structure. *Journal of ASTM International* 2009;5(4):216–239. doi:10.1520/JAI101612.
- [3] Zhang X, Irving P, Edwards L, Fitzpatrick M, Sinclair I, Lin J, et al. The influence of residual stress on design and damage tolerance of welded aircraft structures. In: Dalle Donne C, editor. *Proceedings of the 23rd ICAF Symposium of the International Committee on Aeronautical Fatigue*; vol. 1. 2005, p. 265–281.
- [4] Edwards L, Fitzpatrick ME, Irving PE, Sinclair I, Zhang X, Yapp D. An integrated approach to the determination and consequences of residual stress on the fatigue performance of welded aircraft structures. *Journal of ASTM International* 2006;3(2):1–17. Paper ID JAI12547.
- [5] Irving P, Ma YE, Zhang X, Servetti G, Williams S, Moore G, et al. Control of crack growth rates and crack trajectories for enhanced fail safety and damage tolerance in welded structures. In: Bos M, editor. *Proceeding of the 25th ICAF Symposium of the International Committee on Aeronautical Fatigue*. 2009, p. 387–405.
- [6] Richter-Trummer V, Tavares S, Moreira P, de Figueiredo M, de Castro P. Residual stress measurement using the contour and the sectioning methods in a MIG weld : Effects on the stress intensity factor. *Ciência e Tecnologia dos Materiais* 2008;20:115–119.
- [7] Schnubel D, Huber N. The influence of crack face contact on the prediction of fatigue crack propagation in residual stress fields. *Engineering Fracture Mechanics* 2012;84(0):15–24. doi:10.1016/j.engfracmech.2011.12.008.
- [8] Chao YJ, Qi X, Tang W. Heat transfer in friction stir welding - Experimental and numerical studies. *Journal of Manufacturing Science and Engineering* 2003;125(1):138–145. doi:10.1115/1.1537741.

- [9] Richards D, Prangnell P, Williams S, Withers PJ. Global mechanical tensioning for the management of residual stresses in welds. *Materials Science and Engineering A* 2008;489:351–362.
- [10] Yan DY, Wu AP, Silvanus J, Shi QY. Predicting residual distortion of aluminum alloy stiffened sheet after friction stir welding by numerical simulation. *Materials & Design* 2011;32(4):2284–2291. doi:10.1016/j.matdes.2010.11.032.
- [11] Schnubel D, Koçak M, Staron P. Mechanical Tensioning - An innovative method to improve damage tolerance of laser welded aluminium skin-stringer joints in airframes. In: 3rd European Conference on Aero-Space Science EUCASS. Versailles, France; 2009,.
- [12] Zain-ul-Abdein M, Nelias D, Jullien JF, Boitout F, Dischert L, Noe X. Finite element analysis of metallurgical phase transformations in AA 6056-T4 and their effects upon the residual stress and distortion states of a laser welded T-joint. *International Journal of Pressure Vessels and Piping* 2011;88(1):45–56. doi:10.1016/j.ijpvp.2010.10.008.
- [13] Preston RV, Shercliff HR, Withers PJ, Smith SD. Finite element modelling of tungsten inert gas welding of aluminium alloy 2024. *Science and Technology of Welding & Joining* 2003;8:10–18(9). doi:10.1179/136217103225008937.
- [14] Staron P, Koçak M, Williams S. Residual stress distributions in friction stir welded Al sheets determined by neutron strain scanning. In: 6th International Trends in Welding Research Conference Proceedings. Pine Mountain, GA, USA: ASM International; 2003, p. 253–256.
- [15] Staron P, Vaidya WV, Koçak M, Homeyer J, Hackius J. Residual stresses in laser beam welded butt joints of the airframe aluminium alloy AA6056. *Materials Science Forum* 2006;524–525:413–418.
- [16] Machold W, Staron P, Bayraktar F, Riekehr S, Koçak M, Schreyer A. Influence of the welding sequence on residual stresses in laser welded T-joints of an airframe aluminium alloy. *Materials Science Forum* 2008;571–572:375–380.
- [17] Ball D, Lowry D. Experimental investigation on the effects of cold expansion of fastener holes. *Fatigue & Fracture of Engineering Materials & Structures* 1998;21(1):17–34. doi:10.1046/j.1460-2695.1998.00430.x.
- [18] Reid L. Sustaining an aging aircraft fleet with practical life enhancement methods. In: NATO Research and Technology Organisation , editor. RTO-MP-079(II) - Ageing Mechanisms and Control: Specialists' Meeting on Life Management Techniques for Ageing Air Vehicles. 2001,RTO Meeting Proceedings 79(II) / AC/323(AVT-085)TP/50.

- [19] Department of Defense USoA. Joint service specification guide aircraft structures (JSSG-2006). 2006.
- [20] Air Force Research Laboratory / VASM . Handbook for damage tolerant design. URL [www.afgrow.net/applications/DTDDHandbook](http://www.afgrow.net/applications/DTDDHandbook); 2011.
- [21] Gurney T. Influence of residual stresses on fatigue strength of plates with fillet welded attachments. *British Welding Journal* 1960;7:415–431.
- [22] Harrison J. Exploratory fatigue tests on local heating as repair technique. *British Welding Journal* 1965;12:258–260.
- [23] Verma BB, Ray PK. Fatigue crack growth retardation in spot heated mild steel sheet. *Bull Mater Sci* 2002;25:301–307.
- [24] Ray PK, Verma BB, Mohanthy PK. Spot heating induced fatigue crack growth retardation. *International Journal of Pressure Vessels and Piping* 2002;79(5):373–376. doi:10.1016/S0308-0161(02)00019-4.
- [25] Ray PK, Ray PK, Verma BB. A study on spot heating induced fatigue crack growth retardation. *Fatigue & Fracture of Engineering Materials & Structures* 2005;28(7):579–585. doi:10.1111/j.1460-2695.2005.00901.x.
- [26] Tsay LW, Liu YC, Lin DY, Young MC. The use of laser surface-annealed treatment to retard fatigue crack growth of austenitic stainless steel. *Materials Science and Engineering A* 2004;384(1-2):177–183. doi:10.1016/j.msea.2004.06.010.
- [27] Tsay LW, Young MC, Chou FY, Shiue RK. The effect of residual thermal stresses on the fatigue crack growth of laser-annealed 304 stainless steels. *Materials Chemistry and Physics* 2004;88(2-3):348–352. doi:10.1016/j.matchemphys.2004.07.020.
- [28] Shiue RK, Chang CT, Young MC, Tsay LW. The effect of residual thermal stresses on the fatigue crack growth of laser-surface-annealed AISI 304 stainless steel Part I: computer simulation. *Materials Science and Engineering A* 2004;364(1-2):101–108. doi:10.1016/j.msea.2003.07.003.
- [29] Tsay LW, Yang TY, Young MC. Embrittlement of laser surface-annealed 17-4 PH stainless steel. *Materials Science and Engineering A* 2001;311(1-2):64–73. doi:10.1016/S0921-5093(01)00941-8.
- [30] Jang CD, Song HC, Lee CH. Fatigue life extension of a through-thickness crack using local heating. In: *Proceedings of The Twelfth (2002) International Offshore and Polar Engineering Conference*. Kitakyushu, Japan: The International Society of Offshore and Polar Engineers; 2002, p. 224–229.

- [31] Masubuchi K. Analysis of welded structures: Residual stresses, distortion, and their consequences. Pergamon Press; 1980.
- [32] Radaj D. Welding residual stresses and distortion: Calculation and measurement. DVS Verlag; 2003.
- [33] Macherauch E, Kloos K. Bewertung von Eigenspannungen bei quasi-statischer und schwingender Werkstoffbeanspruchung (Teil I - III). *Materialwissenschaft und Werkstofftechnik* 1989;20:1–13, 53–60, 82–91. doi: <http://dx.doi.org/10.1002/mawe.19890200104>.
- [34] ESI – SYSWORLD 2010 Technical Description of Capabilities; 2010.
- [35] Lindgreen L. Modelling for residual stresses and deformations due to welding - Knowing what isn't necessary to know. In: Cerjak H, Bhadeshia H, editors. *Mathematical Modelling of Weld Phenomena*; vol. 6. Institute of Materials, Minerals and Mining; 2001, p. 491–518.
- [36] Dong P. Residual stresses and distortions in welded structures: a perspective for engineering applications. *Science and Technology of Welding and Joining* 2005;10(4):389–397.
- [37] Zain-ul-Abdein M, Nelias D, Jullien JF, Deloison D. Prediction of laser beam welding-induced distortions and residual stresses by numerical simulation for aeronautic application. *Journal of Materials Processing Technology* 2009;209(6):2907–2917. doi:10.1016/j.jmatprotec.2008.06.051.
- [38] Schnubel D, Koçak M, Staron P. Mechanisches Vorspannen - Eine Möglichkeit zur Modifikation schweissinduzierter Verzüge und Eigenspannungen. In: *SYSWELD Forum 2009*. Weimar, Germany; 2009, p. 266–273.
- [39] Zain-ul-Abdein M, Nelias D, Jullien JF, Deloison D. Experimental investigation and finite element simulation of laser beam welding induced residual stresses and distortions in thin sheets of AA 6056-T4. *Materials Science and Engineering A* 2010;527(12):3025–3039. doi:10.1016/j.msea.2010.01.054.
- [40] Zain-ul-Abdein M, Nelias D, Jullien JF, Wagan AI. Thermo-mechanical characterisation of AA 6056-T4 and estimation of its material properties using genetic algorithm. *Materials & Design* 2010;31(9):4302–4311. doi: 10.1016/j.matdes.2010.03.056.
- [41] Preston R, Shercliff H, Withers P, Smith S. Physically-based constitutive modelling of residual stress development in welding of aluminium alloy 2024. *Acta Materialia* 2004;52(17):4973–4983. doi:10.1016/j.actamat.2004.06.048.

- 
- [42] Bower AF. Applied mechanics of solids. URL <http://solidmechanics.org>; 2009.
- [43] ASM International Handbook Committee , editor. ASM Handbook Volume 2, Properties and Selection: Nonferrous Alloys and Special Purpose Materials. ASM International; 1995.
- [44] Grong Ø. Metallurgical Modelling of Welding; vol. 677 of *Materials Modelling Series*. The Institute of Materials; 1997.
- [45] Myhr O, Grong Ø. Process modelling applied to 6082-T6 aluminium weldments - I. Reaction kinetics. *Acta Metallurgica et Materialia* 1991;39(11):2693–2702. doi:10.1016/0956-7151(91)90085-F.
- [46] Myhr O, Grong Ø. Process modelling applied to 6082-T6 aluminium weldments - II. Applications of model. *Acta Metallurgica et Materialia* 1991;39(11):2703–2708. doi:10.1016/0956-7151(91)90086-G.
- [47] Janssen M, Zuidema J, Wanhill R. Fracture Mechanics. Spon Press; 2004.
- [48] Kuna M. Numerische Beanspruchungsanalyse von Rissen. Vieweg+Teubner; 2008. doi:10.1007/978-3-8348-9285-0.
- [49] Servetti G, Zhang X. Predicting fatigue crack growth rate in a welded butt joint: The role of effective R ratio in accounting for residual stress effect. *Engineering Fracture Mechanics* 2009;76(11):1589–1602. doi:10.1016/j.engfracmech.2009.02.015.
- [50] Krueger R. The virtual crack closure technique: History, approach and applications. Tech. Rep. NASA/CR-2002-211628, ICASE Report No. 2002-10; NASA, ICASE; 2002.
- [51] ASTM E647-05 Standard test method for measurement of fatigue crack growth rates. 2005.
- [52] Schwalbe KH. Bruchmechanik metallischer Werkstoffe (Fracture mechanics of metallic materials). Hansa; 1980.
- [53] Walker K. The effect of stress ratio during crack propagation and fatigue for 2024-T3 and 7075-T6. In: Effects of environment and complex load history on fatigue life; vol. STP 462. ASTM; 1970, p. 1 – 14.
- [54] Swift T. Course in damage tolerance technology. 2000.
- [55] Schmidt HJ, Schmidt-Brandecker B. Aerostruc fatigue & damage tolerance course. 2010.

- [56] Pavier MJ, Poussard CGC, Smith DJ. Effect of residual stress around cold worked holes on fracture under superimposed mechanical load. *Engineering Fracture Mechanics* 1999;63(6):751–773. doi:10.1016/S0013-7944(99)00050-8.
- [57] Metal Improvement Company . Shot Peening Applications Guide. 2005.
- [58] Barter S, Molent L, Sharp K, Clark G. Repair and life assessment of critical fatigue damaged aluminium alloy structure using a peening rework method. In: *Proceedings of the USAF ASIP Conference*. 2000, p. 1–19.
- [59] Hatamleh O, Lyons J, Forman R. Laser and shot peening effects on fatigue crack growth in friction stir welded 7075-T7351 aluminum alloy joints. *International Journal of Fatigue* 2007;29(3):421–434. doi:10.1016/j.ijfatigue.2006.05.007.
- [60] Ding K, Ye L. Laser shock peening - Performance and process simulation. Woodhead Publishing Limited; 2006.
- [61] McElhone M, Rugg D. Experimental evaluation of the fatigue performance of aero-engine fan blade dovetails. In: *Presentation for the AeroMat 2005*. 2005, p. 1–19.
- [62] Spanrad S, Tong J. Characterisation of foreign object damage (FOD) and early fatigue crack growth in laser shock peened Ti-6Al-4V aerofoil specimens. *Materials Science and Engineering A* 2011;528(4-5):2128–2136. doi:10.1016/j.msea.2010.11.045.
- [63] Heckenberger U, Hombergsmeier E, v. Bestenbostel W, Holzinger V. LSP to improve the fatigue resistance of highly stressed AA7050 components. In: *Presentation for the 2nd International Conference on Laser Peening*. San Francisco, USA; 2010, p. 1–27.
- [64] Liu Q. An effective life extension technology for 7xxx series aluminium alloys by laser shock peening (final report). Tech. Rep. DSTO-TR-2177, AR-014-283; DSTO; 2008.
- [65] Hatamleh O. A comprehensive investigation on the effects of laser and shot peening on fatigue crack growth in friction stir welded AA 2195 joints. *International Journal of Fatigue* 2009;31(5):974–988. doi:10.1016/j.ijfatigue.2008.03.029.
- [66] Hatamleh O, Mishra RS, Oliveras O. Peening effects on mechanical properties in friction stir welded AA 2195 at elevated and cryogenic temperatures. *Materials and Design* 2009;30(8):3165–3173. doi:10.1016/j.matdes.2008.11.010.

- 
- [67] Rubio-González C, Felix-Martinez C, Gomez-Rosas G, Ocaña J, Morales M, Porro J. Effect of laser shock processing on fatigue crack growth of duplex stainless steel. *Materials Science and Engineering A* 2011;528(3):914–919. doi: 10.1016/j.msea.2010.10.020.
- [68] Lam YC, Griffiths JR. The effect of intermittent heating on fatigue crack growth. *Theoretical and Applied Fracture Mechanics* 1990;14(1):37–41. doi: 10.1016/0167-8442(90)90042-X.
- [69] Cole GK, Lam YC. Fatigue life enhancement of specimens with stress concentrators using a thermo-mechanical technique. *Scripta Metallurgica et Materialia* 1991;25(12):2849–2853. doi:10.1016/0956-716X(91)90168-Z.
- [70] Lam YC, Cole GK. Fatigue life enhancement of butt welds using a thermo-mechanical technique. *Fatigue and Fracture of Engineering Materials and Structures* 1993;16(9):983–994. doi:10.1111/j.1460-2695.1993.tb00133.x.
- [71] Chen BD, Griffiths JR, Lam YC. The effects of simultaneous overload and spot heating on crack growth retardation in fatigue. *Engineering Fracture Mechanics* 1993;44(4):567–572. doi:10.1016/0013-7944(93)90098-D.
- [72] Ibrahim RN, Sayers RSD, Ischenko D. Retardation of crack growth in an aluminium alloy using a thermomechanical conditioning cycle. *Engineering Fracture Mechanics* 1998;59(2):215–224. doi:10.1016/S0013-7944(97)00081-7.
- [73] Raman RKS, Ibrahim RN, Wu F, Rihan R. Thermomechanical manipulation of crack-tip stress field for resistance to stress corrosion crack propagation. *Metallurgical and Materials Transactions A* 2008;39:3217–3223. doi:10.1007/s11661-008-9665-4. 10.1007/s11661-008-9665-4.
- [74] Prasad NE, Gokhale AA, Rao PR. Mechanical behaviour of aluminium-lithium alloys. *Sadhana* 2003;28(1):209–246. doi:10.1007/BF02717134.
- [75] Lavernia EJ, Grant NJ. Aluminium-lithium alloys. *Journal of Materials Science* 1987;22(5):1521–1529. doi:10.1007/BF01132370.
- [76] Knüwer M, Schumacher J, Ribes H, Eberl F, Bes B. 2198 - Advanced Aluminium-Lithium Alloy for A350 Skin Sheet Application. In: Presentation for the 17th AeroMat Conference & Exposition. Seattle, USA; 2006, p. 1–27.
- [77] Lequeu P, Eberl F, Jambu S, Warner T, Danielou A, Bes B. Latest generation of Al-Li alloys developed by Alcan Aerospace. In: Proceedings of the 1st EU-COMAS European Conference on Materials and Structures in Aerospace. VDI Verlag; 2008, p. 1–8.

- [78] Chen J, Madi Y, Morgeneyer TF, Besson J. Plastic flow and ductile rupture of a 2198 Al-Cu-Li aluminum alloy. *Computational Materials Science* 2011;50(4):1365–1371. doi:10.1016/j.commatsci.2010.06.029.
- [79] Lequeu P, Eberl F, Jambu S, Warner T, Danielou A, Bes B. Latest generation of Al-Li alloys developed by Alcan Aerospace. In: Presentation for the 19th AeroMat Conference & Exposition. Austin, Texas USA; 2008, p. 1–24.
- [80] Deutsche Norm DIN 50125: Test pieces for the tensile testing of metallic materials. 1991.
- [81] European Standard EN10002-1:1990 Tensile testing of metallic materials. 1990.
- [82] Richter-Trummer V, Suzano E, ao MB, Roos A, dos Santos J, de Castro P. Influence of the FSW clamping force on the final distortion and residual stress field. *Materials Science and Engineering A* 2012;- (0):- . doi: 10.1016/j.msea.2012.01.016.
- [83] Staron P, Vaidya W, Koçak M. Precipitates in laser beam welded aluminium alloy AA6056 butt joints studied by small-angle neutron scattering. *Materials Science and Engineering A* 2009;525(1–2):192–199. doi: 10.1016/j.msea.2009.06.058.
- [84] Schmidt HJ. Damage tolerance technology for current and future aircraft structures. In: Dalle Donne C, editor. Proceedings of the 23rd ICAF Symposium of the International Committee on Aeronautical Fatigue; vol. 1. 2005, p. 1–41.
- [85] Kocik R, Vugrin T, Seefeld T. Laserstrahlschweissen im Flugzeugbau: Stand und künftige Anwendungen. In: *Strahltechnik*; vol. 28. BIAS; 2006, p. 15–26.
- [86] Parker A. Stress intensity factors, crack profiles and fatigue crack growth rates in residual stress fields. In: Throop JF, Reemsnyder HS, editors. Residual stress effects in fatigue; vol. ASTM STP 776. ASTM; 1982, p. 13–31. doi: 10.1520/STP776-EB.
- [87] Lee YB, Chung CS, Park YK, Kim HK. Effects of redistributing residual stress on the fatigue behavior of SS330 weldment. *International Journal of Fatigue* 1998;20:565–573.
- [88] Mahmoud HN, Dexter RJ. Propagation rate of large cracks in stiffened panels under tension loading. *Marine Structures* 2005;18(3):265–288. doi: 10.1016/j.marstruc.2005.09.001.
- [89] Edwards L. Influence of residual stress redistribution on fatigue crack growth and damage tolerant design. *Materials Science Forum* 2006;524–525:77–82.

- 
- [90] Labeas G, Diamantakos I. Numerical investigation of through crack behaviour under welding residual stresses. *Engineering Fracture Mechanics* 2009;76(11):1691–1702. doi:10.1016/j.engfracmech.2009.03.006.
- [91] Liljedahl C, Brouard J, Zanellato O, Lin J, Tan M, Ganguly S, et al. Weld residual stress effects on fatigue crack growth behaviour of aluminium alloy 2024-T351. *International Journal of Fatigue* 2009;31(6):1081–1088. doi:10.1016/j.ijfatigue.2008.05.008.
- [92] Bao R, Zhang X, Yahaya NA. Evaluating stress intensity factors due to weld residual stresses by the weight function and finite element methods. *Engineering Fracture Mechanics* 2010;77(13):2550–2566. doi:10.1016/j.engfracmech.2010.06.002.
- [93] Beghini M, Bertini L. Fatigue crack propagation through residual stress fields with closure phenomena. *Engineering Fracture Mechanics* 1990;36(3):379–387. doi:10.1016/0013-7944(90)90285-O.
- [94] Beghini M, Bertini L, Vitale E. Fatigue crack growth in residual stress fields: Experimental results and modelling. *Fatigue & Fracture of Engineering Materials & Structures* 1994;17:1433–1444. doi:10.1111/j.1460-2695.1994.tb00786.x.
- [95] Terada H. Stress intensity factor analysis and fatigue behavior of a crack in the residual stress field of welding. *Journal of ASTM International* 2005;2(5):1–11. doi:10.1520/JAI12558.
- [96] Lee CH, Chang KH. Finite element computation of fatigue growth rates for mode I cracks subjected to welding residual stresses. *Engineering Fracture Mechanics* 2011;78(13):2505–2520. doi:10.1016/j.engfracmech.2011.06.006.
- [97] Barsoum Z, Barsoum I. Residual stress effects on fatigue life of welded structures using LEFM. *Engineering Failure Analysis* 2009;16(1):449–467. doi:10.1016/j.engfailanal.2008.06.017.
- [98] Huber N. *Applied Computational Methods in Materials Science*. Lecture notes WS 08/09 TUHH; 2008.
- [99] Zhu XK, Chao YJ. Effects of temperature-dependent material properties on welding simulation. *Computers and Structures* 2002;80:967–976.
- [100] Schnubel D, Möller M, Huber N. Boundary condition identification for structural welding simulation via artificial neural networks. In: *International Workshop on Thermal Forming and Welding Distortion IWOTE'11*. Bremen; 2011, p. 313–326.

- [101] Zäh MF, Lutzmann S, Schober A, Schulz S. Sensitivität des Bauteilverzugs beim Schweißen in Abhängigkeit verschiedener Einspannbedingungen. In: Proceedings of the SYSWELD Forum 2009. Weimar; 2009, p. 274–283.

# List of publications

## Journals

Schnubel D, Huber N. The influence of crack face contact on the prediction of fatigue crack propagation in residual stress fields. *Engineering Fracture Mechanics* 2012, 84(0), 15–24. doi:10.1016/j.engfracmech.2011.12.008.

Schnubel D, Horstmann M, Ventzke V, Riekehr S, Staron P, Fischer T, Huber N. Retardation of fatigue crack growth in aircraft aluminium alloys via laser heating - Experimental proof of concept. *Materials Science and Engineering A* 2012, 546, 8–14. doi:10.1016/j.msea.2012.02.094.

Schnubel D, Huber N. Retardation of fatigue crack growth in aircraft aluminium alloys via laser heating - Numerical prediction of fatigue crack growth. Accepted for publication in *Computational Materials Science* 2012.

Staron P, Fischer T, Lippmann T, Stark A, Daneshpour S, Schnubel D et al. In situ experiments with synchrotron high-energy X-rays and neutrons. *Advanced Engineering Materials* 2011,13(8),658–663. doi:10.1002/adem.201000297.

## Conferences

Schnubel D, Huber N, Horstmann M, Staron P, Fischer T. Laser heating as approach to retard fatigue crack growth in aircraft aluminium structures. *Proceedings of the 1st International Conference of the International Journal of Structural Integrity*. Porto, 2012.

Schnubel D, Horstmann M, Huber N. Prediction of fatigue crack propagation rates in metallic structures containing residual stresses (Poster). *Program and Book of Abstracts of the 26th ICAF Symposium of the International Committee on Aeronautical Fatigue*. Montreal, 2011.

Schnubel D, Möller M, Huber N. Boundary condition identification for structural welding simulation via artificial neural networks. Proceedings of the International Workshop on Thermal Forming and Welding Distortion IWOTE'11. Bremen, 2011.

Schnubel D, Staron P, Koçak M, Huber N. Mechanical tensioning - An approach to control residual stresses and distortions of laser welded aluminium skin-stringer joints (Poster). Proceedings of the European Conference on Materials and Structures in Aerospace EUCOMAS 2010. Berlin, 2010.

Beck W, Schöps S, Schnubel D, Reeder L, Frömming H, Knüwer M, Rendigs K-H, Palm F, Nicolay H-P, Terlinde G, Witulsk T. Titanium - An ideal partner for CFRP. Proceedings CD of the 4th International CFK-Valley Stade Convention. Stade, 2010.

Schnubel D, Koçak M, Staron P. Mechanical tensioning - An innovative method to improve damage tolerance of laser welded aluminium skin-stringer joints in airframes. Proceedings of the 3rd European Conference on Aero-Space Science EUCASS. Versailles, 2009.

Schnubel D, Koçak M, Staron P. Mechanisches Vorspannen - Eine Möglichkeit zur Modifikation schweissinduzierter Verzüge und Eigenspannungen. Proceedings of the SYSWELD Forum 2009. Weimar, 2009.

## Danksagung

Die vorliegende Arbeit ist während meiner Tätigkeit als wissenschaftlicher Mitarbeiter in der Abteilung Fügen und Bewerten der Helmholtz-Zentrum Geesthacht GmbH entstanden.

Herrn Prof. Dr.-Ing. habil. Norbert Huber möchte ich für die hervorragende Betreuung danken. Ich habe ihn als jemanden kennengelernt, der mit großem persönlichem Einsatz wissenschaftliche Zusammenarbeit fördert und zugleich den Freiraum gewährt, der nötig ist um eigene Ideen erfolgreich umzusetzen. Des Weiteren sage ich Herrn Prof. Dr.-Ing. habil. Alexander Düster herzlichen Dank für die Übernahme des Zweitgutachtens dieser Arbeit.

Herrn René Dinse, Herrn Stefan Riekehr, Herrn Manfred Horstmann, Herrn Hamdi Tek, Herrn Volker Ventzke, Herrn Torben Fischer, Herrn Peter Staron, Herrn Jason Dyck, Frau Dr. Fangjaun Qi, Herrn Jakob Hilgert, Frau Petra Fischer und Herrn Peter Haack möchte ich für die aktive Unterstützung bei der Durchführung der experimentellen Versuche für diese Arbeit danken.

Für ihre Unterstützung und die offene, angenehme Arbeitsatmosphäre gilt mein Dank allen Mitarbeitern der Abteilung Fügen und Bewerten sowie der guten Seele des Instituts, Frau Stephanie Koch. Herrn Dr. Nikolai Kashaev, meinem Abteilungsleiter, möchte ich neben der guten Zusammenarbeit insbesondere dafür danken, dass er mir im vergangenen Jahr die Möglichkeit gegeben hat, die vorliegende Arbeit fertig zu stellen.

Herrn Dr. Waman Vaidya, Frau Dr. Xiang Zhang, Herrn Dr. Shahrokh Daneshpour, Herrn Dr. Volkan Uz, Herrn Dr. Ingo Scheider und Herrn Dr. Dirk Steglich danke ich für die anregenden fachlichen Diskussionen bezüglich verschiedener Aspekte der Arbeit.

Für das sorgsame Korrekturlesen der Arbeit bedanke ich mich bei Herrn Daniel Kupka und Frau Anne Groth.

Nicht zuletzt bedanke ich mich bei Frau Julie Altmeyer, Herrn Daniel Kupka und Herrn Dr. Jürgen Markmann für die Organisation der kleinen, spontanen Feier nach der Promotionsprüfung.

Mein besonderer Dank gilt meiner Frau Morelia Vazquez Renteria und meinen Eltern Marianne und Rainer Schnubel für ihre vorbehaltlose Unterstützung in allen Lebenslagen.

Hamburg im Juli 2012

Dirk Schnubel





